

---

# Synthesis and electronic characterization of bottom-up synthesized graphene nanoribbons and porous nanographenes

---

Von der Universität Bayreuth  
zur Erlangung des Grades  
eines Doktors der Naturwissenschaften (Dr. rer. nat.)  
genehmigte Abhandlung

von

Christoph Dobner  
aus Sulzbach-Rosenberg

Erstgutachter: Prof. Dr. Axel Enders  
Zweitgutachter: Prof. Dr. Jürgen Köhler

Tag der Einreichung: 23. August 2022  
Tag des Kolloquiums: 21. Dezember 2022



# Abstract

With digitalization and electromobility on the rise, the demand for semiconductor materials is growing. Besides developing established traditional semiconductor materials even further, the search for alternatives, which show improved physical and electronic properties, is ongoing. Especially the experimental discovery of isolated graphene in 2007 led to a new field of research, focused on graphene based semiconductors. Using different techniques, it is possible to open up a bandgap in the otherwise metallic graphene. The most promising one being lateral confinement of the carbon lattice, creating so-called graphene nanoribbons (GNR).

The electronic properties of these ribbons, like bandstructure and bandgap width, are highly dependent on the exact atomic configuration of the lattice. It is therefore necessary to synthesize such ribbons with atomic precision, which is only possible by using a bottom-up approach. Thereby, the ribbons are built out of individual precursor molecules by on-surface self-assembly, enabling the fabrication of structurally tailored GNRs.

Defined structural modifications can be used to create graphene nanoribbons with different bandgaps, for example by simply varying the width of the ribbon, or to induce topological states in the nanostructures that can be then studied experimentally. Imaging techniques like scanning tunneling microscopy or atomic force microscopy are usually used to verify the exact atomic configuration of the nanostructures.

Most of the approaches to manipulate a GNRs electronic properties are based on the incorporation of heteroatoms in the ribbon or the connection of functional groups to the edges. However, creating other approaches like the use of structural vacancies is mostly unexplored.

In this thesis, novel precursor molecules will be used for the synthesis of GNRs with unique structural modifications. It will be shown that through a variation of the halogenation angle on individual precursor molecules, it is possible to incorporate periodic vacancies, or nanopores, inside the ribbon's backbone. The influence of such pores on the electronic structure of the ribbon will be investigated using scanning tunneling spectroscopy.

Based on these novel GNRs it will be shown that it is possible to create strips of porous nanographene out of individual GNRs. Such nanographenes were previously synthesized via a top-down approach, starting from a larger graphene sheet. However, through this bottom-up method and the incorporation of nanopores inside the structures, a significant bandgap is opened up. Such large, semiconducting porous nanographenes have not been reported before and pose as promising materials for the incorporation in graphene based field effect transistors.

Besides these experimental results, other experimental work like the transfer and setup of a ultra-highvacuum low temperature scanning tunneling microscope and the development of a diffusion based sample preparation technique will also be presented. With this sample preparation technique, it is possible to create graphene nanoribbon heterojunctions of varying precursor composition on a single sample, simplifying their experimental investigation extremely.

The work of this thesis presents a significant step towards the fabrication of graphene based semiconductor devices. With newly developed techniques paving the way for the synthesis of porous nanographenes and GNR heterojunctions.



# Zusammenfassung

Durch die Digitalisierung und Ausweitung der Elektromobilität steigt die Nachfrage nach Halbleiternmaterialien stetig. Neben der Weiterentwicklung von etablierten traditionellen Materialien werden auch Alternativen gesucht, die verbesserte physikalische und elektronische Eigenschaften aufweisen. Vor allem die experimentelle Entdeckung von Graphen im Jahr 2007 eröffnete einen völlig neuen Forschungsbereich, der sich auf Halbleiter auf Graphenbasis konzentriert. Mithilfe verschiedener Techniken ist es möglich, eine Bandlücke in dem ansonsten metallischen Graphen zu öffnen. Die vielversprechendste Technik ist die laterale Begrenzung des Kohlenstoffgitters, wodurch sogenannte Graphen-Nanoribbons (GNR) entstehen.

Die elektronischen Eigenschaften dieser Ribbons, wie deren Bandstruktur und die Größe der Bandlücke, hängen in hohem Maße von der genauen atomaren Konfiguration des GNRs ab. Daher ist es notwendig, diese mit atomarer Präzision zu synthetisieren, was nur mit einem "Bottom-up"-Ansatz möglich ist. Dabei werden die Bänder aus einzelnen Precursormolekülen durch Selbstorganisation auf der Oberfläche zusammengesetzt, was die Herstellung von GNRs mit maßgeschneiderter Struktur ermöglicht.

Durch definierte Veränderungen der Struktur, können Graphen-Nanoribbons mit unterschiedlichen Bandlücken erzeugt werden, indem beispielsweise die Breite des Bandes variiert wird, oder es können gezielt topologische Zustände in den Nanostrukturen induziert und anschließend experimentell untersucht werden. Bildgebende Verfahren wie Rastertunnelmikroskopie oder Rasterkraftmikroskopie werden in der Regel eingesetzt, um die genaue atomare Konfiguration der Nanostrukturen zu überprüfen.

Die meisten Ansätze zur Änderung der elektronischen Eigenschaften von GNRs beruhen auf dem Einbau von Heteroatomen in das Gitter, oder dem Anhängen funktioneller Gruppen an den Ecken des Ribbons. Andere Ansätze, wie der gezielte Einbau von strukturellen Fehlstellen, sind jedoch weitgehend unerforscht.

In dieser Arbeit werden neuartige Precursormoleküle für die Synthese von GNRs, mit einzigartigen strukturellen Modifikationen, verwendet. Es wird gezeigt, dass es durch eine Variation des Halogenierungswinkels der einzelnen Precursormoleküle möglich ist, periodische Fehlstellen, bzw. Nanoporen in das Rückgrat des Ribbons einzubauen. Der Einfluss solcher Poren auf die elektronische Struktur der GNRs wird mit Hilfe der Rastertunnelspektroskopie untersucht.

Auf der Grundlage dieser GNRs wird außerdem gezeigt, dass es möglich ist, aus einzelnen GNRs, Streifen aus porösem Nanographen herzustellen. Solche Nanographene wurden bisher nur durch einen "Top-Down"-Ansatz, basierend auf einer größeren Graphen-Flocke, synthetisiert. Durch die hier verwendete "Bottom-up"-Methode und den Einbau von Nanoporen im Inneren der Strukturen, kann jedoch gezeigt werden, dass eine erhebliche Bandlücke geöffnet wird. Solch große, halbleitende, poröse Nanographene wurden bisher noch nicht experimentell hergestellt und stellen ein vielversprechendes Material für den Einsatz in Graphen-basierten Feldeffekttransistoren dar.

Neben diesen Ergebnissen werden auch andere experimentelle Arbeiten wie der Transfer und Aufbau eines Ultrahochvakuum-Tiefemperatur-Rastertunnelmikroskops und die Entwicklung einer dif-

fusionsbasierten Probenpräparationstechnik vorgestellt. Mit dieser Technik ist es möglich, GNR-Heterostrukturen unterschiedlicher Precursorzusammensetzung auf einer einzigen Probe herzustellen, was deren experimentelle Untersuchung extrem vereinfacht.

Diese Arbeit stellt einen bedeutenden Schritt in Richtung der Herstellung von Halbleiterbauelementen auf der Basis von Graphen dar. Die neu entwickelten Techniken ebnen den Weg für die Synthese von porösen Nanographenen und der simplen Herstellung von GNR-Heterostrukturen.

# Contents

<b>1</b>	<b>Introduction</b>	<b>1</b>
<b>2</b>	<b>Theoretical basics</b>	<b>3</b>
2.1	Scanning tunneling microscopy . . . . .	3
2.2	Scanning tunneling spectroscopy . . . . .	5
2.3	Self-assembly on surfaces . . . . .	9
2.3.1	Molecule-Surface interactions . . . . .	9
2.3.2	Intermolecular interactions . . . . .	10
<b>3</b>	<b>Graphene nanoribbons (GNR)</b>	<b>13</b>
3.1	Graphene . . . . .	13
3.2	GNR synthesis . . . . .	14
3.3	State of the art on-surface GNR reserach . . . . .	18
3.3.1	Substrates . . . . .	18
3.3.2	Bandgap engineering . . . . .	19
3.3.3	GNR heterojunctions and topological states . . . . .	19
3.3.4	Device fabrication . . . . .	19
3.3.5	Porous GNRs . . . . .	20
<b>4</b>	<b>Experimental details</b>	<b>21</b>
4.1	Ultrahigh vacuum . . . . .	21
4.2	Low temperature scanning tunneling microscope (LT-STM) . . . . .	23
4.3	Scanning tunneling spectroscopy setup . . . . .	28
4.4	Sample preparation . . . . .	30
4.4.1	Substrate cleaning . . . . .	30
4.4.2	The Au(111) surface . . . . .	31
4.4.3	Molecular deposition . . . . .	33
4.5	Organic evaporator . . . . .	35
4.6	Tip preparation . . . . .	36

4.7	Surface diffusion and self-assembly . . . . .	40
4.7.1	Diffusion processes on metal surfaces . . . . .	40
4.7.2	Diffusion based sample preparation . . . . .	43
<b>5</b>	<b>Experimental results</b>	<b>46</b>
5.1	Graphene nanoribbons . . . . .	47
5.1.1	C90-GNRs . . . . .	49
5.1.2	9-AGNRs . . . . .	54
5.1.3	T90-GNRs . . . . .	57
5.1.4	T30-GNRs . . . . .	63
5.1.5	C30-GNRs . . . . .	69
5.1.6	Conclusion and outlook . . . . .	74
5.2	Triangle molecules . . . . .	76
5.2.1	C30-triangle . . . . .	76
5.2.2	T30-triangle . . . . .	81
5.2.3	Conclusion and outlook . . . . .	83
5.3	GNR Heterojunctions . . . . .	84
5.3.1	C90-GNR/9-AGNR Heterojunctions . . . . .	85
5.3.2	C90-/T90-GNR Heterojunctions . . . . .	89
5.3.3	Conclusion and outlook . . . . .	94
5.4	Porous nanographenes (PNG) . . . . .	95
5.4.1	C30-PNGs . . . . .	96
5.4.2	T30-PNGs . . . . .	100
5.4.3	T90-PNGs . . . . .	107
5.4.4	Conclusion and outlook . . . . .	112
<b>6</b>	<b>Summary</b>	<b>113</b>
<b>7</b>	<b>Appendix</b>	<b>115</b>
7.1	STS parameters . . . . .	115
7.2	IUPAC names of precursor molecules . . . . .	116
7.3	C90-/T90-GNR Heterojunctions . . . . .	117
	<b>References</b>	<b>132</b>

# List of Figures

2.1	Principles of STM . . . . .	4
2.2	Theoretical STS spectra of different materials . . . . .	7
2.3	Schematic STS setup . . . . .	8
3.1	2D Brillouin zone of graphene and bandstructure of GNRs . . . . .	15
3.2	On-surface synthesis route for GNRs . . . . .	17
4.1	Photograph of the LT-STM system . . . . .	24
4.2	Schematic UHV system layout . . . . .	25
4.3	Schematic drawing of the LT-STM . . . . .	27
4.4	STM images of clean Au(111) . . . . .	32
4.5	Representation of the postannealing process after DCT of molecular powder . . . . .	34
4.6	CAD model of the molecular evaporator . . . . .	35
4.7	SEM image of a etched tungsten tip . . . . .	38
4.8	Exemplary STM images of samples after STM tip preparation . . . . .	39
4.9	Schematic process of surface diffusion . . . . .	40
4.10	Errorfunction plotted for different times $t$ . . . . .	42
4.11	Distance dependent surface coverage . . . . .	43
4.12	Modelled coverage-distance dependence . . . . .	44
5.1	Different precursor structures . . . . .	47
5.2	Synthesis of C90-GNRs and STM images of resulting structures . . . . .	50
5.3	$dI/dV$ point spectra of C90-GNRs . . . . .	52
5.4	Synthesis of 9-AGNRs and STM images of resulting structures . . . . .	54
5.5	$dI/dV$ point spectra of 9-AGNRs . . . . .	56
5.6	Synthesis of T90-GNRs and STM images of resulting structures . . . . .	57
5.7	3D modeled parallel alignment of T90-polymers . . . . .	59
5.8	$dI/dV$ point spectra of T90-GNRs . . . . .	60
5.9	$dI/dV$ maps of T90-GNRs . . . . .	61
5.10	Synthesis of T30-GNRs and STM images of resulting structures . . . . .	63

5.11	3D modeled parallel alignment of T30-polymers . . . . .	65
5.12	<i>dI/dV</i> point spectra of T30-GNRs . . . . .	66
5.13	<i>dI/dV</i> maps of T30-GNRs . . . . .	67
5.14	Synthesis of C30-GNRs and STM images of resulting structures . . . . .	69
5.15	<i>dI/dV</i> point spectra of C30-GNRs . . . . .	71
5.16	<i>dI/dV</i> maps of C30-GNRs . . . . .	72
5.17	Synthesis of C30-triangles and STM images of resulting structures . . . . .	77
5.18	Analyzed intermolecular distances of C30-triangles . . . . .	78
5.19	STM images of covalently bound C30-triangles . . . . .	79
5.20	STM images of T30-triangle based structures . . . . .	81
5.21	STM images of C90-GNR/9-AGNR heterojunctions . . . . .	86
5.22	<i>dI/dV</i> maps of C90-GNR/9-AGNR heterojunctions . . . . .	87
5.23	Synthesis of C90-/T90-GNR heterojunctions and STM images of resulting structures	89
5.24	<i>dI/dV</i> point spectra of a C90-/T90-GNR heterojunction . . . . .	91
5.25	<i>dI/dV</i> maps of C90-/T90-GNR heterojunctions . . . . .	93
5.26	STM images of C30-PNG structures . . . . .	96
5.27	<i>dI/dV</i> point spectra of C30-PNGs . . . . .	98
5.28	Type I and Type II alignment of T30-GNRs . . . . .	100
5.29	STM images of T30-PNG structures . . . . .	102
5.30	<i>dI/dV</i> spectra of T30-PNGs . . . . .	103
5.31	<i>dI/dV</i> maps of T30-PNGs . . . . .	105
5.32	STM images of T90-PNGs . . . . .	107
5.33	Type I and Type II alignment of T90-GNRs . . . . .	109
5.34	Detailed STM image of a T90-PNG . . . . .	110
5.35	<i>dI/dV</i> point spectrum of a T90-PNG . . . . .	111
7.1	<i>dI/dV</i> maps of C90-/T90-GNR heterjunctons . . . . .	117

# 1 Introduction

As digitalization advances we integrate more and more electronics into our daily lives. This development leads to a constantly high demand for semiconductor materials, which is growing at a fast rate. A predicted annual market growth of 6% until 2030 leaves no doubt that this development is going to continue for the next couple of years.<sup>[1]</sup> While most of the technology is still based on traditional inorganic semiconductor materials like silicon, gallium arsenide and germanium,<sup>[2]</sup> the search for new materials with advanced properties is ongoing.<sup>[3-5]</sup>

Especially the discovery of graphene in 2004 led to a new field of research of 2D materials. Graphenes remarkable structural and electronic properties promised huge advantages for future applications in electronic devices.<sup>[6-11]</sup> On the basis of more than 15 years of continuous research, it is now possible to induce semiconducting properties into the otherwise metallic two dimensional graphene. This can be achieved by using different approaches like doping the graphenic lattice with heteroatoms,<sup>[12,13]</sup> inducing a bandgap through substrate interactions<sup>[14-16]</sup> or through the use of bilayer graphene.<sup>[17,18]</sup> However, the most promising technique is the structural confinement of the graphene lattice. This has already been predicted to open up a bandgap long before the first graphene sheet had even been experimentally isolated.<sup>[19-21]</sup>

By creating a quasi one-dimensional strip of graphene, a so called graphene nanoribbon (GNR), the charge carriers in the lattice are laterally confined. This quantum confinement leads to a quantization of electronic states and thereby to the opening of a bandgap. The width of the bandgap of these GNRs is thereby strongly dependant on the exact atomic edge configuration of the ribbon and inversely proportional to the width of the structure.<sup>[22-25]</sup>

In order to synthesize such nanostructures, it is not suitable to use traditional top-down approaches, since the apparent lack of atomic precision. Instead, a bottom-up strategy is employed, where the GNRs are built out of tailor made precursor molecules in a controlled, step-wise process.<sup>[26]</sup> It is thereby possible to create GNRs of different width, structure and chemical composition by simply changing the design of the precursor. By producing a variety of GNRs, it is now known how different modifications affect their electronic properties, paving the way towards bandgap engineering of GNRs.

The goal of this thesis is to increase the knowledge about how different structural modifications influence the bandgap of GNRs. Until now, most of the existing research works focus on the

---

modifications of the edges of the ribbon. Here, a different approach will be presented, that involves the incorporation of structural vacancies in the GNRs backbone. Little is known about how such periodic defects will affect the electronic structure of GNRs. In an additional step, it will also be investigated how it is possible to create larger porous nanographene (PNG) strips out of individual porous and non-porous GNRs.

In this work, three novel precursor molecules were used to synthesize GNRs on a Au(111) surface. Based on these GNRs, strategies will be presented for the synthesis of heterostructures and nanographenes. All of these nanostructures will be characterized by the use of scanning tunneling microscopy (STM) and scanning tunneling spectroscopy (STS).

As an introduction, the theoretical basics of STM and STS will be described in chapter 2 together with a short explanation of different molecular self-assembly mechanisms on surfaces. Chapter 3 will then continue to provide a detailed description of the structure and electronics of two dimensional graphene layers and GNRs. Reviewing structural differences, electronic properties and synthesis strategies will help to give an idea how the results of this thesis fit into the current state of the art research.

In chapter 4 the focus will be on the experimental aspects of the measurements and sample preparation. Since a large part of the experimental work went into the transfer and setup of an ultrahighvacuum low-temperature scanning tunneling microscope (UHV LT-STM), a in-depth discussion of UHV environments, the UHV system and the LT-STM will be given. Also, a newly developed method for sample preparations will be introduced.

The experimental results of the on-surface bottom-up synthesis of GNRs will be shown in section 5.1. The structurally different precursor molecules result in different types of GNRs. By extensively studying their electronic properties it will be shown how nanopores and edge modifications influence the bandgap width of the ribbons.

Section 5.2, will reveal how different reaction paths of precursor molecules in solution and on metal surfaces result in structurally different reaction products.

Two examples for GNR heterjunctions will be presented in section 5.3. Based on the developed diffusion based sample preparation technique, it will be shown how this approach facilitates the synthesis of such structures.

Finally, in section 5.4, the results of the synthesis of porous nanographenes out of individual GNRs will be discussed. The spectroscopic characterization revealed a surprising behaviour of the bandgap which strengthens the hypothesis about the influence of porosity on the electronic structure of GNRs and porous nanographenes.

A summary of all the relevant results will be given in chapter 6.

## 2 Theoretical basics

In this first part of the thesis a short introduction of the methods of measurements, namely scanning tunneling microscopy and -spectroscopy, will be given. The theoretical derivation of the equations given in this chapter have been elaborated in multiple sources. Because of this, only an abbreviated version will be given here. The reader is kindly referred to the Refs. [27,28] for further reading. This chapter also includes further information about the surface structure of the used Au(111)-substrate and the basics of molecular interactions on surfaces.

### 2.1 Scanning tunneling microscopy

While optical imaging microscopy techniques reach their limit at resolutions in the sub nm-range, scanning probe methods allow for direct real space imaging in the sub pm-regime. First developed in 1981 by Binnig and Rohrer at IBM,<sup>[29,30]</sup> the STM soon became one of the most important tools in surface science. Using a sharp metal tip and placing it just a few hundred pm over a metallic substrate, they were able to measure electrons tunneling from the tip to the surface as a tunneling current  $I_T$ . Since this groundbreaking development, more specialized scanning probe measurement techniques have been developed, but the fundamental working principle remains the same. A probe of some kind is placed in close proximity, or even in direct contact, to the sample surface and then moved in a raster by piezoelectric elements. The probe surface interaction, which can be any kind of physical interaction, is measured during this process and the data represents a lateral distribution of the respective quantity.

Figure 2.1 **a** shows a schematic setup of a STM measurement. The tip is mounted on a piezoceramic scanner tube and is placed in close proximity over the surface, which is here represented by yellow spheres. If one assumes the experiment to be placed inside a vacuum chamber and that tip and sample material is conducting, one can model the setup as a simple metal-vacuum-metal junction as shown in **b**.

If the tip-sample distance  $s$  is large, the quantum mechanical wave functions of tip electrons  $\psi_{\text{Tip}}$  outside of the solid simply decays exponentially into the vacuum. However, if  $s$  is reduced to a few nm, wave functions to tip- and sample-electrons  $\psi_{\text{sample}}$  overlap, resulting in a nonzero probability for a tip electron to tunnel into the sample. This finite tunneling conductance however

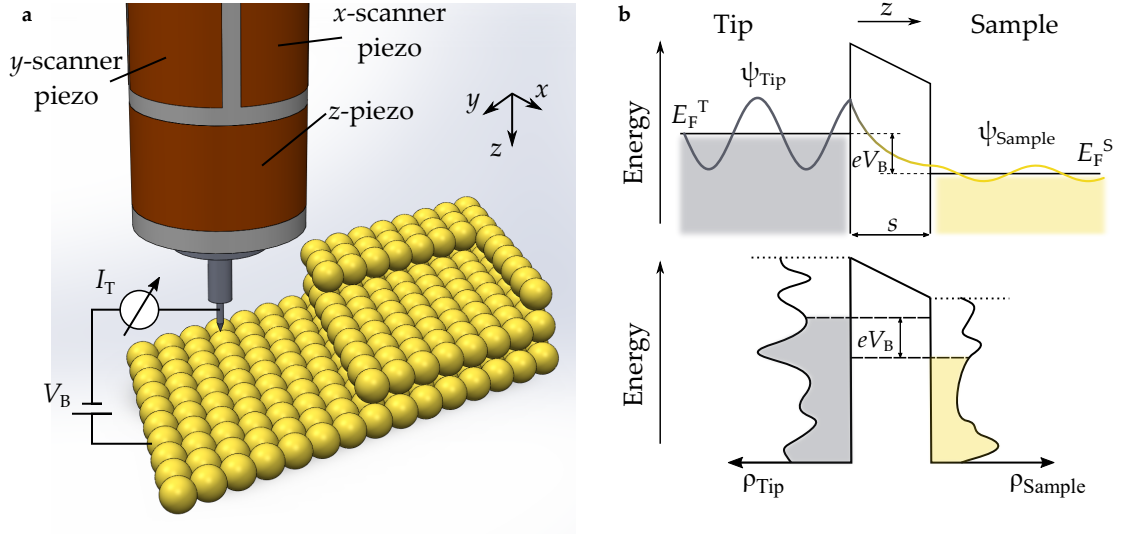


Figure 2.1: **a)** Schematics representation of the STM setup. **b)** Principle of the tunneling process between the tip and the sample.

is not enough to observe a net tunneling current  $I_T$ , as electrons would just flow from the tip into the sample until the Fermi energies  $E_F$  of both materials are equalized. If a bias voltage  $V_B$  is applied however, a net tunneling current can be observed, since the Fermi energies of tip and sample are shifted by  $\frac{1}{2}eV_B$  respectively. This process is shown in figure 2.1 **b**, where in the upper image, the tunneling junction is shown spatially, with the density of states (DOS) of the tip  $\rho_{\text{Tip}}$  and sample  $\rho_{\text{Sample}}$  assumed to be constant. The lower graphic draws a more realistic case, where one can see that these densities of states are not at all constant but depend strongly on the energy, which means that the measured tunneling current  $I_T$  has a nontrivial dependency on  $V_B$  and contains information about the density of states in both the tip and the sample.

As mentioned before, the complete derivation of the equation for the tunneling current will be skipped here. Following Bardeen's theory of tunneling, which is extensively described in Ref. [27], the tunneling current takes the form

$$I_T = \frac{8\pi^2 e}{h} \int_0^{eV} \rho_{\text{Tip}}(E_F^T - eV + \epsilon) \rho_{\text{Sample}}(E_F^S + \epsilon) |M|^2 d\epsilon, \quad (2.1)$$

with  $\rho_{\text{Tip}}$  and  $\rho_{\text{Sample}}$  being the density of states of the tip and sample respectively and  $M$  describing the tunneling matrix element. For simplicity,  $|M|$  and  $\rho_{\text{Tip}}$  are often assumed to be independent of the energy  $\epsilon$  in the range of the bias voltage  $eV_B$ . The expression equation (2.1) thus becomes

$$I_T \approx \frac{8\pi^2 e}{h} \rho_{\text{Tip}} |M|^2 \int_0^{eV_B} \rho_{\text{Sample}}(E_F^S + \epsilon) d\epsilon. \quad (2.2)$$

In this case, the tunneling current  $I_T$  is a convolution of the tip and sample density of states. To further simplify this expression and to provide theoretical predictions for STM imaging, Tersoff and Hamann suggested to use a simple model for the tip wave function. They assumed that the outermost tip atom mainly defines the tunneling process and that the wave function can be modelled as a spherical s-orbital wave function centered at  $r_0$ . This means that the tunneling matrix element can be approximated as

$$M \propto \psi_{\text{Sample}}(\vec{r}_0). \quad (2.3)$$

With this model and the assumption that the tip DOS is constant in the energy range of interest, one can further simplify equation (2.2) to

$$I_T \propto \int_0^{eV_B} \rho_{\text{Sample}}(E_F^S + \epsilon, \vec{r}_0) d\epsilon. \quad (2.4)$$

Under these idealized assumptions, the tunneling current is directly proportional to the local surface density of states of the sample  $\rho^{\text{sample}}$ .

Even though this model is simple, it appears to describe experimental STM data well. Since the tunneling current is directly proportional to the local DOS of the sample, it can be used for imaging and for measurements of the local electronic properties of the sample alike. For imaging, the STM is often used in constant current mode, meaning that the tunneling current is kept constant by a feedback loop. The z-position of the tip is therefore regulated by a piezo actuator and can be recorded while moving over the surface. Assuming the DOS of the sample is constant all over the scan area, this can then be interpreted as a topographic image of the sample surface. For clean metal substrates this assumption might be mostly true, however if there are adsorbed atoms or molecules present on top of the surface, the interpretation of the STM image becomes more complicated. One should always keep in mind that STM images do not generally represent topographic information about the sample.

## 2.2 Scanning tunneling spectroscopy

Even though imaging single molecules and atoms on surfaces might be the predominant use of the STM, it is far more than just an imaging method. Since the tunneling current provides

direct information about the local DOS of the sample at the respective bias voltage, as shown in equation (2.4), it is possible to use it to spectroscopically investigate the sample. Using scanning tunneling spectroscopy allows to probe the energy dependent local DOS of the sample through different techniques.

Looking at equation (2.1) one sees that for a given energy  $\epsilon$ ,  $I_T$ ,  $V_B$  and the tip-sample distance  $s$  are directly interconnected. This allows for three different modes of operation, which establishes the relation between these parameters by always keeping one of them fixed.  $I(z)$  and  $V(z)$  spectroscopy both rely on a change in the tip position. During a  $I(z)$  measurement the tunneling current is measured as a function of  $z$ , from which the local work function of the sample can be extracted by using the exponential dependence between  $I$  and  $z$ , given in equation (2.8). For  $V(z)$  spectroscopy, the measurement is similar, only now the voltage is measured, allowing to gain information about electronic states in the field emission regime.

The third spectroscopy mode, which was also used to characterize the nanostructures presented in this work, is  $I(V)$  spectroscopy. Here, the tip sample distance  $s$  is kept constant by opening the feedback loop, and the bias voltage is varied. The  $I-V$  curve gives information about whether the sample has metallic, semiconducting or insulating properties. Characteristic  $I-V$  measurements for each case are summarized in figure 2.2. The conductance electrons in metallic substrates for example result in a nearly constant density of states and therefore in a  $I-V$  curve with a constant slope. For semiconductors and insulators, this is different. The electronic bandgap in both material classes means that no electronic states exist near the Fermi energy. The density of states of the sample is therefore zero in this energy interval, meaning that the tunneling current amplitude does not depend on  $V$ . As can be seen in the two  $I-V$  curves, the slope near the Fermi energy is zero and, when looking at the  $dI/dV-V$  curves, the bandgap is directly visible. The  $dI/dV$  signal directly reflects the conductance variations of the sample, which is the reason why in most experiments this value is measured directly with the use of a Lock-In amplifier. In principle, it is also possible to calculate the numerical derivative of the  $I-V$  curve, however the direct approach is much more sensitive and allows for dynamic adjustment of parameters during the measurement.

Using a Lock-In amplifier to measure the  $dI/dV$  signal directly involves an additional modulation of the bias voltage. The bias voltage has to be modulated using an AC voltage with an amplitude much smaller than  $V_B$  and a frequency greater than the cutoff frequency of the low-pass feedback loop. The measured tunneling current will then also show a modulation with the same frequency. Feeding the  $I_T$ -signal back into the Lock-In amplifier gives a demodulated DC signal which is directly proportional to  $dI/dV$ . With all the assumptions previously made, it therefore represents the local conductivity of the sample.

A derivation of equation (2.4) gives

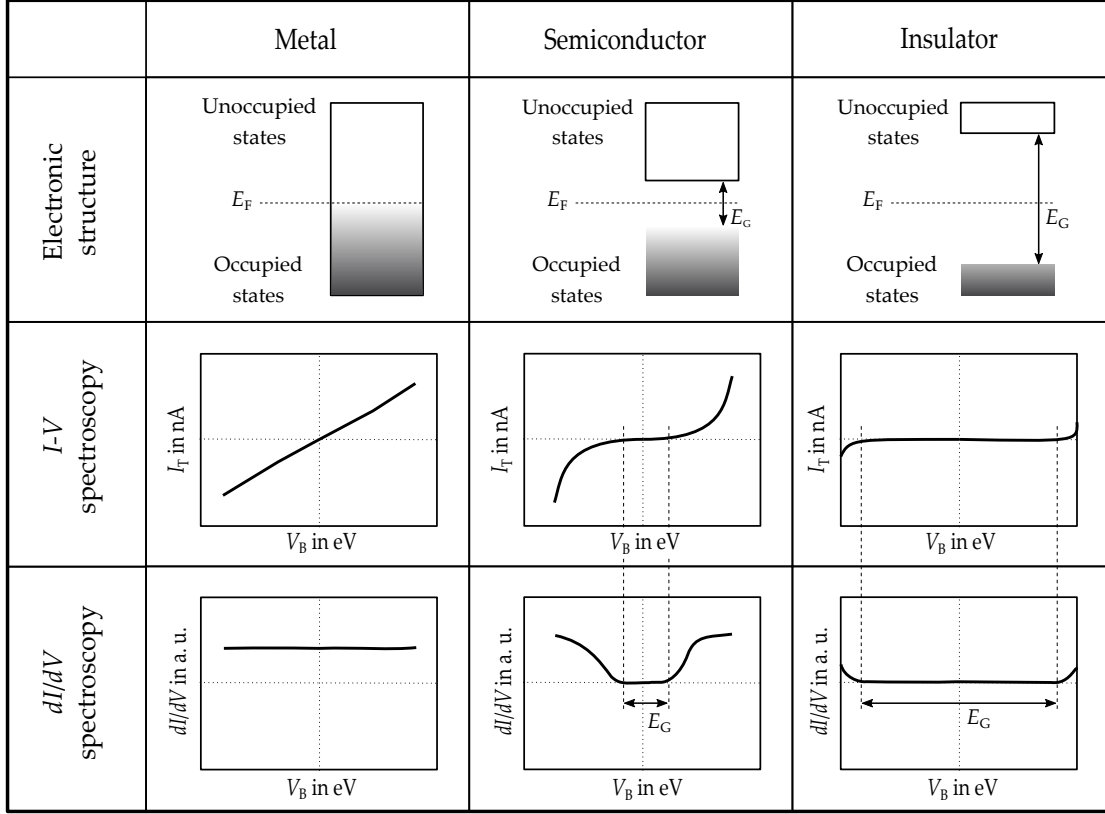


Figure 2.2: Overview of theoretical STS spectra for different materials.

$$dI/dV \propto \rho_{\text{Sample}}(E_F^S + eV_B, \vec{r}_0), \quad (2.5)$$

which shows that, in the boundaries of the Tersoff-Hamann-model, the differential conductance  $dI/dV$  is directly proportional to the local DOS of the sample  $\rho_{\text{Sample}}$  at the energy  $E_F^S + eV_B$  at the tip location  $\vec{r}_0$ .

Figure 2.3 **a** schematically shows the experimental setup used for direct  $dI/dV$ - $V$  measurements with all components. During data acquisition, the tip is held stationary over the sample and the feedback loop is turned off to prevent changes of the tip-sample-distance during the measurement. The AC signal produced by the signal generator is fed into the  $V_{ext}$ -input of the STM control, where it is added to  $V_B$  and the sum is applied to the sample. Simultaneously, it is used as an external reference signal on the lock-in amplifier to provide a reference for demodulation. The tunneling current measured across the junction is first processed in a preamplifier, where current in the range of pA is converted into a proportional voltage signal and amplified. The signal is then processed as usual by the control unit for visualization of the I-V-curve and simultaneously used as

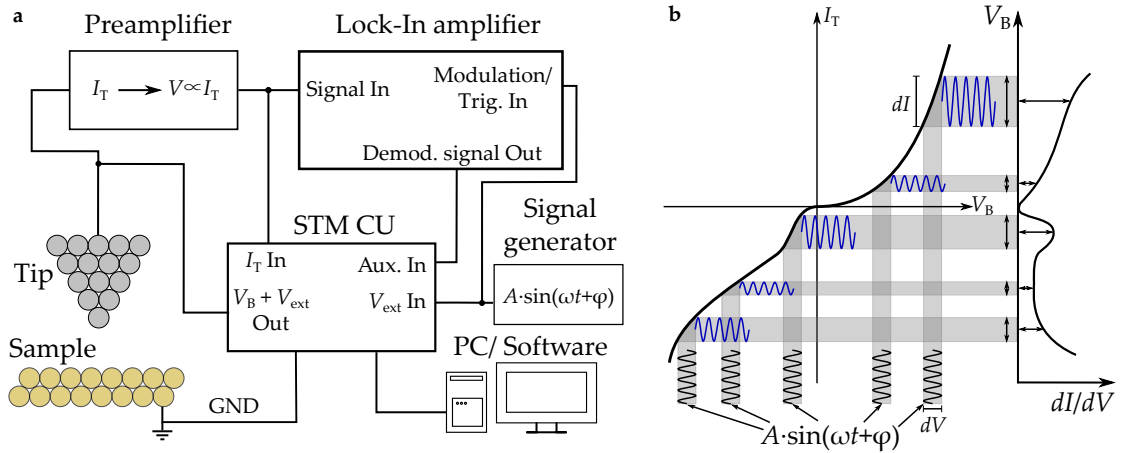


Figure 2.3: **a)** Schematic experimental setup for the direct measurement of the  $dI/dV$  signal using a Lock-In amplifier. **b)** Visualization of the modulation and demodulation while measuring a  $dI/dV$  point spectrum directly.

a signal input for the Lock-In amplifier. The Lock-In amplifier, being supplied with the reference signal and the periodically modulated response in the tunneling current then demodulates the signal component with a constant phase relative to the modulation. This resulting DC signal is proportional to the differential conductance of the sample. Plotting the differential conductance against the bias voltage then gives the desired  $dI/dV$ - $V$  curve in real time as the  $I$ - $V$  curve is measured simultaneously.

Figure 2.3 **b)** visualizes the correspondance between  $I$ - $V$ - and  $dI/dV$ - $V$ -curves again. An exemplary  $I$ - $V$  curve is shown, which presents a complex relation between  $I_T$  and  $V_B$ . The modulation voltage, shown in black, allows to probe the slope of the  $I$ - $V$  curve in small energy intervals. The size of these intervals is given by the amplitude of the modulation, which is usually in the range of 10-50 mV. A higher amplitude increases the signal-to-noise ratio, but also lowers the energetic resolution. To measure an  $I$ - $V$  curve, the bias voltage is increased in small steps, within which the bias voltage is kept constant for a certain amount of time, the so-called raster time  $T_{\text{Raster}}$ , over which the signal is averaged. The modulation frequency should be chosen so that it is possible to average over at least 10 periods of the signal at each raster point, meaning that the relation

$$T_{\text{Raster}} \geq \frac{10}{f_{\text{mod}}} \quad (2.6)$$

is fulfilled. In the case of  $dI/dV$  spectroscopy, where the raster times are usually around 15 ms, it is usually in the range of 1 kHz. The modulated tunneling current, whose AC part is shown in blue here, is fed into the Lock-In amplifier, where parts of the signal with the same frequency as

the modulation are demodulated, resulting in a DC signal proportional to  $dI/dV$ .

Another point which has to be mentioned here is that, although having a theoretically constant density of states, the  $dI/dV$  spectra of clean metal surfaces are far from constant. Even though the tunneling junction proposes a symmetric problem, the quantum mechanical calculations show that tunneling from the tip into the sample ( $V_B < 0$ ) has a higher tunneling probability and therefore results in a larger tunneling current than for positive bias. To prove this, has to go back to equation (2.1) and bring it into a symmetric form with respect to the bias voltage interval  $eV_B$ .

$$I_T = \frac{8\pi^2 e}{h} \int_{-\frac{1}{2}eV_B}^{+\frac{1}{2}eV_B} \rho_{\text{Tip}}(E_F^T - \frac{1}{2}eV_B + \epsilon) \rho_{\text{Sample}}(E_F^S + \frac{1}{2}eV_B + \epsilon) |M|^2 d\epsilon \quad (2.7)$$

A closer look at the tunneling matrix element  $M$  shows that it can be split up into an energy independent part  $M(0)$  and an exponential dependency on the energy  $\epsilon$  and the tip sample distance  $s$ .

$$M(\epsilon) = M(0) \exp\left(\frac{\kappa_0 \epsilon s}{2\bar{\Phi}}\right) \quad (2.8)$$

Here  $\kappa_0$  is the exponential decay constant and  $\bar{\Phi}$  describes an average work function of both materials. Integrating over the exponential part of the  $M(\epsilon)$  shows that the exponential dependency on the energy results in a asymmetry in  $I$ - $V$  curves, which is directly visible when looking at the presented spectra in chapter 5.

## 2.3 Self-assembly on surfaces

In this section, a brief overview of different interactions leading to the self-assembly of organic molecules on metal surfaces will be given. Different adsorption mechanisms as well as intermolecular interactions will be discussed. If interested, the reader is referred to Refs. [31] and [32] for further reading.

### 2.3.1 Molecule-Surface interactions

Adsorption describes the phenomenon of single atoms or molecules to adhere to a surface through molecular interactions. They thereby leave their initial state in the gaseous or liquid phase and become immobilized at an interphase,<sup>[33]</sup> in the case of this work, the solid state of the metal single crystal. Adsorption is usually an exothermic process, meaning that the adsorbed state of molecules or atoms is energetically preferred.

Depending on the strength of the interaction, two main types of adsorption are distinguished. Physisorption, where the molecules are bound to the surface due to van der Waals or dipole-dipole interactions and chemisorption, described by the formation of a chemical bond between the molecule and the surface.

In physisorbed systems the enthalpy of the bond is typically less than 0.2 eV,<sup>[32]</sup> and even though the molecules are bound to the interphase, diffusive motion is still possible on the surface. Because the interaction is weak, the surface and molecules remain structurally unharmed although the electronic interactions are not negligible. The electronic states of an adsorbed molecule can however be modified by substrate interactions in some cases, which one should always keep in mind when measuring electronic structures of molecules on surfaces.<sup>[34]</sup> When dealing with purely organic molecular precursors, the molecules are usually physisorbed on the metal surface and self-assembly is achieved through intermolecular interactions rather than surface epitaxy.

As already mentioned, chemisorption is accompanied by the formation of covalent bonds between the adsorbed molecule and surface atoms which leads to enthalpies being in the range of 2.0 eV.<sup>[32]</sup> Due to the formation of such bonds, the structural integrity of the adsorbed molecule is often threatened, since fragmentation might occur. Hybridization of radical molecules with metal atoms of the surface then leads to a complete immobilization until the molecule-metal bond is broken again, for example by a thermal annealing process. Such hybridized precursor-metal structures were also reported to occur on some occasions on GNR on-surface synthesis routes. It was found that strong precursor-metal interaction led to the formation of chiral GNRs instead of pristine armchair GNRs depending on the substrate used.<sup>[35]</sup> Also that the formation of organometallic hybrid structures can promote GNR synthesis.<sup>[36]</sup>

### 2.3.2 Intermolecular interactions

The interaction between two adsorbed atoms or molecules on the surface may be repulsive or attractive, depending on forces acting between them.<sup>[32]</sup> While attractive forces promote the formation of one- or two-dimensional aggregates, repulsive interactions might show a different outcome. Depending on the strength and orientation of the repulsive forces, the molecules might be ordered or disordered, however the intermolecular distances are generally larger, resulting in a lower packing density. However, for both mechanisms the free energy of the combined system is minimized in the final configuration.

By far the strongest intermolecular interaction ( $E_B > 1.5$  eV) possible is the formation of covalent bonds between neighboring molecules. To form such bonds, it is usually necessary to separate functional groups or to break single covalent bonds of the molecule. This can either be achieved by activation of functional groups through a thermal annealing process, or by lowering specific binding energies of the molecular structure. As mentioned in section 4.4.2, the Au(111)

substrate provides such a strong catalytic effect together with other metal single crystal surfaces. On Cu(111) for example, it is even possible, that molecular precursors fragment upon adsorption on the surface at room temperature. Of course, a change of the initial molecular structure can also be unwanted, but for the case of covalently bound nanostructures it opens new ways for synthesis routes. For the on-surface synthesis of graphene nanoribbons for example, the individual reaction steps are based on the step wise breaking of different molecular bonds by thermal annealing steps, which provides full control over the reaction process.

Other attractive coupling mechanisms like dipole-dipole interactions, including hydrogen bonds, and van der Waals interactions, are based on electrostatic forces and therefore short ranged and weaker than covalent bonds. With binding energies  $E_B$  being in the range of 0.005 meV to 0.4 eV, they are mostly weak and easy to overcome. Diffusive motion at slightly elevated temperatures is often enough to rearrange such weakly bound molecules and have them form new structures.

In the special case of organic molecules consisting mostly of  $sp^2$  hybridized carbon atoms, the large  $\pi$  systems present provide another possibility of intermolecular coupling. So called  $\pi$ - $\pi$  interactions, originating from effective quadrupole moments of organic compounds, lead to a parallel or T-shaped alignment of  $\pi$  systems.<sup>[37]</sup> The binding energies depend strongly on the exact size and shape of the  $\pi$ -system and are therefore not numerically specified here. Crystals of solution synthesized GNRs usually appear hardly soluble due to the strong  $\pi$ - $\pi$  stacking between ribbons,<sup>[38]</sup> which also results in them forming upright standing,  $\pi$ - $\pi$  stacked islands when deposited on a flat nonmetallic substrate.<sup>[39]</sup> This form of  $\pi$ - $\pi$  stacking can also lead to a parallel arrangement of individual GNR polymers. Non-planarized phenyl rings on the edges of polymer chains often interact with each other, which results in attractive forces between neighboring chains. This interaction mechanism will play a key role in the synthesis of nanographenic structures, presented in section 5.4.

All the above-mentioned attractive interactions can lead to the formation of one- or two-dimensional aggregates on surfaces, however there are also forces that prohibit adsorbed molecules from coming closer together. One way to think of such repulsive forces is through electrostatic interaction, meaning that there have to be nonzero net charges in each molecule. However, besides for initially dipolar molecules, such forces can also occur between non-polar molecules. The first possibility would be, if a charge transfer occurs between the adsorbed molecule and the surface, meaning that the molecule acts as a donor or acceptor and thereby interchanges an electron with the metal surface.<sup>[40]</sup> The molecule then appears charged, repelling neighboring, evenly charged adsorbates. The other mechanism is the so called pillow effect, where Pauli repulsion between the adsorbate and the surface electronic configurations leads to a surface charge displacement in the substrate. This results in a charge 'pillow' forming around the contour of the adsorbate, without any charges being transferred.<sup>[41,42]</sup> These induced charge clouds then repel each other, leading

to an equidistant spacing of molecules on the surface.<sup>[43]</sup> Although being a substrate mediated effect, this can be viewed as an intermolecular interaction, since the resulting forces are a result of the molecule-surface system.

## 3 Graphene nanoribbons (GNR)

In the following chapter, a short introduction into the physics of graphene and graphene nanoribbons will be given. Starting from semimetallic 2D graphene sheets, it will be explained how it is possible to open up a bandgap in graphenic materials and the electronic properties of GNRs will be discussed. The last part of this chapter gives a short overview of state-of-the-art research in the field of graphene nanoribbons to put the experimental results given in chapter 5 into context.

### 3.1 Graphene

Purely carbon based materials, mainly graphite crystals, have been in the focus of research works for well over 100 years.<sup>[44]</sup> Their lamellar structure was soon discovered and led the groundwork for theoretical works, predicting physical and electronic properties of single, two-dimensional carbon sheets.<sup>[45-47]</sup> Such two-dimensional layers, consisting of  $sp^2$ -hybridized carbon atoms covalently bound in a hexagonal lattice, were at first theoretically predicted to be unstable when isolated. They would supposedly relax into other, three-dimensional folded configurations upon extraction from the graphite crystal.<sup>[48,49]</sup> With the first experimental observation of freestanding graphene by Novoselov and Geim in 2004,<sup>[6]</sup> these predictions were refuted. Using a highly ordered pyrolytic graphite (HOPG) crystal, they managed to eventually extract single layers of graphene with the use of simple scotch tape by repeatedly separating the layers from each other until they were left with a single two-dimensional sheet. On such isolated layers they were able to experimentally investigate the theoretically predicted outstanding physical and electronic properties.<sup>[8]</sup>

A freestanding 2D layer of graphene consists of  $sp^2$  hybridized carbon atoms, arranged in a hexagonal lattice with a lattice constant of 246 pm.<sup>[50]</sup> In this configuration, each atom forms three  $\sigma$ -bonds with its in-plane neighbors through electrons in the  $2s$ ,  $2p_x$  and  $2p_y$  orbitals and the  $2p_z$  orbitals, which are oriented perpendicular to the plane, form  $\pi$ -bonds. Electrons in the so formed  $\pi$ - and  $\pi^*$ -bands are delocalized and effectively form a two-dimensional electron gas, which is responsible for the outstanding electronic properties of graphene.<sup>[51]</sup>

The band structure for single layer graphene can be easily calculated within a tight binding approach and is shown in figure 3.1. One can see that the conduction band (CB) and the valence

band (VB) are energetically separated at all points, except for the K and K' points, where they form so-called Dirac cones. These points, being a consequence of the lattice symmetry, result in a semimetallic character, making pristine graphene sheets unusable for the utilization in electronic devices. However, the linear dispersion relation near the K and K' points gives rise to exceptionally high charge carrier mobilities as a direct result of the electrons behaving as massless Dirac fermions.<sup>[7]</sup> The charge carrier mobility at room temperature is  $200\,000\text{ cm}^2\text{ V}^{-1}\text{ s}^{-1}$ <sup>[52]</sup> and therefore around four orders of magnitude larger than in common metals like Cu, Ag or Al. In combination with other unique properties like exceptional mechanical strength,<sup>[53]</sup> and thermal conductivity<sup>[54]</sup>, graphene has been a promising candidate for numerous applications.

While there exist some techniques to open up a bandgap in graphene sheets, the search for more customizable approaches is still ongoing. Since possible modifications to induce semiconducting properties always involve structural or chemical enhancement of the carbon lattice, they also affect its initial electronic properties. By doping graphene with heteroatoms like sulfur,<sup>[55]</sup> nitrogen<sup>[56]</sup> or boron<sup>[57]</sup>, it becomes a narrow bandgap semiconductor. The same result is achieved by chemically functionalizing the sheet<sup>[58,59]</sup> or by incorporating hexagonal boron-nitride domains into the lattice.<sup>[60]</sup> Stacks of two individual graphene sheets, called bilayer graphene have also been used to create devices based on the semiconducting properties of the combined material.<sup>[61–63]</sup>

Other modifications, that will open up a bandgap in graphene, involve controlled tuning of the morphology of the lattice. By confining the delocalized  $\pi$ -electrons laterally, a so-called graphene nanoribbon is created. Numerous studies provide compelling evidence that such thin strips of graphene, called GNRs, can exhibit a wide range of diverse physical properties, which depend strongly on the nanoribbons width and edge structure. As these ribbons will be the main topic of this thesis, an in depth discussion of the different modification methods and their influence on the electronic properties of GNRs will be given in the next chapter. The last method to mention here is the introduction of highly periodic vacancies into the lattice, i.e. the creation of porous graphene, which will also be discussed separately in section 3.3.5.

## 3.2 GNR synthesis

The lateral confinement of a two-dimensional graphene lattice can lead to the opening of a bandgap in the resulting graphene nanoribbon.<sup>[64]</sup> Such nanoribbons can be treated as quasi one-dimensional nanostructures, whose electronic properties can be tuned by tailoring the geometry and chemical composition of the structure. The first theoretical predictions about electronic properties of laterally confined graphene sheets were already made years before the experimental discovery of freestanding graphene. In the work of Nakada et al. the electronic properties of graphene nanoribbons were derived from tight binding calculations, which showed that the

bandstructure of narrow GNRs considerably differs from predictions based on the BZ of 2D graphene.<sup>[20]</sup> A simple approach would be that the conduction and valence band in graphene nanoribbons is approximately the projection of the 2D bandstructure of graphene onto a plane intersecting the Brillouin zone as shown in figure 3.1 **a**. The orientation of these planes can be constructed from the edge configuration of the GNR, depending on the direction in which the lattice was cut. However, the calculations of Nakada et al. showed that by reducing the width of the graphene strip, additional electronic states appear, resulting from the lateral confinement of delocalized  $\pi$ -electrons.

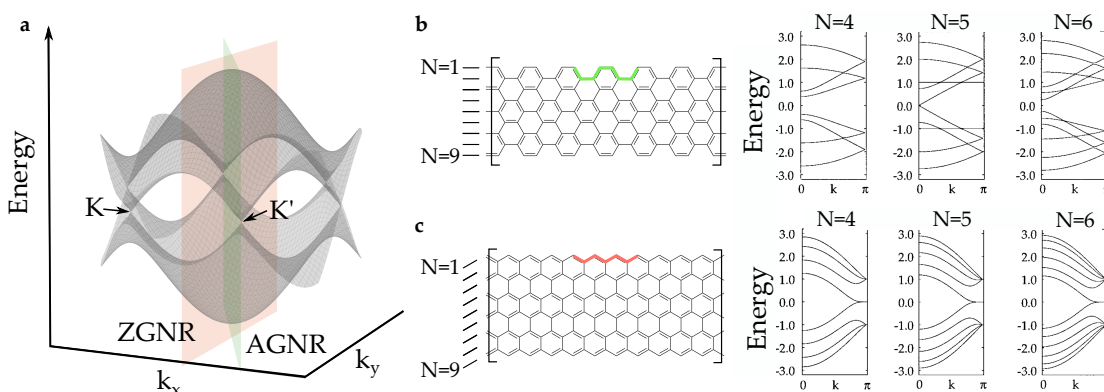


Figure 3.1: **a**) Representation of the 2D Brillouin zone of graphene (gray) with the valence band and conduction band meeting at the K and K' points. The red and green planes resemble the 'cutting' directions of AGNRs and ZGNRs through the BZ. **b**) and **c**) Chemical structure formula of AGNR and ZGNR with their calculated bandstructures for different widths  $N$ . Bandstructures taken from Ref. [20].

If one imagines a hexagonal lattice and tries to cut it down into thin strips, depending on the cutting angle, only two edge configurations can exist. These so-called armchair and zig-zag-edges have their names from their distinct appearance when looking at the atomic positions at the edges and result in completely different electronic properties of the respective GNRs.<sup>[23,65–68]</sup> Figure 3.1 **b** and **c** show armchair (AGNR) and zig-zag GNR (ZGNR) structures and bandstructures for different widths respectively. GNRs are characterized by their edge configuration as well as their width in terms of carbon atoms perpendicular to the edge. In figure 3.1 **b** for example, a 9-AGNR is shown while **c** shows a 9-ZGNR, where the 9 resembles the number of atomic rows in each structure.

Looking at the bandstructures of the GNRs in figure 3.1 **b** and **c**, one can see that the bandstructures do indeed look very different for both types of GNRs. These were calculated by using a tight-binding approach within the Hückel approximation, with numbers  $N$  on top of each bandstructure resembling the width of the ribbon. ZGNRs appear metallic and therefore show no bandgap, whereas AGNRs exhibit a direct bandgap for  $N = 4$  and  $N = 6$ . This result is

rather surprising and can not be explained by the simple model that has been mentioned above. If one imagines the simple projection onto the planes, every GNR should have metallic character because of the contact of VB and CB at the K points. To explain the opening of a bandgap one has to look closer into the electronic structure of GNRs. The bandgap in AGNRs is a result of the lateral confinement of electrons in the delocalized  $\pi$ -system of the structure. It therefore explains why the bandgap width is strongly dependent on the width of the GNR.<sup>[20,21]</sup>

Z-GNRs are often ruled out as suitable structures for the use in electronic devices because of their metallic nature. However, other electronic properties, like the existence of localized edge states<sup>[19,20]</sup> and spin polarized states<sup>[69,70]</sup> make them subject of multiple studies and possibly useful for new carbon based spintronic devices. In this work the focus lies on the synthesis of novel GNRs which have pristine or modified armchair edge configurations, a detailed discussion of ZGNRs will therefore be spared here.

For armchair GNRs, theoretical studies following the work of Nakada et al. found a systematic behavior of the electronic bandgap on the ribbon's width.<sup>[23,37,71]</sup> All of which showed that the number  $N$  of atomic rows in a ribbon always belongs to one of three groups. Depending on  $N$  belonging to the  $3p$ ,  $3p + 1$  and  $3p + 2$  group, where  $p$  is an integer, the electronic properties are significantly different, with only the  $3p$  and  $3p + 1$  group showing a significant bandgap width dependence on the ribbon's width. This is consistent with figure 3.1 **b**, which shows that the bandstructure for  $N = 5$  shows no bandgap. This also explains the findings in figure 3.1 **b**, where the bandstructure for  $N=5$  shows no bandgap. If a bandgap is present, its width increases with decreasing ribbon width, which can easily be explained by treating the lateral confinement of the  $\pi$ -electron system as a particle in a box problem. For greater widths ( $N \geq 30$ ) Nakada et al. showed that the bandstructure approaches the above-mentioned projection of the 2D BZ of graphene onto a plane.<sup>[20]</sup>

The early approaches to produce graphene nanoribbons used top-down methods, starting from larger structures like two-dimensional graphene sheets or carbon nanotubes (CNT) and changing their structure and/or size by physically or chemically attacking the lattice. Single or multi-walled CNTs of different radii were chemically unzipped<sup>[72–75]</sup> and large graphene sheets have been cut down to narrow strips using electron beam lithography<sup>[24,76,77]</sup> or other chemical etching techniques.<sup>[78–82]</sup> Even though these approaches were spatially precise, the resulting nanoribbons showed nonuniform edge configurations and structural variations which shows that, without downplaying the importance of these results, that they were suboptimal for the production of structurally precise GNRs.

Atomic precision for the synthesis can only be achieved if individual precursor molecules are used from which the structure is then built using a bottom-up approach. Such techniques were already well established for the synthesis of large polymer structures and in the field of biomolec-

ular research but had not been used for the synthesis of narrow GNR structures before.<sup>[83–85]</sup> The use of specifically designed precursor molecules then led to the first synthesis of well-defined 9-AGNRs in solution by Yang et al. in 2008.<sup>[86]</sup> This motivated a numerous research works, to develop this approach further and improving the molecular weight and yield of the chemical reactions.<sup>[87–97]</sup> This solution-based synthesis route resulted in a variety of GNRs with different widths, edge structures and functionalizations. For structural characterization, high resolution scanning probe techniques are used. However, it is therefore necessary to place the molecules onto clean surfaces, which is particularly difficult for GNRs synthesized in solution. The strong aggregation tendency of GNRs in solution, which stems from the interribbon  $\pi$ - $\pi$  interactions, and also the contaminants present on GNR structures due to residue from the solution synthesis make it hard to achieve sufficient spatial resolution on individual GNRs.

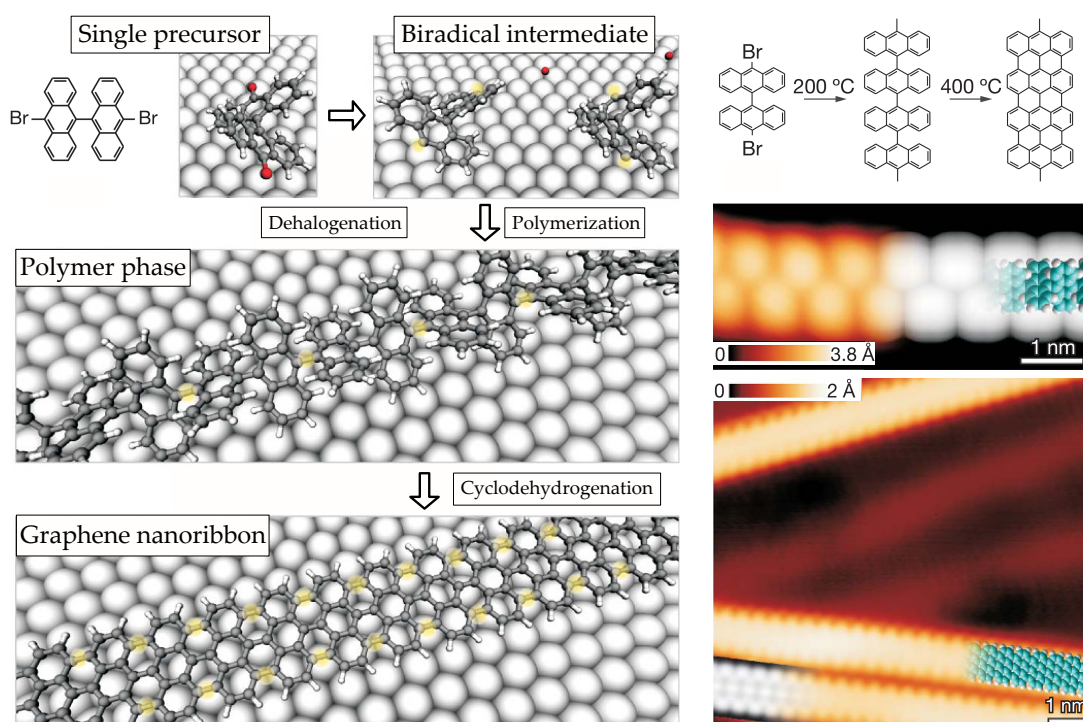


Figure 3.2: Graphical representation of the individual reaction steps for the on-surface synthesis of 7-AGNRs. The two STM images on the right side show the polymer phase and fully cyclized GNRs on a Au(111) surface. Adapted from Ref. [26]

A breakthrough in structural precision has been achieved by using a surface assisted synthesis route, where molecular self-assembly and temperature controlled coupling reactions are used to form GNRs out of individual precursor molecules.<sup>[98,99]</sup> This procedure was first employed by Cai et al. in 2010,<sup>[26]</sup> laying the groundwork for a whole new field of research. The precursor

molecules, which are chemically synthesized by design, are usually deposited onto clean metal single crystals in a UHV environment using thermal evaporation. The halogenated precursors then undergo dehalogenation upon a first annealing step, where the temperature of the sample is increased slightly to break carbon-halogen-bonds and leave biradical intermediates on the surface. These biradicals are free to diffuse over the crystal surface and form polymer chains through self-assembly by covalently coupling at the previously halogenated sites. The exact location and number of halogen functionalizations on each precursor molecule is therefore of utmost importance for the resulting structures. A second annealing step then leads to the planarization of the molecular chains by surface assisted dehydrogenation. The individual reaction steps are graphically shown in figure 3.2 together with two STM images showing the polymer phase and the fully cyclized 7-AGNRs on Au(111). This method provides a viable tool to change the geometry and chemical composition of the resulting structures based on differences in the precursor design, enables the investigation of individual ribbons with surface science methods and also minimizes contamination due to the UHV environment.

### 3.3 State of the art on-surface GNR reserach

In the following, a short summary of recent advances in the field of on-surface bottom-up synthesis of graphene nanoribbons will be given. This short overview will help to set the presented results into context, to show how fast the field is moving and in which direction it is headed.

#### 3.3.1 Substrates

The on-surface synthesis of GNRs requires the use of metal single crystals like Au, Ag or Cu, as catalytic substrates to promote the on-surface reactions. Depending on the substrate, the reaction temperatures can vary strongly,<sup>[100-102]</sup> and the use of the same precursor molecules does not necessarily result in the same GNR structure.<sup>[35,103,104]</sup> They can also influence the growth of the GNRs by acting as templates, where the resulting structures grow epitactically,<sup>[102,105]</sup> or align with the morphology of the substrate.<sup>[106-108]</sup> Recent developments also involved the use of Au/Mica substrates, which are cheaper and can therefore be destroyed when the GNRs are transferred to other substrates for device fabrication.<sup>[109-111]</sup> Placed on pure metallic substrates, the electronic structure of GNRs can be probed however one has to keep in mind that the measured spectra always deviate from the bandstructure of isolated ribbons since the interaction with the substrate modifies the electronic states. To circumvent this problem, methods have been developed to intercalate on-surface synthesized GNRs with Si,<sup>[112-114]</sup> or to move them with the tip onto NaCl-islands,<sup>[115]</sup> which isolates them from the surface.

#### 3.3.2 Bandgap engineering

The main focus when synthesizing novel GNRs lies on the improvement of their electronic properties. Different variations in the GNR architecture result in shifts of the valence and/or conduction band and thereby directly affect the bandgap width. To verify the predicted width dependent bandgap, postulated by Son et al.,<sup>[23]</sup> different widths of armchair GNRs were synthesized using special precursor molecules,<sup>[116–120]</sup> showing good agreement of the measured bandgap widths with the theoretical calculations. But it is not just the width of the structure that influences the bandgap. Structurally different edges do also strongly change the GNRs bandgap width and also give rise to localized electronic states.<sup>[121–124]</sup>

Another method to alter the bandgap is by integrating heteroatoms into the GNR structure. The dopant atoms like nitrogen, boron or sulfur are therefore built into the individual precursor molecules to get a perfect periodic arrangement inside the synthesized GNR. It was found that nitrogen doping tends to shift the CB and VB edges to lower energies,<sup>[125,126]</sup> while the bandgap width remains unchanged. Boron and sulfur dopant atoms, only have small effects on the bandgap,<sup>[127–130]</sup> but still modify the electronic configuration. This shows when more than one heteroatom species is employed. Also, N-, O- and S-doped chevron GNRs show a significantly smaller bandgap than pristine chevron GNRs,<sup>[131]</sup> and B-N-doped 9-AGNRs presented a shifted VB edge towards higher energies.<sup>[132]</sup>

#### 3.3.3 GNR heterojunctions and topological states

With the above-mentioned structural and chemical modifications, it is possible to produce a variety of different GNRs which can either be p-type or n-type semiconductors, depending on the location of the VB and CB edge. Combining two such structures into one heterostructure, creates a p-n-junction that behaves very similarly to a traditional one.<sup>[126]</sup> Different efforts have been made to produce GNR heterojunctions, including the simple use of structurally different precursor molecules,<sup>[133,134]</sup> a hierarchical synthesis process controlled by varying halogen atoms,<sup>[135]</sup> a subsequent modification of the structure with the STM Tip<sup>[136]</sup> or simply the lateral combination of similar GNRs into wider segments.<sup>[137,138]</sup> In some of the experiments, localized electronic states at the heterojunctions were found that locally change the bandgap create additional channels for charge transport.<sup>[139,140]</sup> Those states are a direct result of topological effects in the junction and can also be periodically formed.<sup>[141–143]</sup>

#### 3.3.4 Device fabrication

Regarding future applications of graphene nanoribbons in electronic devices, there are a variety of different technical instruments, where GNRs and GNR heterostructures can be employed. The

possibility to construct p-n-junctions with atomic precision led to the construction of first GNR field effect transistors. These devices provide improved charge carrier mobilities and thermal conductivity compared to established silicon based FETs.<sup>[111,144–147]</sup> The existence of topological states also makes it possible to construct GNR based spintronic devices<sup>[148,149]</sup> or to use them for the construction of quantum information devices, as high quality single photon emitters.<sup>[150,151]</sup> Simpler applications involve GNR based gas sensors,<sup>[152–154]</sup> or photodetectors.<sup>[155,156]</sup> This shows how versatile GNRs really are and that future developments might lead to new innovative devices.

### 3.3.5 Porous GNRs

As it is particularly interesting for this thesis, an overview of the small number of studies that focused porous graphene nanoribbons and porous nanographenes will follow. Some early works started with the preparation of porous graphene sheets by using lithography methods,<sup>[157,158]</sup> or molecular self-assembly.<sup>[159,160]</sup> Unfortunately all of those studies focussed on the application of porous graphene sheets but not on the electronic properties. Theoretical studies then predicted that periodic nanopores in graphene and graphene nanoribbons will open up or in the case of GNRs influence the bandgap width.<sup>[160–163]</sup> Even though these studies suggested the implementation of nanopores as a highly valuable tool for the electronic modification of GNRs, just very few studies are accessible to date that experimentally utilize this effect. Recent studies of Pawlak et al. and Ajayakumar et al. report the synthesis of porous GNRs, however both lack an experimental determination of the bandgap width.<sup>[164,165]</sup> For the synthesis of porous nanographenes the number of published research works is also very limited. Some studies employed single precursor molecules for the synthesis of small porous nanographenes.<sup>[166,167]</sup> However the most promising results came from Jacobse et al. by using individual parallelly aligned graphene nanoribbons and fusing them together laterally.<sup>[168]</sup> With this method, relatively large porous nanographenes can be synthesized in situ which are atomically precise and provide periodically located pores of similar size. In their study however, they found an additional in-gap electronic band in the fused PNG structures. This corresponds to an effective decrease in bandgap width due to this new electronic state that emerges when individual GNRs are fused.

## 4 Experimental details

In the following chapter, the experimental setup used in this work will be presented. First, a short introduction into ultrahigh vacuum conditions will be given to provide the necessary background. Then the used low temperature scanning tunneling microscope with all its components will be explained in detail. Other necessary information like the experimental setup to conduct STS experiments with this system as well as sample and tip preparation techniques will also be discussed here. Within the scope of this work, a new approach for the synthesis of self-assembled nanostructures was invented, which is based on the diffusive motion of single molecules on clean metal surfaces. The findings of these experiments together with a theoretical model for surface diffusion processes will also be presented. The resulting nanostructures will be discussed in detail in chapter 5.

### 4.1 Ultrahigh vacuum

To conduct surface science experiments, it is crucial to minimize contamination of the sample. It is therefore necessary to use ultrahigh vacuum (UHV) systems, in which the residual gas pressure inside a vacuum chamber is reduced to  $p \leq 10^{-9}$  mbar. Reducing the pressure by 13-14 orders of magnitude relative to ambient pressure is a technically demanding process and requires the use of several pumps. Each vacuum pump is able to create a pressure gradient between its intake and exhaust, which is why by connecting these pumps in series the desired absolute pressure can be reached.

Starting at ambient pressure of  $p = 10^3$  mbar the first set of pumps to use usually consists of oil sealed rotary pumps, which reduce the pressure to  $p = 10^{-3}$  mbar. These pumps are able to take high gas loads, but are inefficient in pumping lighter gases like  $H_2$ . After letting the rotary pumps run for a couple of minutes, the base pressure is reached and the turbomolecular pumps can be started. The pumping mechanism in these pumps is based on momentum transfer from the rotor blades, rotating at a speed of  $6 \times 10^5 \text{ min}^{-1}$ , to residual gas molecules. Therefore heavier gases like  $N_2$  and  $O_2$  are pumped efficiently, while pumping  $H_2$  remains challenging. When the molecular motion of residual gas atoms leaves the continuum regime, because the mean free path of individual molecules gets larger and larger, the mechanical pumping mechanism requires gas

molecules to randomly find their way into the pump and a further reduction therefore takes an increasing amount of time. The turbomolecular pumps are able to reduce the pressure inside the UHV system to  $p = 10^{-8}$  mbar, at which point the residual gas pressure comes almost exclusively from  $H_2$  and  $H_2O$ . Hydrogen gas molecules are so small that they are able to diffuse through the turbomolecular pump and the residual water pressure stems from water being trapped inside the chamber walls. When the pressure is reduced to the high vacuum regime ( $p \approx 10^{-8}$  mbar), trapped gas molecules inside the chamber walls start to desorb into the vacuum.

To achieve UHV conditions, two further steps are necessary. The first one being the need of a bakeout. To remove trapped residual gas molecules from the chamber walls, the only possibility is to increase the desorption ratio by baking the whole system at increased temperatures for several hours. To realize this, the complete system is either wrapped with heating cords or a isolated stainless steel box is built around the system, and it is baked at  $T = 150$  °C. Throughout the whole process, the rotary pumps and turbomolecular pumps are connected to the chamber to remove the released gas molecules. After the system is cooled down again, the residual gas pressure of  $H_2O$ , should be reduced below  $p = 10^{-11}$  mbar. However, the pressure of the whole system will still be  $p \approx 10^{-8}$  mbar, since hydrogen is still able to diffuse through the turbomolecular pump into the system. At this point, the turbomolecular and rotary pumps are disconnected via a gate valve and a third set of pumps is used to reduce the pressure further.

In these pumps, residual gas molecules are trapped chemically instead of being removed from the system by transporting them to an exhaust. Ion getter pumps (IGP) are able to ionize residual gas atoms, which are forced onto circular orbits by a strong magnetic field, following the Lorentz force law. They are then trapped inside circular titanium tubes inside the pump. Titanium, being a strong getter material by chemically binding the residual gas, is also used in titanium sublimation pumps (TSP), where titanium filament rods placed inside the vacuum chamber are heat up by Joule heating until they start to sublime and thereby coat the chamber walls in a small layer of titanium atoms. Residual gas atoms hitting the chamber walls are then chemically bound by this titanium layer. When the layer is saturated, it can usually be noticed by an increase in pressure and a new layer of titanium has to be produced.

After switching on the last set of pumps and disconnecting the mechanical pumps, it still takes a couple of hours to reduce the pressure to  $p = 10^{-11}$  mbar. This shows that creating a UHV environment is technically demanding and highly time-consuming. Table 4.1 is meant to underline the necessity of UHV conditions for surface science experiments, as it sets the base pressure of a UHV system into relation to the arrival time of a monolayer of residual gas atoms on a clean sample surface.

In table 4.1, different parameters important for UHV experiments are shown in relation to each other. Where especially the mean free path  $\lambda$  and the monolayer arrival time  $\tau$  should be discussed

Pressure $p$ in mbar	Molecular density $n$ in $\text{cm}^{-3}$	Arrival rate $J$ in $\text{cm}^{-2} \text{s}^{-1}$	Mean free path $\lambda$ in m	ML arrival time $\tau$ in s
$1 \cdot 10^3$	$2 \cdot 10^{19}$	$3 \cdot 10^{23}$	$7 \cdot 10^{-8}$	$3 \cdot 10^{-9}$
$1 \cdot 10^0$	$3 \cdot 10^{16}$	$4 \cdot 10^{20}$	$5 \cdot 10^{-5}$	$2 \cdot 10^{-6}$
$1 \cdot 10^{-3}$	$3 \cdot 10^{13}$	$4 \cdot 10^{17}$	$5 \cdot 10^{-3}$	$2 \cdot 10^{-3}$
$1 \cdot 10^{-6}$	$3 \cdot 10^{10}$	$4 \cdot 10^{14}$	$5 \cdot 10^0$	$2 \cdot 10^0$
$1 \cdot 10^{-9}$	$3 \cdot 10^7$	$4 \cdot 10^{11}$	$5 \cdot 10^3$	$4 \cdot 10^3$

Table 4.1: Different important parameters for UHV experiments showing the dependence on the base pressure  $p$ . This table was adapted from Ref. [169]

in more detail. As a measure for how long a residual gas molecule travels through the vacuum before colliding with another molecule,  $\lambda$  can be taken into account to estimate the interaction of residual gas molecules to be negligible. One can also conclude that under UHV conditions, where  $\lambda \approx 5$  km, the molecules will most likely hit the chamber wall first, being trapped by the titanium layer supplied by the TSP. The monolayer arrival time  $\tau$  shows how long it takes before a clean surface is covered with a monolayer of residual gas molecules. This is of course just an estimate value since not every molecule hitting the surface will also be adsorbed, however it gives an idea in which order of magnitude experiments should be conducted timewise. In the case of this particular system, where the base pressure is  $p = 10^{-11}$  mbar, the monolayer arrival time is about 24 h.

## 4.2 Low temperature scanning tunneling microscope (LT-STM)

The theoretical consideration of the tunneling process with an STM has been discussed in chapter 2. However, scanning tunneling microscopes come in a variety of different setups, which is why the exact experimental system used in this work will be explained in detail here. The UHV system has been purchased from the University of Nebraska-Lincoln in 2019, and was then transferred and set up in the laboratory in Bayreuth. Due to the fact that the refurbishment represents a significant part of the experimental work of this thesis, a short introduction into the history of this particular system will be given first.

Figure 4.1 shows an image of the UHV system consisting of two vacuum chambers and a large cryostat assembly. The STM itself is located inside the analysis chamber and is attached to a liquid helium cryostat for low temperature measurements at  $T = 4.2$  K. The LT-STM system was initially purchased as a first generation built from Scienta Omicron in 2007. At this time,

the group of Prof. Enders was still located at the University of Nebraska-Lincoln. The system in its original form just consisted of the analysis chamber, the LT-STM and a Load-lock unit to introduce samples and was extended in the following years by an additional preparation chamber and a manipulator to spatially separate the sample preparation process from the sensitive STM.

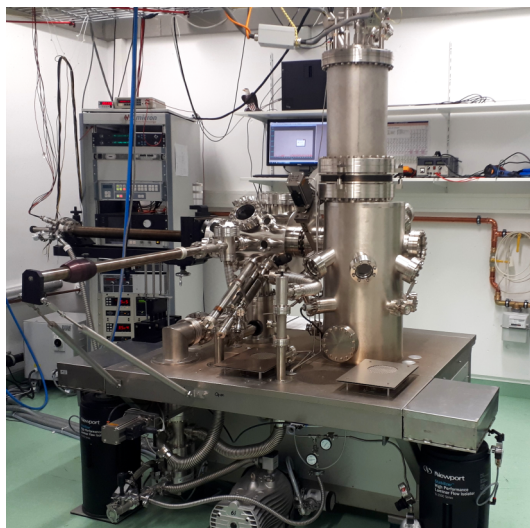


Figure 4.1: Photograph of the UHV system with all its components and peripheral systems attached.

In this configuration the system was used for 12 years, until in 2019 the decision was made to transfer it to the new laboratory in Bayreuth. As all the preparations had been made, I went to Lincoln in July 2019, disassembled the system into manageable parts and packed everything up for shipping. As the boxes arrived in Bayreuth in August 2019, the reinstallation of the system had been started while simultaneously improving outdated systems. After the arrival in Bayreuth, the instrument required extensive refurbishment and repair, which took more than 8 months.

The following section will give an overview of all the relevant parts of the UHV system. Figure 4.2 shows a schematic drawing of the complete UHV system. Vacuum pumps and pressure gauges are not shown here for simplicity. The connections between all the components are copper sealed ConFlat flanges in different sizes which are best suitable for UHV applications with a leak rate of  $\leq 10^{-11}$  mbar s $^{-1}$ . A dry scroll vacuum pump (Edwards, nXDS6i) and a turbo pump (Pfeiffer Vacuum, HiPace350) are connected to the Load-lock and the preparation chamber to provide high vacuum conditions and to absorb high gas loads if necessary. Inside the stainless steel table, on which the vacuum chambers are mounted, an IGP (Agilent, Vacion Plus 150) is mounted below each chamber to allow for separate pumping and to maintain UHV conditions even if the other pumps are turned off. The two TSP are located at the bottom of each chamber respectively. Also built inside the table are the heating elements, which heat up the system to  $T = 150$  °C during bakeout. To assure consistent temperature of all system parts during that process, the temperature is held for at least 48 hours. This is especially important since the STM is thermally decoupled from the rest of the system through the cryostats and therefore takes several days to reach the desired temperature.

The preparation chamber ① and the analysis chamber ② are separated by a pneumatic gate valve ③. Thereby, processes producing a high gas loads can be performed in the preparation chamber without contaminating samples stored in the analysis chamber. When a sample is

introduced from outside the system it is first placed in the Load-lock (4), a small chamber separated from the rest by a gate valve. Pumping the chamber for several hours ensures desorption of most ambient residuals before transferring the sample into the manipulator (5) via a magnetically coupled transfer arm (6). In the manipulator, the sample is held in a specially designed heating stage, which is equipped with an electron beam heating assembly to heat up the sample plate. Temperatures well over 1300 K can thereby be reached, which is often necessary for crystal cleaning purposes or to initiate certain chemical reactions on a sample.

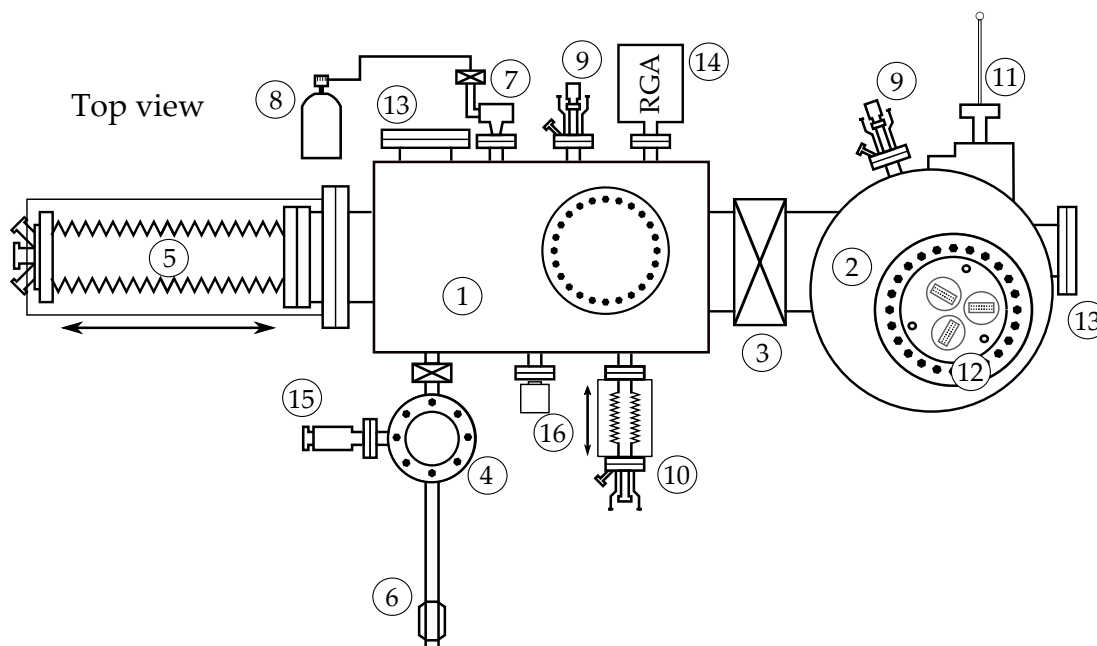


Figure 4.2: Schematic top view of the UHV-system layout. The most important components are numbered.

An ion gun (PREVAC, IS 40C1) (7) is attached to a supply of high purity argon gas (8) through a precision leak valve to clean metal single crystal substrates. The details of the cleaning procedure will be described in section 4.4.1. The system is equipped with two metal evaporators (Focus, EFM 3) (9) and a home built organic evaporator (10) to deposit different kinds of molecules and atoms onto the crystal surface. By varying evaporation parameters such as temperature and evaporation time, different coverages of the desired molecules on the surface can be achieved. A quartz microbalance is attached to the front of the manipulator head to calibrate these evaporators. It is based on an oscillating quartz crystal plate, whose resonance frequency changes when atomic layers of different molecular weights are deposited onto it. This enables precise measurements of the deposited amount of molecules per time with sub monolayer precision. One of the metal evaporators is mounted directly onto the analysis chamber, pointing right at the microscope. With

this setup, it is possible to deposit hot metal atoms onto the cold sample directly inside the STM.

When the sample preparation is finished, the crystal is transferred into the analysis chamber by the manipulator and picked up with the wobble stick (11), which is a bellow sealed device for manual sample manipulation via a pair of pliers mounted on the vacuum side. The wobble stick allows for a precise placement of the sample in the STM stage, which is mounted at the bottom of the combined LN<sub>2</sub>-/LHe bath cryostat (12). Both cryostats and the STM assembly are shown in detail in figure 4.3. Multiple viewports (13) allow for direct visual contact with the sample from outside the chamber. A residual gas analyzer (14) is attached to the preparation chamber to monitor the composition of the residual gas inside the chamber and thereby detect leaks early on. It is also used to check the purity of the argon gas for the ion gun, since contaminations in the filling lines or the valves can lead to the deposition of those onto the sample.

As will be described in more detail in section 4.6, oxidized tungsten tips need to be annealed at high temperatures in UHV to reduce the oxide layer. Since during this annealing process high gas loads arise due to the increased temperatures of the tip, tip holder and tip carrier, it was relocated from the analysis chamber into the Load-lock to minimize contamination. Therefore, a special tool (15) for direct contact heating of the tip was developed, with which the tip wire can be precisely contacted near the apex to allow direct current heating. For sample preparation, it is inevitable to have precise knowledge about the sample temperature during annealing processes. In UHV systems it is very difficult to implement direct temperature measurements via thermocouples because of the inaccessibility of the sample and poor thermal contact. As a solution, an infrared thermometer (Optris, CTlaser 3MH1) (16) was installed on the system to measure the temperature contactless. Therefore, a viewport with special transmission characteristics had to be installed to get a correct measurement. The interval of measurable temperatures of the IR thermometer ranges from  $T = 150\text{ °C}$  to  $T = 1000\text{ °C}$  corresponding to wavelengths between  $\lambda = 2.3\text{ }\mu\text{m}$  and  $\lambda = 10\text{ }\mu\text{m}$ .\* Since usual quartz glass viewports show poor transmission values for larger wavelengths, a ZnSe viewport was purchased, which shows nearly constant transmission values between  $0.5\text{ }\mu\text{m}$  and  $15\text{ }\mu\text{m}$  and is therefore perfectly suitable for this application.

All components are mounted on a stainless steel table, which can be decoupled from the ground by engaging three pneumatic dampers (Newport, S-2000 Series). This vibrational isolation is very effective against low frequency noise such as building vibrations and low frequency acoustical noise. The STM itself is also decoupled from the rest of the system during measurements via a spring mechanism, which is described in more detail below. All the listed components are either necessary to ensure stable operation conditions for the STM or are used for sample and tip preparation. However, the LT-STM itself is the most important part of the system. In figure 4.3, a detailed schematic drawing as well as two photographs of the actual STM are shown and the

---

\*Approximating the used metal single crystals as ideal black bodies.

individual parts of the microscope are numbered.

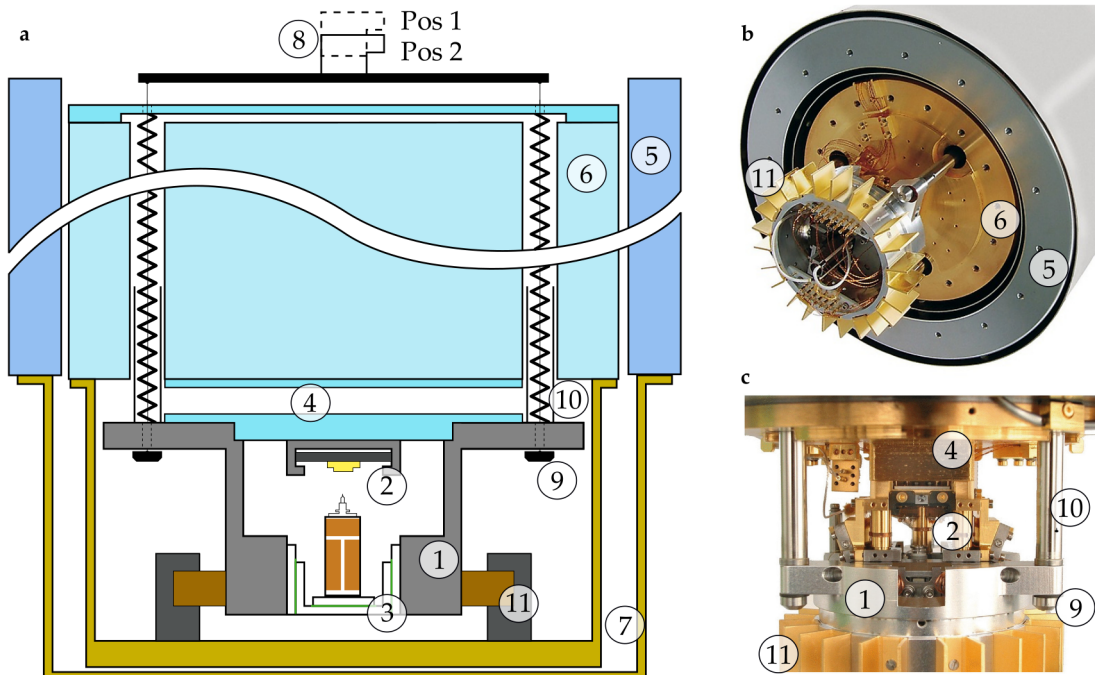


Figure 4.3: **a)** Schematic drawing of the LT-STM and cryostat setup. **b)** Photograph of the LT-STM from below. **c)** Photograph of the LT-STM from the front. Both taken from Ref. [170]. The cryogenic cups of both cryostats are not attached in **b** and **c**.

The scanning tunneling microscope consists of a rigid metal body (1) in which all the main components are mounted. When the sample is introduced into the STM from the manipulator, it is placed in the sample stage (2) which is located directly above the piezoelectric scanner tube. The STM tip is mounted on top of this tube. It is made out of a piezoelectric material and is divided into segments by electrodes. When a voltage is applied between any one of these contact surfaces and the inside of the tube, it causes the material to lengthen/shorten and therefore the tube to bend. The tip can therefore be moved in three dimensions across the sample surface with sub pm precision. Of course this movement is spatially very limited which is why for a macroscopic motion of the tip and scanner, the assembly is mounted on top of the course motion drive (3). The course motion is built on the basis of piezoelectric sliding motors, which enable coarse positioning of the tip in the x- and y- direction as well as to bring the tip into close contact with the sample surface before starting the automatic tip approach. This automated process brings the tip into tunneling contact with the surface without crashing by using a step wise approach where the course motion drive and the z-piezo element act synchronized.

On top of the sample, a thermal contact plate (4) is mounted, which guarantees for good thermal

contact between the microscope and the LHe-cryostat. Both of the cryostats are mounted above the STM, with the LN<sub>2</sub>-cryostat (5) mounted on the outside and the LHe-cryostat (6) on the inside. Both are about 70 cm in length to provide enough volume to guarantee a possible operation time of 48 hours before refilling. After refilling, it takes about 3 hours until the liquid nitrogen stops to boil and the STM can be operated without induced vibrations from the cryostats. Each cryostat is mounted free hanging on its filling lines and has no mechanical contact with the chamber or the other cryostat. This also ensures minimized vibrational intake as well as thermal isolation of the LHe-cryostat. Cryogenic copper cups (7) are mounted at the bottom of each cryostat to thermally shield the microscope from its surroundings. For rapid cooldown, the STM is pressed against the LHe-cryostat by a spring-loaded locking mechanism (8) to provide proper thermal contact. However during measurements, this mechanism is brought into position 2, which releases the stainless steel cables (9) and suspends the STM on three long springs (10). If the system is aligned perfectly, the STM as well as the springs do not touch the rest of the system anywhere except for the attachment points inside the LHe-cryostat. However, since the springs are extremely long to provide sufficient vibrational isolation, they are also very smooth, which is why low frequency oscillations of the suspended system have to be damped by an eddy current damping mechanism (11). As can be seen in figure 4.3 **b** and **c**, a ring of copper brackets is mounted at the bottom of the STM. This ring comes to rest in an array of permanent magnets mounted inside the LHe-cryogenic cup in the suspended position. Any movement of the STM is thereby directly damped out because of eddy currents induced by this damping mechanism.

In this configuration, the system is able to operate for hours without thermal drift or induced vibrations with a z-resolution in the order of  $\approx 1$  pm, which is 200 times smaller than the height of a monoatomic gold step edge.

Even though the system is specified for operation at 4.2 K it is usually operated with both cryostats filled with liquid nitrogen. The increased temperatures are not expected to change the outcome of the experiments significantly and additionally, the handling of liquid nitrogen is easier.

### 4.3 Scanning tunneling spectroscopy setup

While in section 2.2 the theory behind scanning tunneling spectroscopy was explained, this section will focus more on the experimental aspects of the measurement of  $dI/dV$  point spectra and  $dI/dV$  maps here. A wiring diagram for all electronic components needed is shown in figure 2.3. To generate the modulation signal, an external function generator (Keysight, 30500B) was used, which is able to supply small amplitude sine waves with high precision. The built-in signal generator of the Lock-In amplifier (Stanford Research Systems, SR830 DSP) was not used for this work, because it starts to distort the output sine wave signal at amplitudes below  $V_{\text{mod}} = 5$  mV.

In this particular setup, the signal coming from the preamplifier of the STM has to be attenuated since it can sometimes exceed the maximum input level of the Lock-In amplifier. Higher tunneling current setpoints are beneficial when taking spectroscopic measurements, since the signal-to-noise ratio is increased. By using a 10:1 attenuator, it is possible to collect data at higher current setpoints up to 1 nA without overloading the Lock-In amplifier. When the signal is fed back into the Matrix CU via the auxiliary input, it can be observed in real time while simultaneously taking  $I$ - $V$  measurements.

The actual values set on each device are listed in section 7.1. These values were determined by looking at noise levels, signal amplitudes and energetic resolution and will have to be fine-tuned for individual measurements. Especially the characteristic times set on the Lock-In amplifier and in the software have to be altered carefully by keeping in mind that modulation frequency, demodulation time constant and the raster time of the STS spectrum always have to be adjusted with respect to each other. The condition given by equation (2.6) has to be fulfilled no matter if  $dI/dV$  point spectra or  $dI/dV$  maps are acquired. For the measurement of point spectra,  $T_{\text{Raster}}$  is set directly, but for  $dI/dV$  maps the scan speed per line has to be adjusted accordingly. The raster time at every pixel of the map can be calculated via

$$T_{\text{Raster}} = \frac{\text{scan speed in s}}{\text{points per line}}.$$

Since changing the scan speed also changes the image quality, tip response and thermally induced drift during the duration of one frame, it has to be adjusted for every measurement and a compromise between image quality and signal-to-noise ratio in the spectroscopic measurements has to be found. The modulation frequency should also not exceed values of  $f_{\text{mod}} = 5$  kHz, thereby limiting the minimum raster time of the measurement. The only solution is to let the STM equilibrate for several hours before taking measurement to reduce thermal drift. This way it is possible to set the measurement duration of one frame in the order of one hour and thereby achieve maximum signal-to-noise ratio and image quality. Of course, this also shows how time-consuming the process of  $dI/dV$  mapping really is and that it is immensely important to prepare the measurement thoroughly.

In the theoretical derivation of the  $dI/dV$  signal in section 2.2 the assumption was made that the DOS of the tip is constant in the energy interval of the measurement and followed that the spectrum only contains information about the sample DOS. This is however not initially true, and the DOS of the tip should be checked frequently during measurements. This can be done by measuring individual  $dI/dV$  point spectra on a clean substrate area and comparing the result to expected spectra for pristine metal surfaces. The exact methods used to prepare the tip are described in section 4.6 and will not be described here. Only when the measured point spectra

show no tip artifacts or strange peak structures should the tip be used for STS measurements.

## 4.4 Sample preparation

The accuracy of STM measurements requires that samples are also prepared with great precision and cleanliness. This led to the question, how substrate surfaces can be prepared to make them usable for such a sensitive surface science method. In the following chapter, the necessary processes to achieve atomically flat and clean metal surfaces will be discussed and a detailed description of molecular deposition methods onto those surfaces will be given.

### 4.4.1 Substrate cleaning

Metal single crystals are frequently used as substrates in STM experiments, since they provide reproducible surfaces that can be used multiple times for sample preparation. In this section, the cleaning procedure for such crystals will be discussed, as it is of utmost importance to reset the surface into a well-defined state before using them again as substrates. The procedure is generally the same for all such crystals. It consists of repeated cycles of ion bombardment and thermal annealing, where the damage done by the impacting ions is repaired. In section 4.2 it has been already mentioned that the primary purpose of the ion gun mounted on the preparation chamber, is to be used for sample cleaning.

In this gun, argon ions are created and accelerated and form a focused ion beam. If the substrate is placed in front of this gun, the ions hit the surface and can thereby clean it from any contaminations. This process is called sputtering and, depending on the chosen ion energy, can be very gentle to minimize surface damages or can leave a heavily damaged surface with argon ions even penetrating into the bulk structure of the crystal. For this reason, noble gas ions are used for the sputtering process, since their inert nature minimizes the chance of unwanted covalent bonding between them and the substrate. High ion energies of up to 5 keV can be necessary for several reasons, for example if an oxide layer which is usually strongly bound to the crystal structure has to be removed. After the ion bombardment, the surface will therefore show a lot of defects and needs to be recovered by thermal annealing. Increasing the temperature of the crystal high enough will eventually mobilize surface atoms, which can then diffuse across the surface and heal such defects. Thereby supporting the formation of equilibrium structure of the crystal surface, which is typically a flat with a precise atomic oriented. In addition, it also leads to bulk diffusion of embedded argon atoms towards the surface.<sup>[169]</sup> For the cleaning of Au(111) crystals, the substrate used for all experiments of this thesis, three to five cycles of repeated sputtering at 2 keV and annealing at  $T = 650\text{ }^{\circ}\text{C}$  were usually sufficient, depending on the degree of contamination. In the second to last cycle the annealing temperature was increased slightly to create a depletion

zone in the bulk and in the last step, ion energies were reduced to 1 keV. A shorter annealing time of the final annealing step then results in a clean, contaminant free Au(111) surface structure.

### 4.4.2 The Au(111) surface

All experiments in this work were carried out using standard gold single crystals. Such metal single crystals are industrially grown and then cut precisely with respect to the crystallographic axis. It is thereby possible to create surfaces, which show a distinct atomic configuration. Frequently used are flat (111) surfaces, presenting a triangular lattice of surface atoms, but also vicinal surfaces can be achieved by slightly mismatching the cutting angle with the crystallographic orientations. The resulting surfaces then show highly periodic monoatomic steps at the surface, which can be beneficial for the synthesis of certain nanostructures or used as a template for molecular self-assembly.

For experiments of this work, a Au(111) surface was chosen, since it can easily be cleaned by ion bombardment and subsequent annealing cycles as described above. The resulting surface is atomically flat and therefore perfect for studies of the self-assembly of molecules. Compared to other (111) surfaces, the structure is different in the sense that the surface atoms relax into positions, different from the bulk configuration, when the surface is clean. This so called  $22 \times \sqrt{3}$  reconstruction is a typical feature of the Au(111) surface and is often dubbed herringbone reconstruction because of its unique appearance. It is a direct result of a periodic shift in local packing densities, changing from fcc- to hcp-packing.<sup>[171]</sup> This change in packing density results in a slight buckling of the surface, which is directly visible in STM images.

By cutting the fcc crystal structure in the (111) direction and thereby creating a free surface, bulk symmetry of the crystal lattice is broken. New solutions to the Schrödinger equation, defining the electronic structure of the bulk crystal, arise as the boundary conditions have to be modified. These new solutions do now include additional electronic states, located at the surface of the crystal decaying both into the vacuum and the bulk.<sup>[169,172]</sup> The energy eigenvalues of those so-called Shockley surface states differ from bulk values, which means that they appear as sharp peaks or steps in STS spectra.

In Figure 4.4 two STM images of a clean Au(111) reconstructed surface are presented together with the respective topographic linescans across the marked lines. The large scale STM image in **a** shows the clean terraces covered with the characteristic herringbone pattern and three distinct monoatomic step edges running from top to bottom of the image. Since this data represents the z-position of the tip during the measurement, one can plot the relative tip position against the distance across the marked red line to get a topographic line profile. This profile is shown below **a** and clearly shows the three distinct steps with a average height of 205.1 pm, which is in good agreement to other experimental results for monoatomic Au steps.<sup>[173]</sup> The herringbone pattern

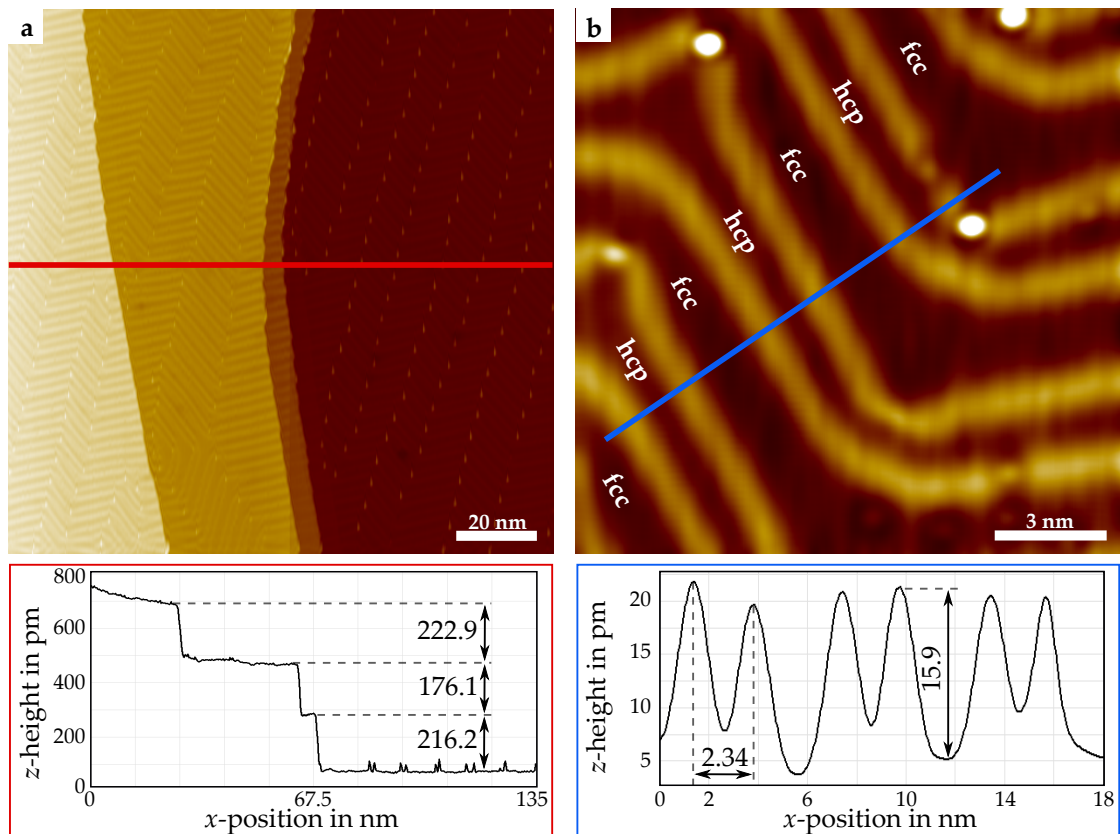


Figure 4.4: **a)** Large scale STM image of the herringbone reconstruction of a Au(111) surface. ( $V_B = +0.6$  V,  $I_T = 50$  pA) **b)** Zoomed in image of the herringbone reconstruction pattern where fcc and hcp regions are marked accordingly. ( $V_B = -1.5$  V,  $I_T = 1.0$  nA) The respective line profiles along the colored lines are given below each image.

stretches across all terraces and always terminates perpendicular to the step edges, because the compressed packing of the discommensuration lines is favorable in that direction.<sup>[174,175]</sup>

In **b)** a zoomed in image of the surface is shown, giving the exact geometry of the reconstruction. The bright lobes sitting in the kinks of the reconstruction are adsorbates like hydrogen and nitrogen, which preferentially stick to the substrate at these adsorption sites. The areas of different packing density are marked accordingly, with the bright discommensuration lines in between, being corrugated in the out of plane direction and therefore appearing brighter. The line profile across the blue line is shown below **b)**, from which one can extract typical geometric values of the herringbone pattern. The corrugation height of 15.9 pm and the distance between the commensuration lines of 2.34 nm are also in good agreement with previously published theoretical and experimental values.<sup>[176,177]</sup> The comparison between the experimental values of these reconstruction characteristics measured with the new LT-STM and other published results is

essential, since the newly installed STM had to be checked for calibration. It also often happens, that thermal drift and piezo creep result in the image not matching the saved scale in the software. If that is the case, the real scale of the image often has to be recovered from such characteristic surface geometries.

These measurements show the benchmark substrate configuration for most of the experiments of this work and also give an idea of how good the spatial resolution really is. The exponential dependency of the tunneling current on the tip sample distance allows for sub pm resolution in the  $z$ -direction, where the apparent height of single atoms or molecules lying on the surface is in a range of a few hundred pm, depending on the interaction with the Au substrate.

Another fact that one has to note here is that the chosen substrate also has an effect of on-surface reactions. In the case of Au(111), it has been shown that the surface lowers dehalogenation energies of adsorbed molecules,<sup>[178,179]</sup> which is often referred to as a catalytic effect in the scientific community.

### 4.4.3 Molecular deposition

All the precursors used in this work were synthesized by collaborators from the University of Nebraska-Lincoln in solution. After purification, the resulting molecular crystals were then sent to us and posed as the starting point for the on-surface synthesis.

For molecular studies on surfaces it is necessary to get the molecules somehow onto the substrate without contaminating it with any other substances. To provide precise control about the amount of deposited material, molecular evaporators are usually used in surface science. These devices are usually Knudsen-cell-type thermal evaporators which provide accurate temperature control and are therefore often used for molecular beam epitaxy, where low partial pressures of the evaporand have to be maintained. The molecular precursors in the form of granular powder are placed inside the crucible which is part of the Knudsen cell and have to be degassed at elevated temperatures below the sublimation temperature before being evaporated. This process reduces the amount of atmospheric contaminants like H<sub>2</sub>O which is still present in the powder. After degassing for several minutes, the evaporator can be used for molecular deposition. To control the amount of deposited material, the system used for this work was equipped with a quartz microbalance. Such microbalances are able to measure sub monolayer coverages by measuring the oscillation frequency of a quartz plate. If material is deposited onto the surface, the eigenfrequency changes slightly and the amount of deposited material can be calculated. Control parameters of the evaporation process like temperature and time were calibrated for each molecular system before the sample was prepared.

Even though this process is used in many laboratories, it does have some disadvantages. Firstly, the molecules have to be thermally stable to stay intact during the heating process, which is especially

problematic for larger molecules. Furthermore, because the diameter of the molecular beam is usually greater than the crystal surface, the whole surface is homogeneously covered, which can be unwanted in some cases. Another downside is that for unknown reasons, the evaporation temperature is not very reproducible in most cases. The filling level of the crucible and the packing density of the powder seem to influence the temperature greatly, meaning that the determined evaporation parameters are not very reliable. Also, to deposit two different precursor species it is necessary to use two separate evaporation cells, which makes it hard to operate both simultaneously with precision to achieve the desired molecular ratio.

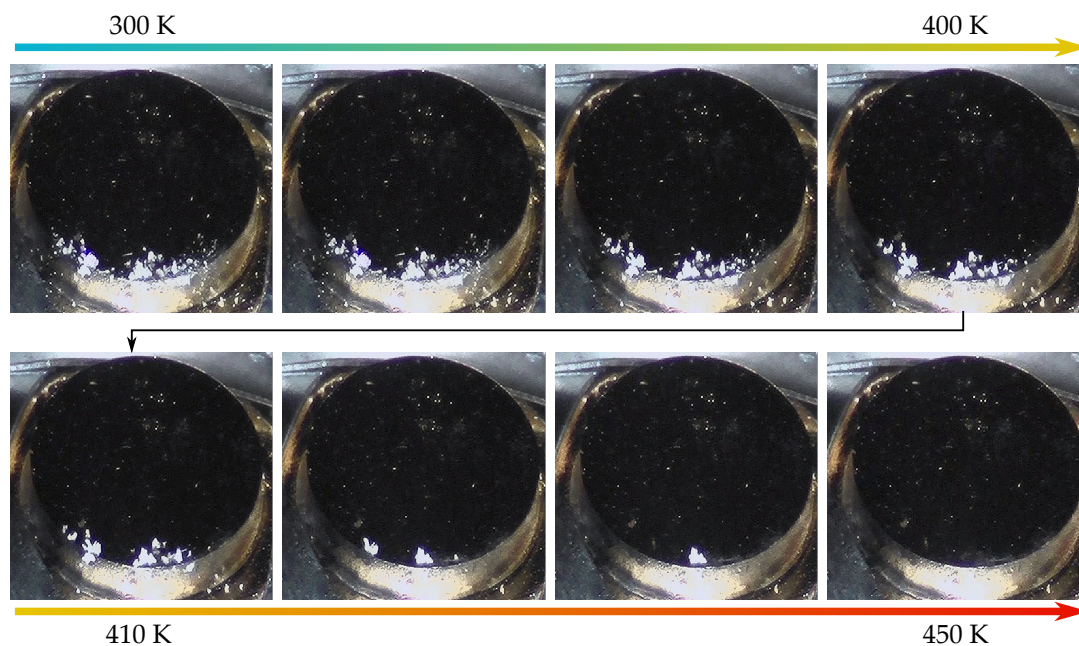


Figure 4.5: Postannealing process after DCT of molecular powder onto a clean Au(111) crystal surface. The powder, seen in white at the bottom of the crystal, starts visibly melting at temperatures above  $T = 400$  K until it is completely vanished.

To circumvent these disadvantages, a deposition process described as direct contact transfer (DCT) was mostly used. A stamp is prepared by using a special contact printing device with a common precision wipe (Kimtech Science) placed at the very front. This stamp is then simply pressed into the molecular powder, prepared by simply crushing the larger crystals with a clean spatula, and is picking up some of it. It is then placed in the transfer arm in the Load lock and, after pumping for several hours to reduce atmospheric contaminants, gently pressed against the edge of the clean crystal surface. Thereby, a large amount of molecules is deposited on the surface, which is then gradually annealed until the molecular powder visibly disappears.

At this point, the crystalline structure of the precursor molecules starts to break apart and diffusive motion of individual precursor molecules sets in. The melting of the precursor powder

is shown in figure 4.5 with photos of the sample surface taken at different temperatures during the postannealing process. The exact melting temperatures of different molecular powders are slightly different, but all lie below  $T = 150\text{ }^{\circ}\text{C}$ . As it is shown the sample does not change visibly while being below  $T = 100\text{ }^{\circ}\text{C}$  but at higher temperatures the small chunks of powder start to vanish first. Larger pieces stay intact longer until finally the thermal energy is enough to overcome the diffusion barrier. In an ideal process like it is shown here, the powder vanishes without leaving any visible residue and the sample surface is covered in precursor molecules afterwards while appearing visibly clean in the camera image. A more detailed view on surface diffusion processes will be given in section 4.7

Even though this process might seem oversimplified, it turned out to be a reliable and easy method for molecular deposition and the used materials for the stamp do not leave any unwanted molecules on the sample.

### 4.5 Organic evaporator

A variety of molecular evaporators for organic molecules are commercially available and ready to use upon arrival. However, since the organic evaporator on the UHV system was not working properly, a new design was developed during the course of this work. This new model was optimized for homogeneous crucible temperature and provides an improved temperature reading.

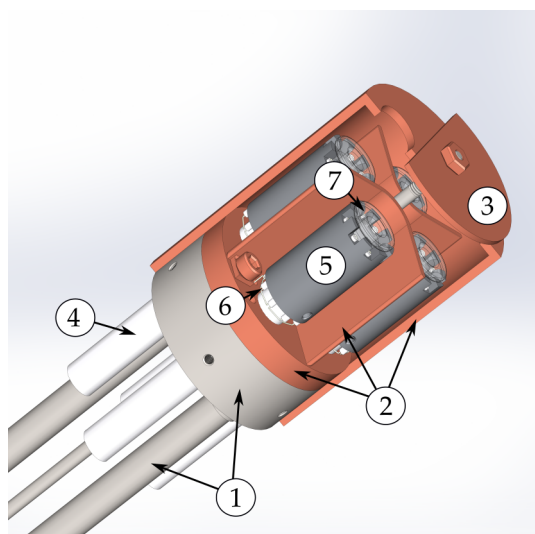


Figure 4.6: CAD model of the evaporator head of the homebuilt molecular evaporator. Important parts are numbered and explained below.

Figure 4.6 shows a CAD model of the evaporator head with the four Knudsen cells mounted inside. The whole assembly is mounted on a variable  $z$  shift on the preparation chamber so that the evaporator head can be moved closer to the sample surface. The whole evaporator is water cooled via an external water bath. The stainless steel cooling lines and body ① are welded onto a CF40 flange, which is mounted on the back of the  $z$ -shift. The two cooling lines are connected through the cooling body and allow for water cooling of the evaporator head and crucibles. Each evaporation cell is surrounded by thermal shields ② made out of oxygen free copper to keep all the metal parts and unused crucibles cool when using just one

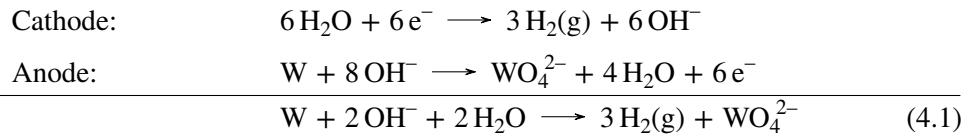
evaporation cell. The outer shield has four holes, each lined up with the crucibles below so that the sublimated molecules can escape. A shutter (3) is mounted on top to cover the openings while the temperature is ramped up. Only when the evaporation temperature is reached, this shutter is opened from outside the chamber for a specific amount of time to guarantee a defined and repeatable deposition time. The Knudsen cells are mounted on top of double bored  $\text{Al}_2\text{O}_3$  tubes (4) to electrically and thermally decouple them from the rest of the assembly. The molybdenum body (5) is equipped with 8 holes, holding again  $\text{Al}_2\text{O}_3$  double bore tubes through which a  $125\ \mu\text{m}$  tantalum wire (6) is threaded. If a current is applied to the wire, the whole molybdenum body is heat up evenly. In the middle of the molybdenum body sits the crucible made from quartz glass (7), under which a thermocouple is mounted to read the temperature of the crucible as accurately as possible.

This design provides several advantages compared to other evaporators. Since the thermocouples are mounted directly underneath each crucible inside the molybdenum body, the temperature reading is repeatable and close to the real temperature of the molecules inside the crucible. Thin filament wires make it possible to reach high temperature with very low current running through the wires, reducing the requirements for the necessary power supply. A tight fit between the crucible and the body provides great thermal coupling and homogeneous heating of the crucible. The biggest advantage however is the rigidity of the whole assembly. Once the evaporation cells are assembled and the filament wire is threaded through the tubes, there are no fragile parts left, and the whole assembly is easy to handle when changing the crucible. With the filament wires being fed through the cooling plates, they can be contacted from below and the chance of damaging them is very low.

## 4.6 Tip preparation

To derive a simple model for the tunneling current in section 2.1, several assumptions were made, one of which is particularly important. All derivations assumed a constant density of states of the tip in the energy interval of interest, which is only true for fully metallic and sharp metal tips. In a real scenario however, the tip will almost always be modified by molecules and atoms which were picked up from the surface and the exact shape of the apex will generally be unknown. Luckily, there are several ways to prepare the tip in-situ to end up with the desired tip configuration. In the following, a short introduction into the methods of tip preparation will be given and it will be explained how different methods can affect the tip apex. The tips are initially etched from a tungsten wire with a diameter of  $380\ \mu\text{m}$  and a purity of 99.9% purchased from GoodFellow. The etching itself is done with a custom-made device by introducing the tip wire vertically into a lamella of NaOH solution. If a voltage is then applied between the tip wire (Anode) and the

counter electrode (Cathode), a chemical reaction (shown in equation (4.1)) leads to the removal of tungsten and, if the right parameters are set, the formation of a sharp apex.



After the etching process, the tip is cleaned by rinsing it thoroughly with H<sub>2</sub>O and ethanol to remove any organic contaminants and residue of the etching process. Afterwards it is checked with scanning electron microscopy (SEM), if the tip radius is in the desired range of a few nanometers. A exemplary SEM image is shown in figure 4.7, where the tip has a perfectly concave shape. The tip apex needs to be evenly formed and can not be too long, since this would result in instabilities and possible vibrations during measurements. The zoomed in image shows the tip apex with a radius of about 7 nm, but covered in a thick layer of hydrocarbon contaminants. Such layers, as well as the naturally formed oxide layer on the tungsten itself, need to be removed by in-situ tip cleaning procedures in the UHV system.

If the shape of the Apex is satisfactorily symmetric and well, the tip is introduced into the Load-lock of the system. A first annealing process at temperatures between 100 °C and 100 °C for a couple of minutes removes most of the volatile hydrocarbons and atmospheric residue from the transfer process. Typically, the tungsten is oxidized and this oxide layer needs to be removed first before it is usable as a STM tip. This is done by contacting the tip wire with a direct current heating tool, which feeds 8-10 A through the tungsten wire and thereby increases the temperature to about 1000 °C. At such high temperatures, the oxide layer of W<sub>2</sub>O<sub>3</sub> reduces to WO<sub>2</sub>,<sup>[116,180]</sup> which itself is volatile and therefore leaves a tip of pure, unoxidized tungsten. Only in this form does the tip provide sufficient conductivity, stability and most important a purely metallic, and thereby mainly constant, density of states. When annealing the tip one has to be careful not to overheat it, too high temperatures can lead to blunting of the tip apex.<sup>[181]</sup>

The first measurements with such a freshly prepared tip are often far from optimal, since the high electrical field strengths between the apex and the sample surface can often lead to instabilities during measurements. To stabilize the tip, one usually has to condition it on a clean Au(111) substrate by using a variety of different methods. For example, if the images appear to be very streaky, there are often loosely bound molecules or atoms attached to the tip, which can be removed by applying voltage pulses between -10 V and +10 V. However, if the amplitude of the voltage pulse is chosen too large, the tip can be damaged permanently or even 'explode', meaning that the apex gets detached after which the tip is blunt and undefined.

Another method to condition the tip in situ is to dip the tip slightly into a clean part of the

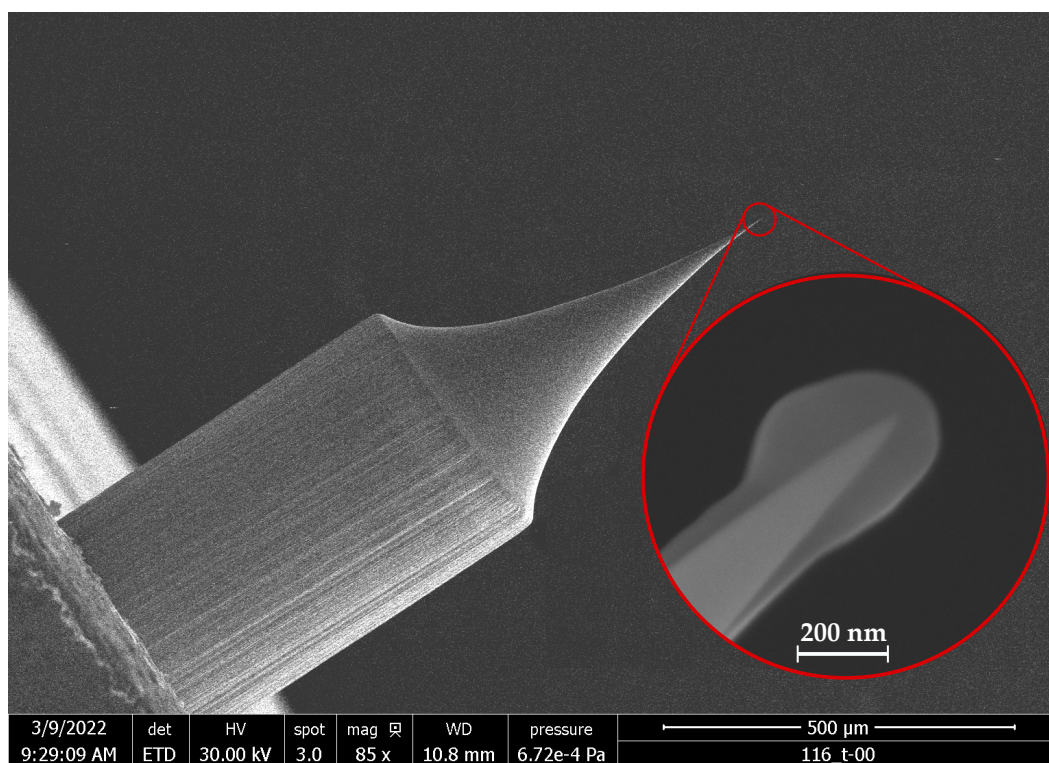


Figure 4.7: SEM image of a etched tungsten tip. In the red circle a zoomed in image of the tip apex is shown.

substrate to mechanically form the apex. To do this, the tip is moved in the  $z$  direction closer to the substrate until ohmic contact is measured. Then the tip is gradually pulled out of this contact while a negative bias voltage is applied. It is thereby possible to coat the tip with a layer of Au atoms from the surface, that form a new, sharp Apex. Mechanical grinding of the tip can be done by reducing the size of the scan frame to only a few  $\text{nm}^2$  while bringing the tip really close towards the surface. If the scan speed is then set to several  $\mu\text{m s}^{-1}$ , it will heavily affect the tips surface atoms and lead to a permanent deformation of the apex.

It should be noted here that all these methods should be carried out on a clean Au substrate. If there are other molecules present on the surface, the chance is high that those get picked up by the tip which would then again lead to a modified density of states. In figure 4.8 three exemplary STM images are shown, which show the sample surface after applying different tip preparation techniques. In **a**, the tip was dipped into the surface unintentionally and resulted in a hole being pressed into the fully covered Au surface. The STM image in figure 4.8 **b** shows single GNR heterostructures on the surface together with five large chunks of 'dirt', marked by the red circles. These piles are the result of voltage pulses, resulting in Au islands being tossed from the tip onto

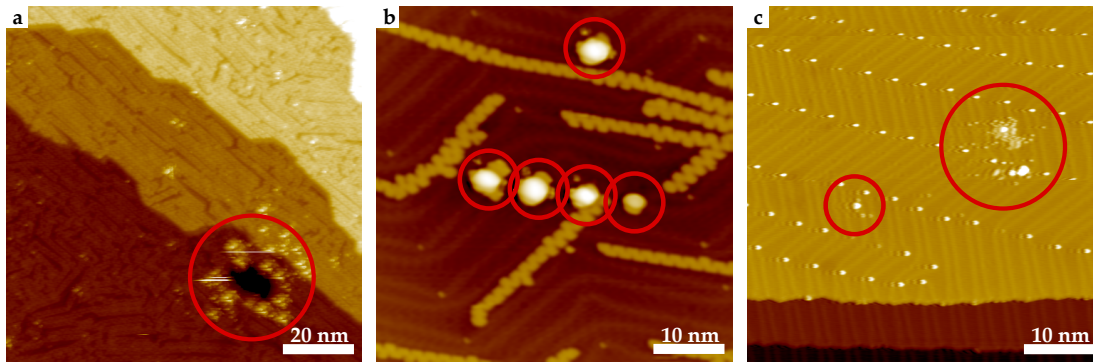


Figure 4.8: **a)** STM image of a sample after the tip apex crashed into the surface and left a large hole. ( $V_B = +1.0$  V,  $I_T = 0.5$  nA) **b)**  $I$ - $V$  measurements resulted in the deposition of Au islands on the sample surface. ( $V_B = +0.8$  V,  $I_T = 1.0$  nA) **c)** Random deposition of tip adsorbates on clean Au(111) during scanning. ( $V_B = +0.6$  V,  $I_T = 10.0$  nA)

the sample surface. By applying negative voltage pulses it also happens that surface atoms are pulled out of the lattice, forming similar bright lobes on the surface. In **c** the tip was scanning over a clean substrate area multiple times when it started to spontaneously lose adsorbates onto the surface. This can also happen when the tip configuration is unstable after frequent tip changes occurred. These images show that the sample surface can be severely modified by the tip and the method of preparation should be chosen carefully.

For  $dI/dV$  measurements, it is extremely important that the density of states of the tip is constant, meaning it has a defined and sharp apex. For this purpose,  $dI/dV$  spectra are frequently acquired during the scanning process. If the spectra show any sign of deviation from the prototypical measurements, the tip configuration must have changed, and must be restored by the methods described above. Only when the spectra repeatedly reproduce pristine Au(111) spectra, a measurement of other structures on the surface should be considered. This process of preparing the tip for  $dI/dV$  measurements can consume several days, depending on how good the tip initially was. However if a solid, clean tip configuration is reached, it is usually stable over long periods of time.

## 4.7 Surface diffusion and self-assembly

Most of the samples investigated in this work were prepared by using a direct contact transfer process described in section 4.4.3. The brief description given there summarizes the necessary steps to use this method, but does not go into detail about the actual physical processes behind the diffusion. For this reason, a short introduction will be given how diffusion processes on metal single crystal surfaces work, and how they can be exploited to produce samples with gradually increasing surface coverage across the crystal surface.

### 4.7.1 Diffusion processes on metal surfaces

Self-assembly of nanostructures on surfaces is different from solution-based self-assembly in two ways. One, it is a solvent-free approach, and two, the surface provides a landscape of diffusion barriers which can guide or inhibit the surface diffusion of adsorbed molecules. It has to be noted here that a variety of different diffusion barriers across flat surfaces, step edges and defects exist on a Au(111) surface. For simplicity, only a diffusion process across a flat surface in one crystallographic direction will be discussed here.

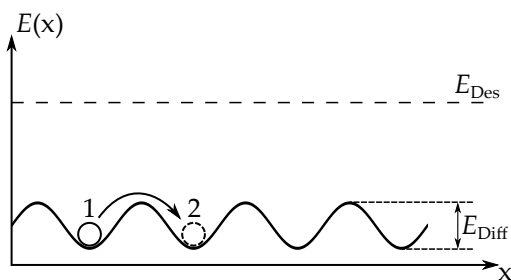


Figure 4.9: Schematic visualization of the surface diffusion process.

Figure 4.9 schematically shows the energy landscape for a single molecule, represented by a circle, adsorbed on a single crystal surface. The periodicity of the energy landscape is given by the surface atoms of the Au crystal. To get from one adsorption site on the surface to another, molecules have to overcome the diffusion energy  $E_{\text{Diff}}$ . This energy strongly depends on the substrate material and the interaction of adsorbates and surface atoms. At

sufficiently low temperatures, each molecule is adsorbed at a specific site without having enough energy to hop from one adsorption site to another. In this case  $E_{\text{Diff}} \ll k_B T$ , meaning that, without thermal activation, the sample will simply stay in this configuration. By increasing the temperature it is possible to overcome that potential energy barrier and the molecules will start to randomly hop from site to site, i.e. 1 to 2 in figure 4.9, described by a random walk motion. On a two-dimensional crystal surface, this of course means that the random walk motion happens in two directions. Increasing the temperature even further until  $k_B T \approx E_{\text{Des}}$ , will result in molecules desorbing from the surface into the vacuum or, if the binding energies inside the molecular adsorbates, cause molecular fragmentation. It is therefore easy to see why additional annealing helps to reduce the amount of unwanted weakly bound contaminants. Such species

or fragments that diffuse freely over the sample surface usually have low desorption energies. Increasing the sample temperature carefully will therefore lead to a desorption of all the mobile species, while the desired molecules stay adsorbed at the surface.

Looking at the case where molecules are deposited on the surface via evaporation and the surface coverage is low, meaning that every molecule is surrounded by empty adsorption sites, one can model the mean square displacement  $\langle r \rangle^2$  of a single molecule on a 2D surface via

$$\langle r \rangle^2 = \nu a^2 t$$

where  $a$  is the distance to the neighboring adsorption site,  $t$  is the time and  $\nu$  is the hopping frequency which can be written as

$$\nu = \nu_0 \exp\left(\frac{-E_{\text{Diff}}}{k_B T}\right).$$

The diffusion coefficient  $D$  then follows as

$$D = \frac{\nu a^2}{z}$$

where  $z$  is the number of neighboring sites. For the experiments described in this work it is difficult to estimate the hopping frequency  $\nu$  as well as the actual time  $t$  where diffusive motion happens on the surface since annealing involves a continuous increase in temperature and the diffusion energy  $E_{\text{Diff}}$  is generally unknown. The probability of a hopping event to happen is thus dependent on the energy of the adsorbate and the time. This means that hopping can occur even at low temperatures if enough time is given. In order to determine the diffusion constants, one would have to study surface diffusion very extensively. This is, however, beyond the scope of this work.

As described before, the experiments of this work were mostly carried out using the DCT process for molecular deposition. With this method, large amounts of molecules are deposited locally on the surface. A postannealing step then leads to the dispersion of molecules all over the surface. In this case, the diffusive motion can not be considered as individual diffusion of single molecules, but has to be described within the scope of continuum mechanics. In the 19th century, the phenomenon of diffusion of continuous media was first described by Adolf Fick, who formulated his famous first and second law of diffusion.<sup>[182]</sup> In the case of this work, the large number of molecules on one side of the crystal creates a concentration gradient  $\nabla c$  across the surface, which is responsible for a driven, diffusive motion of molecules towards the area with lower concentration. Fick's first law of diffusion assures a direct proportionality between the

diffusion flux  $J$  and the concentration gradient  $\nabla c$  as

$$\vec{J} = -D\nabla\vec{c}, \quad (4.2)$$

with the diffusion coefficient  $D$  as a proportionality factor, and the negative sign indicating the flux towards the area with lower concentration. Here  $D$  and  $\nabla c$  are assumed to be constant, which is usually not the case in real systems. By combining equation (4.2) with the continuity equation

$$\frac{\partial\vec{c}}{\partial t} = -\nabla\vec{J},$$

one gets Fick's second law of diffusion.

$$\frac{\partial\vec{c}}{\partial t} = D\nabla^2\vec{c} \quad (4.3)$$

assuming that  $D$  is constant and isotropic. Applying this to the case of DCT, namely a semi-infinite reservoir deposited on one side of the crystal with the boundary being located at  $x_0$  one can find a solution by using the complementary error function  $\text{erfc}(x)$  with the following boundary conditions.

$$\begin{aligned} c(x, 0) &= c_0 & \text{for } x < x_0 \\ c(x, 0) &= 0 & \text{for } x \geq x_0 \end{aligned}$$

$$c(x, t) = c_0 \text{erfc}\left(\frac{x - x_0}{2\sqrt{Dt}}\right)$$

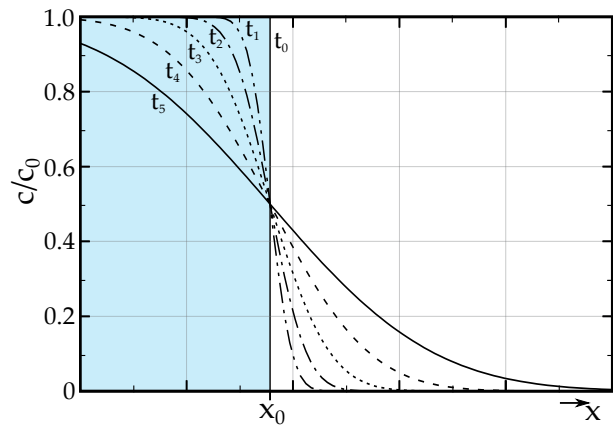


Figure 4.10: Errorfunction plotted for different values of  $t$ . Marked in blue is the area where the initial concentration is  $c_0$ .

Figure 4.10 illustrates this solution for different values of the time  $t$ , where it can be seen that the initial sharp concentration gradient flattens out. The time  $t$  in this case refers to the overall annealing time in which the thermal energy is higher than the diffusion barrier. This is of course a very simple model that does not take into account that different diffusion barriers, and therefore diffusion constants, do exist on a crystal surface. Fundamental diffusion processes like diffusion over terraces, steps or along corners all have different diffusion barriers.<sup>[183]</sup> In the case shown

here, the diffusion constant would then be a kind of average diffusion constant that describes the composition of all different processes in one parameter. However, even if this model is simple, it reproduces the experimental data sufficiently well.

#### 4.7.2 Diffusion based sample preparation

In the course of this work, it was found that it is possible to exploit those diffusion characteristics for the preparation of inhomogeneously covered samples. The DCT method makes it possible to create a reservoir of molecules on one side of the crystal surface while leaving the rest of it clean. Promoting diffusive motion of the molecules through thermal annealing then creates a coverage gradient over the sample surface similar to figure 4.10. In addition, the differences in diffusion kinetics of two different precursor molecules can be used to create GNR heterojunctions by simply depositing two molecular species with the DCT approach.

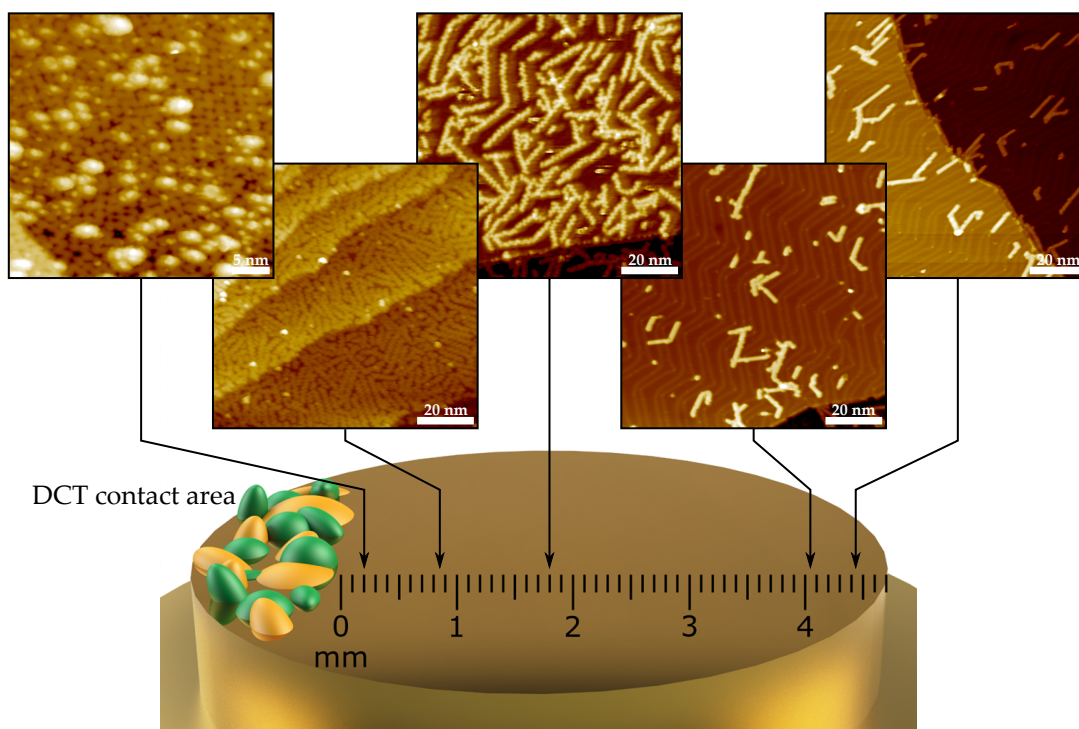


Figure 4.11: STM images measured at different positions on the Au(111)-surface. All images measured with  $I_T = 100 \text{ pA}$  and  $V_B = -2.0 \text{ V}$

The STM makes it possible to study two different characteristics of samples prepared this way. One, the overall surface coverage as a function of the distance from the stamping site, and two, the molecular composition of heterojunctions across the coverage gradient. This section will only focus the surface coverage as a function of distance and the different heterojunctions will be

discussed separately in section 5.3.1.

By simply using the coarse motion of the STM, the tip can be moved across the crystal surface and STM images can be acquired at different distances from the stamping site. In figure 4.11, five STM images are presented, clearly showing different surface coverages. The stamp was in this case prepared with a 1:1 molar mixture of two molecular precursors for GNRs. The molecules are represented by the green and orange pieces on the left side of the crystal surface. The annealing process involved a first step where the temperature was slowly increased until the visible molecular crystals vanished to promote precursor diffusion and then a rather quick temperature ramp until the final temperature of  $T = 450\text{ }^\circ\text{C}$  was reached to form the final GNRs present in the STM images. These images were then used to extract the surface coverage of GNRs without distinguishing between the two types of precursor molecules. The coverage in monolayers is plotted against the distance from the stamping site in figure 4.12.

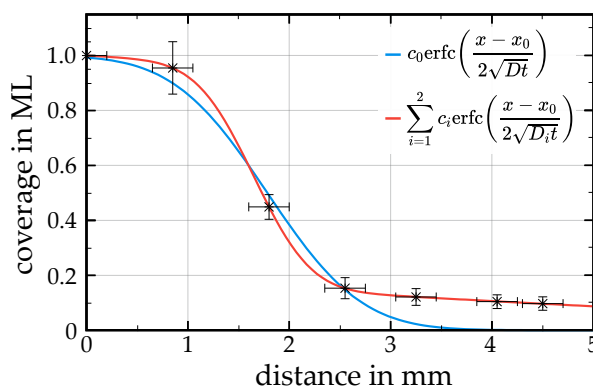


Figure 4.12: Plotted values of surface coverages in different distances from the DCT contact area. In blue the model for diffusion of one molecular species is shown and in red a second species was added to represent the data.

Since the quality of the STM images varies strongly, the coverage can be locally modified by step edges or surface defects and an exact determination of the distances is hardly possible the error bars are rather large on some of these datapoints. Nevertheless, an obvious deviation from the diffusion model of just one molecular species is visible. Especially the fact that the coverage does not come down to zero within the dimensions of the crystal surface but rather shows a constant decay until reaching the opposing edge can just be reproduced by using a diffusion model including two independent diffusion processes. The blue curve represents a model for the surface coverage if just one precursor species is deposited onto the crystal surface, while the red curve includes two species with different diffusion kinetics.

Since the model is only used to reproduce the overall distribution of the data points, no fit to the data was performed. However, in order to get the best approximation possible, it was assumed that the edge position  $x_0$  and the annealing time  $t$  are equal in both terms of model 2 (red). The individual concentrations  $c_i$  also needed to be constraint. It was set that

$$c_1 + c_2 = 1 \quad \text{for} \quad x = x_0,$$

since the observed surface coverage right at the stamping site was 1.0 ML, and the molar ratio of the precursors should ideally be 1:1, meaning that

$$c_1 = c_2 = 0.5 \quad \text{for} \quad x = x_0.$$

The last condition however represents an idealized case because the weighed quantity of molecules did hardly exceed 1 mg and the molar masses of the precursors molecules are highly different. It was therefore not used as a constraint when approximating this model, since a large error when weighing in the molecules has to be assumed. Another point that should be addressed here is the uneven spacing and lack of datapoints on the distance scale. As the measurements were performed, the crystal surface was significantly contaminated by dust particles from the frequent use in other experiments. Such contaminations are also visible in figure 4.5. They could have potentially altered the surface coverage locally, which is why attention was paid to always chose measurement locations on clean parts of the surface. The only datapoints included in this evaluation were taken from images of such locations.

## 5 Experimental results

The following chapter includes the most significant experimental results within the scope of this work. First, the growth of structurally similar precursor molecules on Au(111) was studied. It was found that, even slight changes in the precursor structure will result in significant differences of the resulting GNRs structure. The structure of the synthesized GNRs ranged from simple straight AGNRs and chevron GNRs to ribbons with a notched edge structure and even porous GNRs. Differences between solution based and on-surface synthesis approaches were also investigated, revealing distinctly different molecular structures.

A new synthesis route, for the formation of GNR heterojunctions has already been presented in section 4.7.2. The results of these experiments will be reviewed, showing how a theoretically predicted topological state at the interface of one junction could be experimentally confirmed by  $dI/dV$  mapping. In the last part of this chapter, it will be shown how it is possible to create porous nanographenes out of individual GNRs.

By using an additional postannealing step, it was possible to fuse parallelly aligned GNRs with different structures. The formed PNGs were investigated spectroscopically, revealing exceptional electronic properties of these nanostructures.

All the STM data shown was acquired with the use of the LT-STM described in section 4.2. Both cryostats have been filled with liquid nitrogen, resulting in a sample temperature of  $T = 77$  K. The exact measurement parameters for each image or spectrum will be stated in the caption of the respective figure.

## 5.1 Graphene nanoribbons

Since on-surface synthesis of GNRs is a well established method for more than 10 years now, a variety of structurally different ribbons have already been synthesized. Through structural design of the precursor molecules it is possible to synthesize GNRs with different edge structures, widths and specific structural features as desired. By synthesizing the precursor molecules in solution, using different reaction routes and procedures, it is possible to tailor their structure, and thereby create very specific GNR structures.

For example, Rizzo et al. used asymmetric precursor molecules that has been designed specifically for the purpose of synthesizing periodic 7-/9-AGNR heterostructures.<sup>[143]</sup> These hetero-GNRs were theoretically predicted to develop topologically induced bands inside the usual bandgap of the structure. Through the specific design of the precursor molecule they were able to verify these predicted bands experimentally. This shows, that tailored precursor molecules make it possible to create nanostructures with highly specific electronic properties.

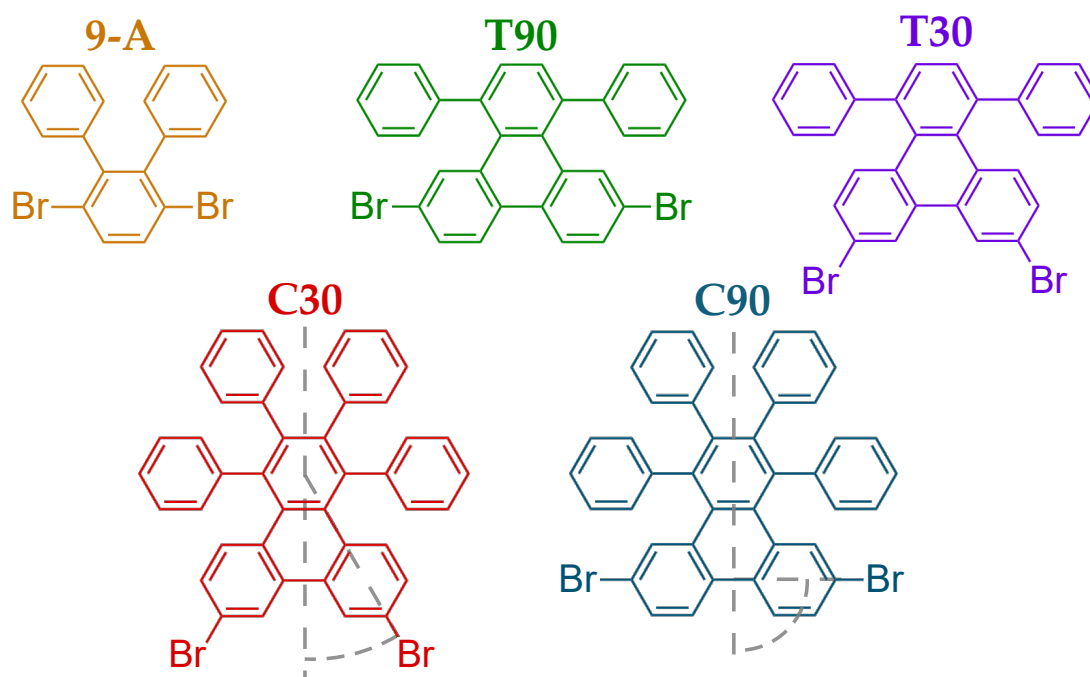


Figure 5.1: Structure formulas of the different precursor molecules used for GNR synthesis.

Based on the two well established precursor molecules 9-A and C90, which have been used in several research works in the past,<sup>[26,102,133,184]</sup> three novel precursors have been developed specifically for the experiments of this thesis. In close collaboration with the group of Professor Sinitskii from the University of Nebraska-Lincoln, these molecules were designed based on the structure of the C90-molecule. Each of them giving rise to specific structural enhancements, that

are expected to alter the resulting GNRs properties significantly.

For the rest of this work, the respective molecules will be referred to with their names given above the structures shown in figure 5.1. Depending on which state they are in during the reaction, these abbreviations will be combined with the appendix -precursor, -polymer, -GNR or -PNG. The acronyms were introduced with reference to the structure of the molecule, where C stands for Chevron, the common notation of the GNRs formed from C90-precursors in literature and T for truncated, meaning that two phenyl rings at the head side of the molecule are missing. 30 and 90 refers to the halogenation angle that is formed by the symmetry axis of the molecule and the C-Br-bond, as shown in figure 5.1. The name of the 9-A-precursor has been adapted from the notation in other research works. The IUPAC names of the individual molecules are given in section 7.2.

Especially the varied halogenation angle on C30- and T30-precursors is expected to result in interesting structures. This is the first time that such symmetric molecules are used with halogenation angles of 30°. For T30-precursors, a 9 carbon atom wide GNR with armchair edges is expected to form. However, this armchair edge configuration will be periodically modified by 'defects' or notches, that will change the electronic properties of the ribbons.

Using precursor designs that are structurally familiar will enable to compare the STS results to already published data for pristine GNRs.

### 5.1.1 C90-GNRs

C90-GNR, are in other research works often called chevron GNRs, because of their distinct shape and were part of the first scientific study of on-surface bottom-up GNR synthesis by Cai et al. in 2010.<sup>[26]</sup> In many following studies C90-GNRs were synthesized on surfaces and in solution,<sup>[126,185,186]</sup> doped with nitrogen heteroatoms,<sup>[96,187]</sup> or structurally modified<sup>[133,136,154,188]</sup> to gain insight into their physical and electronic properties. All these studies demonstrated the versatility of these ribbons and showed that the bandgap of chevron like GNRs is very different from straight armchair or zig-zag GNRs.<sup>[133,189]</sup> The bandgap of C90-GNRs on Au(111) was experimentally determined to be between 1.6 eV and 2.8 eV,<sup>[125,126]</sup> being significantly larger than the bandgap of AGNRs of similar width.<sup>[119]</sup>

The experiments with C90-precursor molecules were started as a first test of the newly set up LT-STM. The final goal was to prepare heterojunctions out of C90-GNRs and 9-AGNRs, for which it is inevitable to have precise knowledge about the synthesis parameters of each individual system. Since most of the other on-surface synthesis works have used thermal evaporation as a deposition method also chose to deposit the precursor molecules with the new evaporator shown in figure 4.6. This process involved the determination of evaporation temperatures of the molecules, trying different evaporation times and comparing them to the resulting surface coverage, and also testing different annealing temperatures for the polymerization and cyclodehydrogenation of the precursor molecules. These temperatures are very well documented in other works, however since temperature readings can vary extremely for different setups it is necessary to test and in case adjust the parameters for the particular system used.

In principle, the on-surface synthesis of graphene nanoribbons always follows the steps shown in figure 3.2. However, to make it clear which covalent bonds are formed in the individual reaction steps, the respective reaction pathway for all molecules studied will be given. For C90-GNRs, the reaction path is shown in figure 5.2 **a**. Newly formed bonds in each step are colored in orange. The molecular precursors are deposited onto the surface and a first annealing step (**I**) at a temperature of  $T \approx 180^\circ\text{C}$  initiated polymerization by removing the halogen Br. The temperature was therefore increased over the course of 30 min to enable sufficient diffusion, leading to the formation of long polymer chains. The sample was then usually checked with STM to investigate the reaction products. The second annealing step (**II**) at a temperature of  $T \approx 480^\circ\text{C}$  led to cyclodehydrogenation, resulting in planar C90-GNRs on the surface.

Figure 5.2 **b** shows an STM image of C90-GNRs on a reconstructed Au(111) surface. To prepare a sample with such low coverage for the investigation of individual ribbons, an evaporation time of  $t = 2$  min at a measured crucible temperature of  $T = 140^\circ\text{C}$  was used. The characteristic chevron like shape of the GNRs is clearly visible and matches the expected chemical structure perfectly. With the low surface coverage present in this image, the herringbone reconstruction of

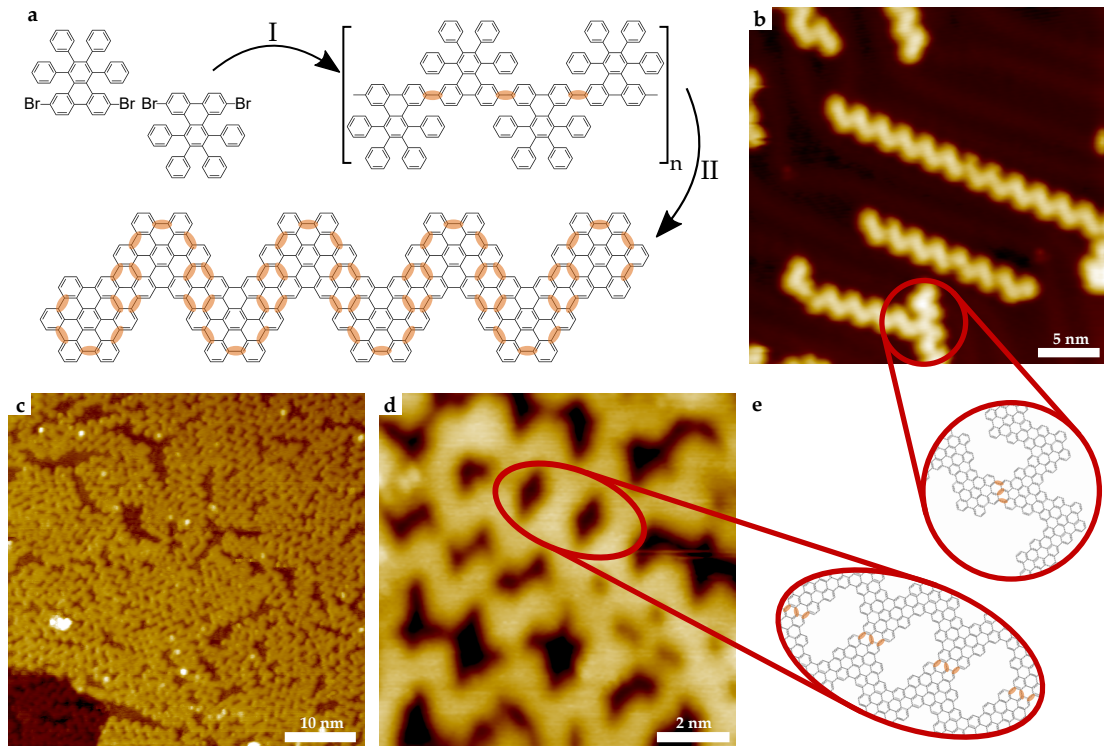


Figure 5.2: **a)** On-surface synthesis route for the formation of C90-GNRs. Newly formed covalent bonds are highlighted in orange. **b)** Fully cyclized chevron GNRs on Au(111) with low surface coverage. ( $V_B = +0.8$  V,  $I_T = 0.1$  nA) **c)** Highly covered surface area. ( $V_B = +1.8$  V,  $I_T = 0.1$  nA) **d)** Zoomed in image of a fused GNR structure creating diamond shaped pores. ( $V_B = +1.2$  V,  $I_T = 0.05$  nA) **e)** Structure formula highlighting the formation of interribbon bonds.

the Au surface is still slightly visible in the background. From the orientations of the ribbons, one sees that they are aligned nicely with this pattern. This means that in areas with low surface coverage, the corrugation of the substrate guides the chain growth. Individual precursor molecules diffuse inside the fcc channels of the reconstruction, defining the growth direction of the ribbons.

In figure 5.2 **c** no such template effect is visible. The high surface coverage forces the ribbons into a densely packed configuration, where intermolecular interactions overcome the diffusion barriers given by the herringbone pattern of the surface. It is also obvious that the average ribbon length is much smaller than in **b**. This also is a direct result of the high surface coverage, since during polymer formation the individual formed chains interact with each other, hindering the attachment of new precursor molecules. These images were taken on a different sample, prepared by evaporating C90-precursors for  $t = 20$  min at a crucible temperature of  $T = 140$  °C onto the surface.

The STM images in figure 5.2 **c** and **d** both show fully cyclized C90-GNRs with a surface

coverage of close to one monolayer (ML). Looking closely one has to realize that in some locations, where the distance between chains is particularly small, covalent bonds have formed between adjacent GNRs. This directly shows that the temperature during the cyclodehydrogenation step was chosen a too high. As it will be in section 5.4, the hydrogen atoms located at different sites of an individual precursor molecule do not have identical binding energies. This means that hydrogens at the head sites of the precursors in the polymer chain are usually not cleaved during the cyclodehydrogenation process because their binding energy is higher. However if neighboring chains come in close contact with each other, these the hydrogen atoms at the head sites have to relocate because of steric hindrance, straining the covalent bonds and eventually leading to the breaking of these bonds at lower temperatures.

In the case of this particular sample, the second reaction temperature was chosen slightly higher than usual, to guarantee a complete cyclization of the GNRs. This however also resulted in the formation of interribbon bonds as can be seen in **c** and **d**. Figure 5.2 **e** shows two structural models of exemplary structures present in the STM images. The upper one resembling branching due to the merging of the end of one ribbon and the edge of another one. Here the template effect of the substrate resulted in a connection angle of  $60^\circ$  because the individual polymers were oriented along the herringbone reconstruction. The detailed image in **d** shows two short GNR segments which are parallelly aligned and fused at their edges. The unique shape of the chevron GNR leads the formation of diamond shaped pores, which are also shown in the structural formula in **e**. Even though these pores are rather large, these findings resulted in the idea for the synthesis of a porous nanographenes out of individual GNRs. This idea was then further developed and led to the findings presented in section 5.4.

Since GNRs are so popular because of their semiconducting properties, it is necessary to further characterize the synthesized structures via STS. Using  $dI/dV$  point spectroscopy, the electronic properties of individual C90-GNRs shall be determined from experimental data in the following.

Figure 5.3 presents the taken  $dI/dV$  point spectroscopy measurements together with a select C90-GNR. Two spectra are shown in **a**, acquired at different positions in the sample as marked in **b**. In figure 5.3 **b** an STM image of a pristine C90-GNR segment is shown. The superimposed structural model reveals that the GNR is defect free and the length is sufficient to neglect any effects of end terminations on the electronic structure. The blue and gray cross exemplarily mark the locations on which measurements were taken.

The Au(111) spectrum in **a** is a great example for a  $dI/dV$  point spectrum taken at a clean substrate area. The spectrum appears mainly featureless except of the step-like surface state peak located at  $E = -0.48$  eV, which is a direct result of the dispersion relation of the Shockley surface state.<sup>[190]</sup> The asymmetry of the spectrum has already been described in **STS**, showing a higher signal amplitude at negative bias voltages.

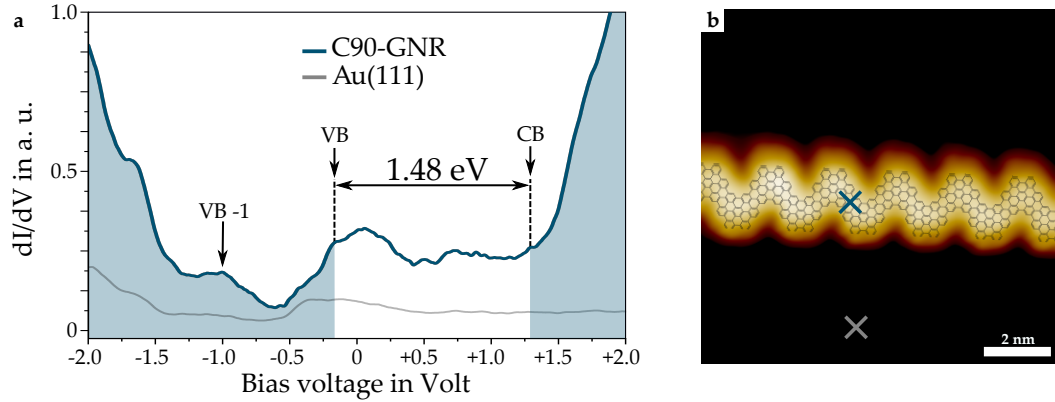


Figure 5.3: **a)**  $dI/dV$  point spectra of C90-GNR (blue) and Au(111) surface (gray). ( $I_T = 0.3$  nA,  $V_{\text{mod}} = 20$  mV,  $f_{\text{mod}} = 964$  Hertz) **b)** Detailed STM image of a C90-GNR with a superimposed structural model. Measurement locations of the point spectra are marked accordingly. ( $V_B = -1.2$  V,  $I_T = 1.0$  nA)

The blue spectrum in figure 5.3 **a** resembles the electronic structure of individual C90-GNRs. However, before discussing the features of this spectrum in detail, some experimental aspects of the measurement itself have to be pointed out. Each spectrum is an average over multiple measurements, which were not necessarily taken in the exact same GNR but on similar locations all over the sample. It is necessary to gather lots of data in different locations to be able to decide which spectra might include tip artifacts and which features correspond to real electronic states of the GNR. One also has to keep in mind that the measurement represents the electronic configuration of a C90-GNR supported by a Au(111) substrate. It should therefore only be compared to other experimental results using the same substrate to rule out any confusion because of GNR-surface interactions that could electronically modify the ribbons.

The blue curve in **a** resembles a typical GNR spectrum. Measured in a range of  $-2$  V to  $+2$  V, it shows the distinct increased signal at high positive and negative energies due to the valence and conduction band. In between, the spectrum is more flat, with only a few features visible as distinct peaks. The analysis of such spectra is not straight forward and the determination of the location of VB-1, VB and CB are done differently by many research groups. The evaluation of  $dI/dV$  point spectra in this thesis will follow the procedure used by Merino-Díez et al.,<sup>[119]</sup> who explicitly determined the feature near the Fermi energy to be the real VB edge. They demonstrated that this peak is indeed a result of the GNR being placed on the Au(111) substrate and has to be therefore seen as an electronic state of the GNR.

The blue spectrum shows the individual electronic states of a C90-GNR measured directly above the GNRs backbone. Immediately obvious is the presence of both VB-1 and CB edge at  $E = -(1.00 \pm 0.15)$  eV and  $E = +(1.28 \pm 0.08)$  eV, visible by the increased signal amplitude at these energies. The VB edge is here located at  $E = -(0.20 \pm 0.05)$  eV which results in a bandgap

width  $E_{\text{Gap}} = (1.48 \pm 0.13) \text{ eV}$  for C90-GNRs. In past research works, people often used the VB-1 edge to calculate the bandgap, which in this case would lead to a bandgap with of  $E_{\text{Gap}} = (2.28 \pm 0.23) \text{ eV}$ , being in good agreement with other experimental results.<sup>[125,126]</sup>

It should be noted here that the electronic structure of graphene nanoribbons varies strongly depending on the exact location of measurement. Localized states at the ribbons edges will modify the bandstructure and result in a different bandgap width compared to a measurement at the ribbon's backbone. Therefore, results of different publications have to be carefully compared with respect to the substrate used and the exact location where the spectrum was recorded.

These results laid the groundwork for the synthesis of C90-GNR/9-AGNR heterojunctions and also proofed that the experimental data obtained with the LT-STM is in good agreement with other results.

### 5.1.2 9-AGNRs

The experiments continued with the on-surface synthesis of 9-AGNRs. Figuring out the synthesis parameters is necessary to guarantee a successful synthesis of C90-GNR/9-AGNR heterojunctions. The first reported synthesis of 9-AGNRs was published by Talirz et al. in 2017,<sup>[191]</sup> using a Au(111) crystal as a substrate. The synthesis of these 9-atom-wide armchair GNRs was driven by the theoretical prediction, that they should exhibit a reduced bandgap. Since they belong to the  $3p$ -symmetry group, their bandgap should be considerably smaller than those of 8- or 10-AGNRs.<sup>[23]</sup> To deposit the 9-A-precursor molecules onto a clean Au(111) surface the home built molecular evaporator was used again. The evaporation parameters were chosen accordingly, with a evaporation time of 90 s at a crucible temperature of  $T = 140\text{ }^\circ\text{C}$ . Figure 5.4 **a** shows

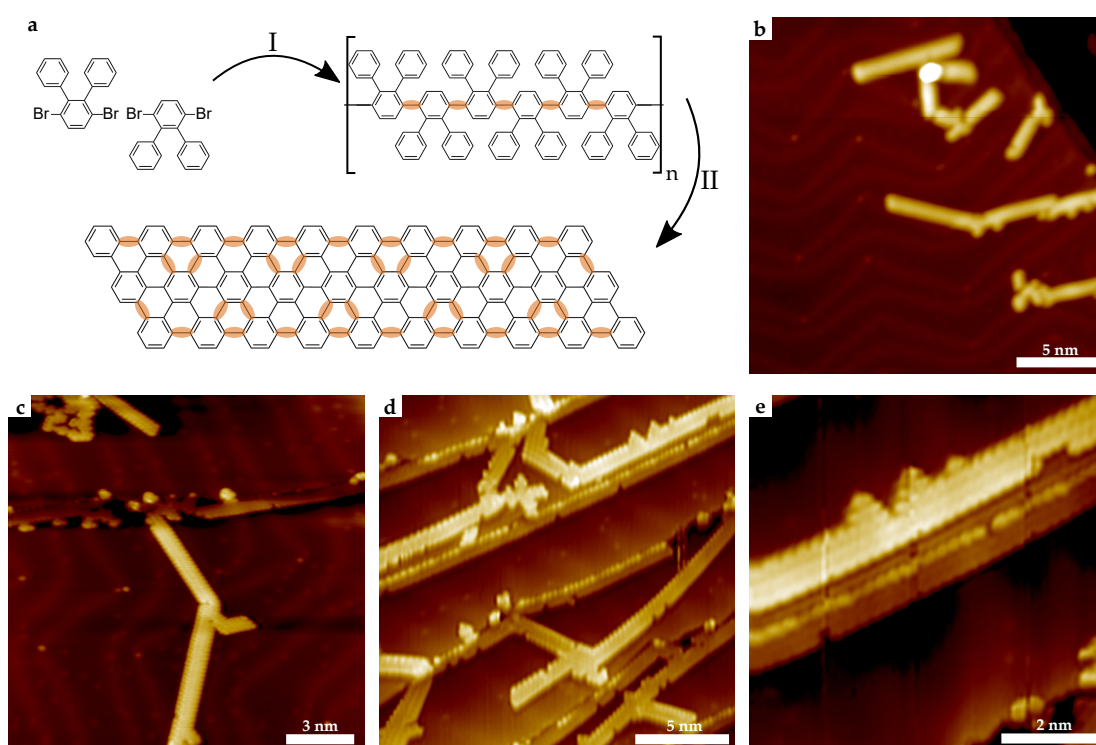


Figure 5.4: **a**) On-surface synthesis route for the formation of 9-AGNRs. Newly formed covalent bonds are highlighted in orange. **b**) STM image of 9-AGNR segments on Au(111) ( $V_B = -1.4\text{ V}$ ,  $I_T = 0.5\text{ nA}$ ) **c**) High resolution image of single 9-AGNRs. ( $V_B = -1.4\text{ V}$ ,  $I_T = 0.5\text{ nA}$ ) **d**) Alignment of 9-AGNRs on surface step edges. ( $V_B = -1.4\text{ V}$ ,  $I_T = 0.3\text{ nA}$ ) **e**) Detailed image of a defective 9-AGNR and step edge alignment. ( $V_B = -1.8\text{ V}$ ,  $I_T = 0.5\text{ nA}$ )

the reaction path for the on-surface synthesis of 9-AGNRs out of its molecular precursor. The formation of polymer chains (**I**) was initiated by a first annealing step at  $T \approx 140\text{ }^\circ\text{C}$ , slightly

lower than the related temperature for the C90-precursor molecules. The formed polymer chains were afterwards cyclized (**II**) by increasing the temperature to  $T \approx 450$  °C for about 20 min and the resulting 9-AGNRs are shown in figure 5.4 **b - d**. Looking at the STM images in **b** and **c**, there are two fundamental differences to recognize compared to the synthesis of C90-GNRs. First, there is no template effect of the substrate visible. Even at low surface coverages, the GNRs do not align with the herringbone reconstruction and therefore show no preferred orientation or a parallel alignment relative to each other. Second, the overall chain length of 9-AGNRs is much lower than for C90-GNRs. There are hardly any segments present that show a length of more than 10 nm without major defects or kinks, which is due to the higher mobility of the precursor molecules and the missing channeling effect through the surface reconstruction. Another common phenomenon visible in figure 5.4 **c** is the aggregation of GNRs/precursor molecules at step edges. The step edge running from left to right in the upper third of the STM images is almost fully covered with GNRs, whereas clean terraces above and below just show single ribbons present. This has also been observed on other molecular systems on clean metal surfaces,<sup>[192]</sup> and is based on an electrostatic surface dipole moment present at the location of the step edge.<sup>[193]</sup> This aggregation effect can also have a stabilizing effect on the growth of graphene nanoribbons, resulting in longer chains being formed along the edge.<sup>[194]</sup>

Figure 5.4 **d** shows a surface area with five step edges present, and **e** is a zoomed in STM image of the structure in the upper right corner. Here, the resolution allows to resolve individual six-membered carbon rings of the GNRs and thereby prove the exact alignment of 9-AGNRs on monoatomic Au step edges. The GNRs seem to overlap with the substrate step edge, resulting in a decreased apparent width of the ribbon. The bright lobes visible on the edge of the terrace in figure 5.4 **e** appear to be carbon atoms of the armchair edge, sitting slightly out of plane to the substrate. By taking several line scans over the profile marked by the blue line in **e**, a quantitative result for the diminished apparent width could be determined, being  $(0.74 \pm 0.05)$  nm. The width of pristine 9-AGNRs sitting on flat substrate areas however, is  $(0.97 \pm 0.05)$  nm and is in perfect agreement with published experimental data.<sup>[119,191]</sup>

Attempts to develop a geometric model for the exact alignment of the GNRs, surprisingly did not lead to any result. This hints towards an electronic modification of the GNRs molecular orbitals, making the ribbon appear more narrow in the STM image. For a precise explanation however, molecular simulations would be necessary to get an idea how exactly the step edge influences the electronic structure of the GNR. The spatial resolution in figure 5.4 **c-e** is sufficient to reveal, that defects in the ribbon structure become visible. Missing carbon atoms in the precursor molecules lead to defects in the hexagonal lattice of the ribbon upon cyclodehydrogenation. Similar to the case with C90-GNRs some irregular structures can be seen, where individual precursor molecules are attached to at the armchair edge of a 9-AGNR, resulting in triangular attachments on the edge.

STS point spectra were acquired on individual 9-AGNRs to investigate their electronic properties. A typical spectrum of 9-AGNR, which was obtained by averaging over several individual spectra, is shown in figure 5.5. All the individual spectra were taken on similar locations right above

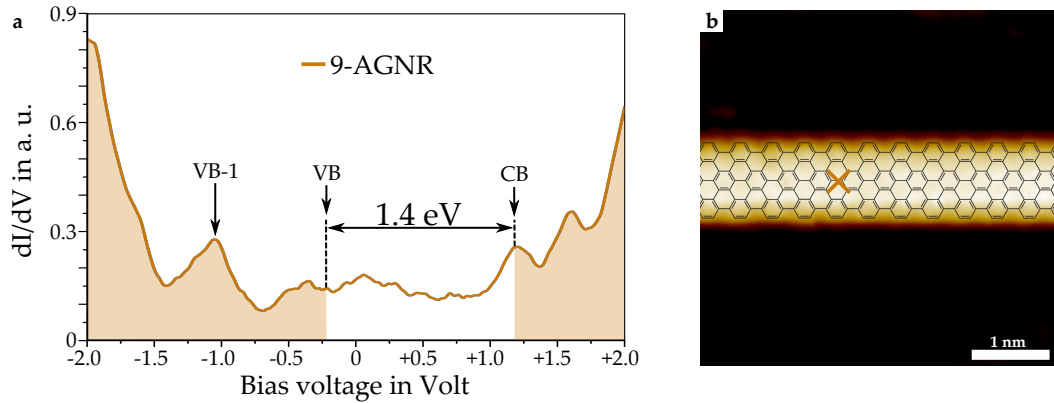


Figure 5.5: **a)**  $dI/dV$  point spectrum of a 9-AGNR. VB and CB edges are colored in orange. ( $I_T = 0.3$  nA,  $V_{\text{mod}} = 20$  mV,  $f_{\text{mod}} = 964$  Hertz) **b)** STM image of a 9-AGNR segment. The measurement location of  $dI/dV$  spectra is marked with a cross. ( $V_B = -1.4$  V,  $I_T = 0.5$  nA)

the ribbons' backbone as marked in **b**. The peak at  $E = -(0.23 \pm 0.02)$  eV is identified as the VB edge, while the CB edge position is determined to be  $E = +(1.20 \pm 0.08)$  eV. The bandgap width of 9-AGNRs can then be determined to be  $E_{\text{Gap}} = (1.43 \pm 0.10)$  eV, which is in good agreement with previously reported results for 9-AGNRs on Au(111).<sup>[112,119,191]</sup> As mentioned before, some earlier works determined the bandgap by using the VB-1, which is why it is marked in the spectrum to avoid any misunderstandings. The energetic location of the VB-1 edge at  $E = -(1.10 \pm 0.05)$  eV is also in good agreement with the results of Merino-Díez et al.<sup>[119]</sup>

## 5.1.3 T90-GNRs

Synthesizing two well known GNR species and characterizing them with STM and STS helped to get a feeling for the measurement characteristics of graphenic nanostructures. The following results are shown here for the first time and have not been published before. The novel GNR precursors in this study were developed with the goal to synthesize new types of GNRs with advanced electronic properties. Starting here, the results of the T90-precursor molecules will be presented.

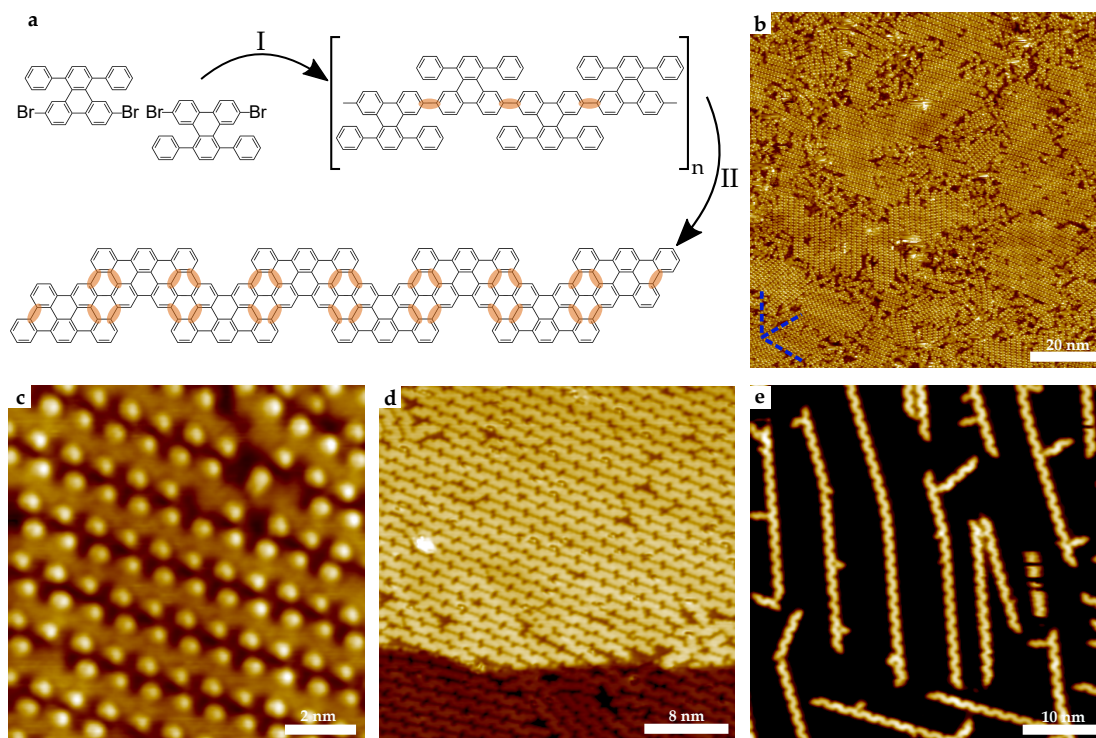


Figure 5.6: **a)** On-surface synthesis route for T90-GNRs. Newly formed covalent bonds are colored in orange. **b)** Large scale image of a densely covered surface area in the polymer stage. The blue dashed lines indicate preferred orientations of the polymer islands. ( $V_B = +0.8$  V,  $I_T = 0.1$  nA) **c)** Detailed image of parallel T90-polymer chains. ( $V_B = +0.5$  V,  $I_T = 0.01$  nA) **d)** Large scale image of T90-GNRs with low surface coverage. ( $V_B = +0.5$  V,  $I_T = 0.1$  nA) **e)** Densely packed T90-GNRs aligned perfectly parallel to each other. ( $V_B = +1.5$  V,  $I_T = 1.0$  nA)

Figure 5.6 **a)** shows the synthesis route for T90-GNRs. The molecular precursors, were deposited onto the Au(111) substrate with the DCT method, which has already been described in detail in section 4.4.3. A first postannealing step (**I**) at  $T \approx 160$  °C led to debromination and subsequent polymerization. The duration of the annealing process is particularly important for these precursors because it strongly influences the degree of alignment between chains. For the sample shown

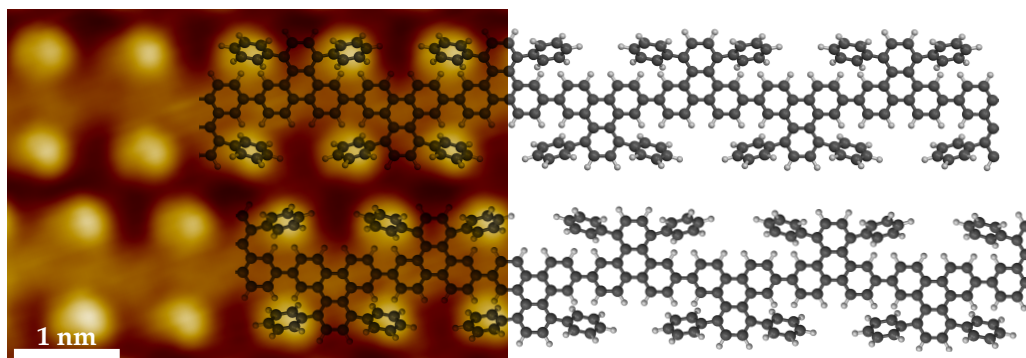
in these images, the temperature was increased at a rate of about  $3 \text{ K min}^{-1}$  until the sample temperature reached  $T \approx 160^\circ\text{C}$ . Already reaching the polymerization temperature also led to the powder residue left on the surface vanish completely. The temperature was then held constant for about 20 min to achieve equilibrium temperature of the sample and to promote parallel alignment of the polymers.

Figure 5.6 **b** and **c** show STM images of the sample covered with polymer chains. In the large scale image (**b**) it is already visible that the polymers tend to form islands in which the individual chains are parallelly aligned and oriented in discrete directions. In the lower left corner of the image, three blue dashed lines are shown, all at an angle of  $60^\circ$  to each other. These lines resemble the orientation of the crystallographic axis of the substrate, which can be reconstructed from the directions of the herringbone pattern on clean surface areas. Looking at the orientation of the T90-polymer islands, it can be observed that they match those directions, meaning that the polymer growth happens epitaxially.

In **c**, a zoomed in STM image of one of those islands is shown, where the parallel alignment is clearly visible. Each polymer chain is furthermore decorated with bright lobes at the edges. These bright features resemble non-planarized phenyl rings which are rotated slightly out of plane. A structural model of such chains is shown in figure 5.7. There, a three-dimensional ball and stick structure model is shown from different perspectives. The STM image in **a** shows two adjacent polymer chains onto which the structural model was superimposed. Due to the two phenyl rings on each precursor molecule that are just connected via one covalent bond to the backbone, they can rotate around that axis which leads to the hydrogen atoms at the edge sticking out of plane. This rotation is caused by the steric hindrance of the hydrogen atoms on the respective phenyl ring and the ones connected to the polymer backbone. In **b** and **c**, two different views on parallelly aligned polymer models are shown. The red regions thereby mark areas in which  $\pi$ - $\pi$  interactions between adjacent phenyl rings lead to attractive forces between neighboring chains. The closer the chains come together, the higher the  $\pi$ -system overlap is, which causes the high degree of parallel alignment on the surface. In this particular case, the attractive forces are so large that the chains overcome the surface reconstruction and instead form closely packed islands. Once the polymer chains have achieved a certain length, further diffusive motion of them is negligible, meaning that the parallel alignment stays intact.

Figure 5.6 **d** shows a densely packed surface area after the second annealing step (**II**) at  $T \approx 440^\circ\text{C}$ . The fully cyclized GNRs are perfectly aligned and closely packed, showing very little defects. In figure 5.6 **e**, a surface area with lower coverage is shown after cyclodehydrogenation. Here the distance between the chains was simply too large to achieve considerable  $\pi$  overlap. The individual chains therefore lie separately and are aligned with the herringbone reconstruction of the surface. Depending on the degree of surface coverage, the average chain lengths do vary, but

a



b



c

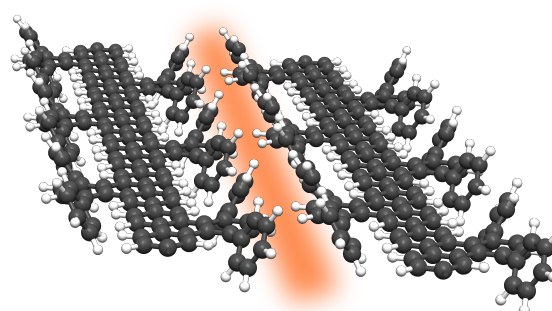


Figure 5.7: 3D models of the molecular geometry of T90-polymers. **a)** Top view on two parallel aligned polymer segments superimposed on an STM image of aligned T90-polymer chains. ( $V_B = +0.5$  V,  $I_T = 0.01$  nA) **b)** A side view with the interacting  $\pi$ -systems colored in red. **c)** Angled view to show the interaction of the polymers on the whole length.

T90-GNRs in general grow extraordinarily long. Chain lengths of up to 100 nm were frequently observed. At step edges and in densely packed regions, the parallel alignment to neighboring chains or the substrate steps stabilizes the growth and thereby increases the length compared to pristine 9-AGNRs.

In the following, the spectroscopic results revealing the electronic structure of T90-GNRs will be discussed. Since these GNRs are novel and have not been studied elsewhere, there was no information about the expected bandgap width or the spatial distribution of electronic states prior to this study available.

Looking at the structural model of T90-GNRs one sees that they can be described as 9-AGNRs with alternating periodic defects of the size of one benzene ring on each side. Those defects, or notches, should have a strong impact on the electronic configuration, since they alter the symmetry of the  $\pi$ -system. Figure 5.8 **a)** shows averaged  $dI/dV$  point spectra of the T90-GNR

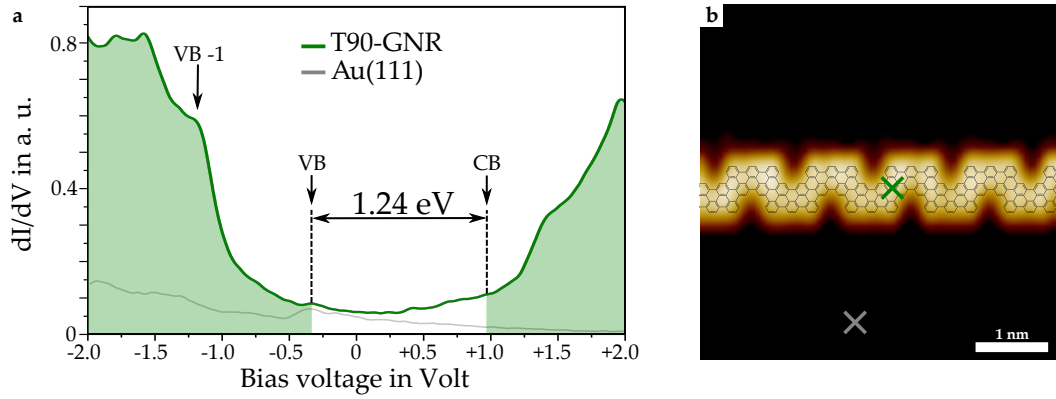


Figure 5.8: **a)**  $dI/dV$  point spectra of a T90-GNR (green) and the Au(111) substrate (gray). VB and CB edges of the T90-GNR are colored in green. ( $I_T = 0.1$  nA,  $V_{\text{mod}} = 20$  mV,  $f_{\text{mod}} = 859$  Hertz) **b)** STM image of a T90-GNR segment. The measurement locations of  $dI/dV$  spectra are marked accordingly. ( $V_B = +0.5$  V,  $I_T = 0.1$  nA)

(green) and the Au(111) substrate (gray). The measurement locations are again marked in the STM image in **b** with crosses in the respective color of the spectrum. When looking at the Au spectrum one sees that it's free of tip artifacts and the surface state peak is located at slightly above  $E = -0.5$  eV as expected. Whereas the T90-GNR spectrum shows a clear VB and CB edge, located at  $E = -(0.33 \pm 0.05)$  eV and  $E = +(0.91 \pm 0.15)$  eV. The VB-1 peak is visible at  $E = -(1.21 \pm 0.10)$  eV. The bandgap is therefore calculated to be  $E_{\text{gap}} = (1.24 \pm 0.20)$  eV, which is slightly smaller than that of 9-AGNRs. All the results of STS measurements are compared in table 5.1.

	VB-1 in eV	VB in eV	CB edge in eV	Bandgap width in eV
T90-GNR	-1.22	-0.33	+0.91	1.24
9-AGNR	-1.1	-0.22	+1.2	1.4
9-AGNR*	-1.17	-0.20	+1.14	1.35

Table 5.1: Direct comparison between the energetic location of VB-1, VB, CB and bandgap of T90-GNR and 9-AGNRs. 9-AGNR\* marks results from Ref. [119]

For all three data sets, the VB-1 and VB edge locations are very close. The CB edge position however is shifted towards lower energies in the case of T90-GNRs. Since the substrate is the same for all compared measurements, it can be concluded that the energetic shift of the CB edge is a direct result of the structural differences. This means that the periodic notches at the edges of the T90-GNR shift the CB edge position towards lower energies.

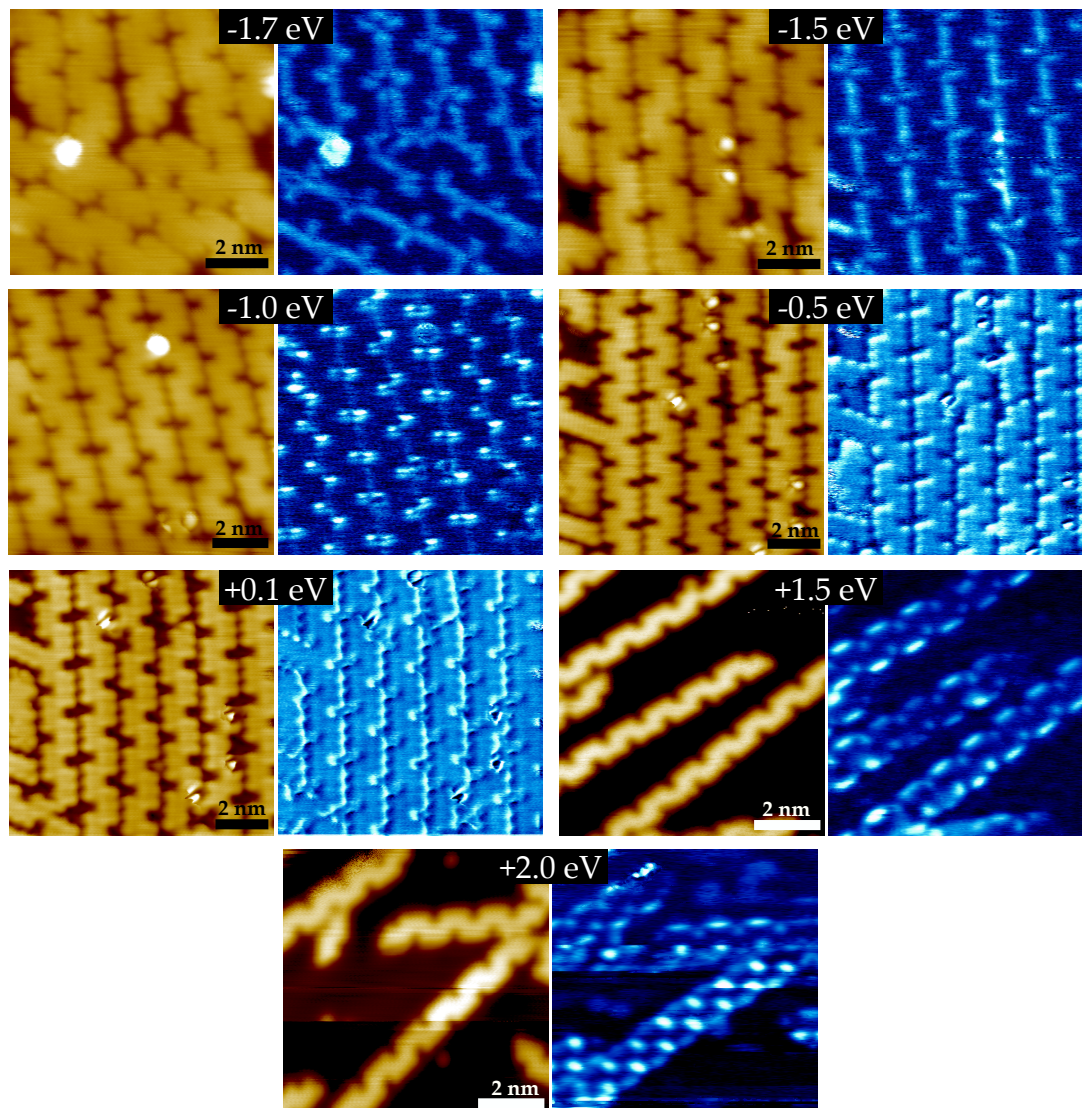


Figure 5.9:  $dI/dV$  maps of T90-GNRs at different energies showing the spacial distribution of electronic states. All maps were taken with a setpoint of  $I_T = 1.0$  nA and with a modulation voltage of  $V_{\text{mod}} = 30$  mV at  $f_{\text{mod}} = 4.371$  kHz.

Graphene nanoribbons are known to have spatially localized electronic states. In armchair GNRs for example, a characteristic armchair edge state, located directly at the position of the edge atoms, has been confirmed on several different AGNRs.<sup>[119,134,143]</sup> The T90-GNR does not possess a pristine armchair edge, the evolution of such an armchair state is thus not certain. To investigate the spatial distribution of electronic states at different energies in T90-GNRs,  $dI/dV$  mapping was used. During these measurements the sample is scanned as usual but with a very low scan speed. The bias voltage is chosen for the energy of interest and is modulated with a

small AC voltage with an amplitude of several mV. This allows for a simultaneous recording of the demodulated signal from the Lock-In amplifier. The result is a spatial map of electronic states, located in a small energy interval, centered around the chosen bias voltage. In the maps shown here, white always resembles areas of high signal amplitudes and it has to be pointed out that the color scheme of each map is adjusted to maximize visibility of the electronic states.

In figure 5.9 the  $dI/dV$  maps are shown in blue with the corresponding STM images in the usual orange color scheme. The respective energy is given above each pair of images. At  $E = -1.7$  eV and  $E = -1.5$  eV, the maps look very similar, with high intensity regions surrounding the GNRs. At  $E = -1.0$  eV however, the intensity is considerably higher at the location of the notches, corresponding to the VB-1 edge. The  $dI/dV$  map at  $E = -0.5$  eV still shows an increased signal originating from the ribbons, while at  $E = +0.1$  eV the measured intensity from the substrate is greater, resulting in high intensity regions between the GNRs. This is not surprising since  $E = +0.1$  eV is located in the bandgap of the GNR, meaning that the main part of the tunneling current stems from tunneling into bulk states of the substrate. At  $E = +1.5$  eV, the CB edge states appear, resulting in higher intensities on the armchair edges and already slightly visible features at the notches. This shows that on the short armchair edge segments of the ribbon, a characteristic edge state is evolving. The energetic and spatial location of these states is in good agreement with the results from other research groups.<sup>[143]</sup> Increasing the energy even further shows that the notch state becomes dominant, overtaking the armchair edge state at  $E = +2.0$  eV.

With these results, a full spectroscopic characterization of the novel T90-GNR has been achieved. The  $dI/dV$  point spectra in combination with  $dI/dV$  mapping revealed a significant change in the bandgap width and the spatial distribution of electronic states.

## 5.1.4 T30-GNRs

In the following section, the first novel precursor molecules with a varied halogenation angle of  $30^\circ$  will be used for the synthesis of T30-GNRs. Two distinct GNRs will be presented, on which a varied halogenation angle drastically changes the structure of the formed ribbon. By adding the bromine atoms in the 7,10 rather than the 6,11 locations,\* the shape of the formed backbone takes a different shape than for a connection angle of  $30^\circ$ . The precursor molecules are now connected in a zig-zag shape, which in this case leads to the formation of nanopores inside the GNR. The results shown here, present the samples prepared with T30-precursor molecules, which were deposited on a clean Au(111) surface by DCT.

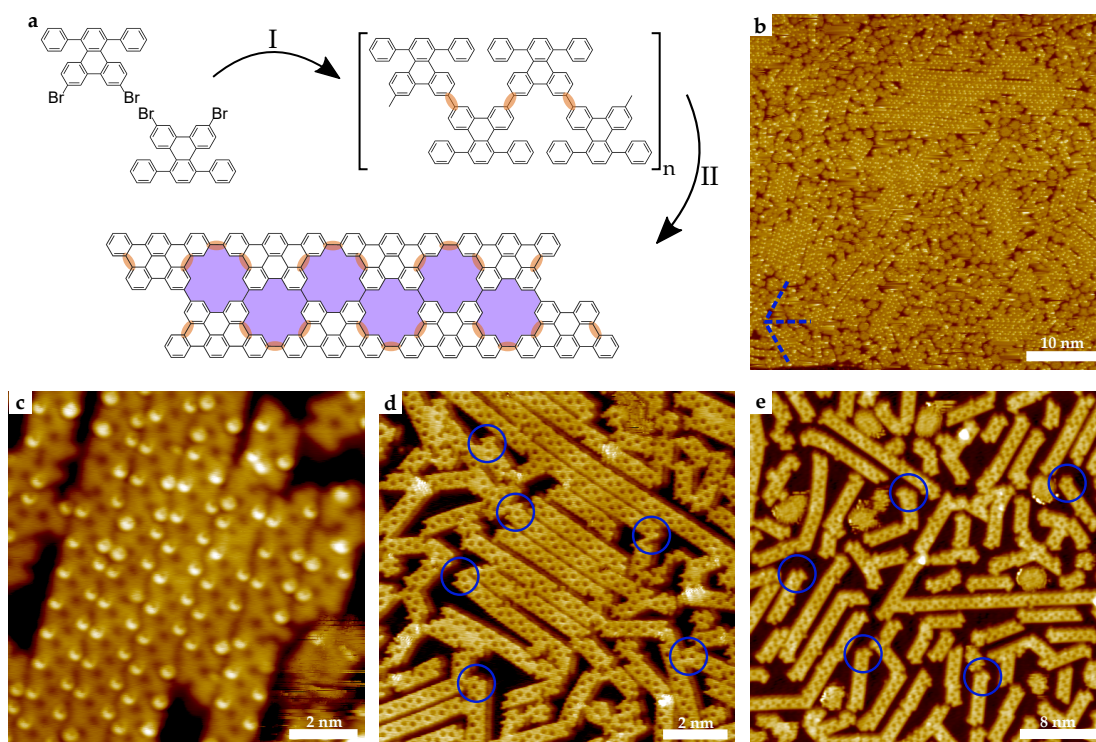


Figure 5.10: **a)** On-surface synthesis route for T30-GNRs. Newly formed covalent bonds are colored in orange. **b)** Large scale STM image showing T30-polymer islands on Au(111). The blue dashed lines represent preferred orientations of polymer chains. ( $V_B = +0.8$  V,  $I_T = 0.1$  nA) **c)** Detailed image of parallel aligned polymer chains. ( $V_B = +0.8$  V,  $I_T = 0.1$  nA) **d)** STM image of parallel aligned T30-GNRs. The blue circles mark edge terminations through differently oriented precursor molecules. ( $V_B = +0.6$  V,  $I_T = 1.0$  nA) **e)** T30-GNRs at lower surface coverage, where no parallel alignment is observable. ( $V_B = +1.0$  V,  $I_T = 0.6$  nA)

Figure 5.10 **a** shows the on-surface synthesis route for T30-GNRs. The polymerization (**I**)

\*The numbering of the locations is based on the respective locations according to the IUPAC notation.

and cyclodehydrogenation temperatures (**II**) were  $T \approx 160^\circ\text{C}$  and  $T \approx 440^\circ\text{C}$  respectively. The nanopores in the structure formula of the fully cyclized GNR are colored in purple for better visualization. Figure 5.10 **b** and **c** show a large and small scale STM image of T30-polymers. In **b** it can be seen that T30-polymers also tend to form islands in densely covered surface areas. However, the size of these islands is much smaller compared to T90-polymers, hinting towards a mechanism that decreases the degree of alignment and hinders the chain growth. The polymer islands do again show preferred orientations of  $60^\circ$  rotational symmetry, which is ascribed to an epitaxial effect of the Au(111) surface structure.

A closer look at the polymer structure reveals the similarity to the T90-polymer with two phenyl rings being located right at the edge, which are able to rotate freely around the covalent bond to the polymer backbone. However, the coupling angle of  $30^\circ$  decreases the distance between adjacent precursor molecules in the growth direction of the ribbon slightly. The phenyls of neighboring precursors are thereby forced closer together and get in the way of each other.

The detailed image of parallelly aligned T30-polymer chains in figure 5.10 **c** reveal a major difference in appearance compared to T90-polymers. If one compares the two structures closely it becomes obvious that instead of two bright lobes per precursor molecules the T30-polymers do just show one and also that these features are not equidistant. To fully understand this, one has to take a closer look onto the three-dimensional structure of the polymer chains.

To clarify this, a detailed image of parallelly aligned T30-polymers together with two explanatory structural models was added in figure 5.11. From the STM image in **a** it becomes clear that the bright lobes do indeed appear irregularly and that only one bright spot per pair of phenyl rings exists. The 3D model in **b** was therefore reconstructed from this image, showing that one of the phenyl rings is forced upwards in the out of plane direction, while the other one is forced downwards. The colors in this model were picked to match the colors of the STM image in the respective location. In the tilted view model on one single polymer chain in figure 5.11 **c**, it becomes apparent that the phenyl rings are indeed resting in a stacked configuration and that the backbone of the polymer has a zig-zag shape. The phenyl ring that is forced upwards appears bright in the STM image, resulting in the bright feature being slightly shifted in position on each molecule.

With this configuration in mind, one can also see why the  $\pi$ - $\pi$  interaction between adjacent chains is significantly lower than for T90-polymers. A conformation as shown in figure 5.11 greatly reduces the  $\pi$ -system overlap between adjacent chains, reducing the attractive interaction. This directly results in a decreased degree of alignment.

Figure 5.10 **d** and **e** show the sample after the second postannealing step leading to GNR formation by cyclodehydrogenation in a highly covered and medium covered region. While the average chain length is approximately the same in both regions, the alignment of the GNRs is very

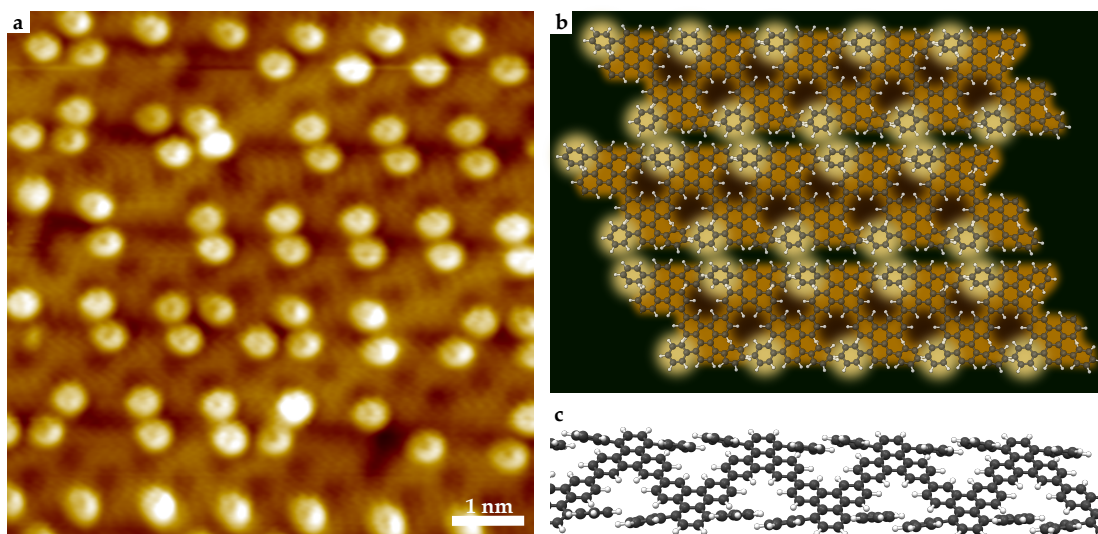


Figure 5.11: **a)** Detailed STM image of parallelly aligned T30-polymer chains. The bright lobes represent rotated phenyl rings on the polymers edges. ( $V_B = +0.8$  V,  $I_T = 0.1$  nA) **b)** 3D model of T30-polymers to demonstrate the parallel orientation. The colored background matches colors in the STM image. **c)** Side view on a single T30-polymer chain. The close proximity of the outer phenyl rings forces them into a stacked configuration.

different. Similar to the case of T90-GNRs, interchain distances determine the degree of alignment and result in parallelly oriented GNRs in highly covered regions and random orientations at lower coverages. Another factor that limits the chain growth is also visible here. Marked in blue are GNR edges that are always terminated by 'wrongly' attached precursor molecules. In contrast to T90-GNRs, where steric hindrance in combination with the  $90^\circ$  connection angle allows for parallel chain growth in a linear fashion, it is here possible that a new precursor molecules is attached to the chain being rotated by  $60^\circ$ . This then leads to the chain breaking its linear progression and most likely ends up terminating the polymer. Upon cyclodehydrogenation, these attached precursors are then clearly visible because the armchair segments do not follow the linear edge of the ribbon.

As mentioned in section 3.3.5, periodic pores can open up a bandgap in otherwise semimetallic graphene and be used as a tool to manipulate the bandgap width of already semiconducting GNRs. T30-GNRs and 12-AGNRs are of identical width and edge geometry. The only difference is that T30-GNRs have pores and 12-AGNRs do not. These two molecules therefore pose as an ideal model system to study the effect of structural holes on the electronic properties of GNRs.

The porous nature of T30-GNRs is already visible in the polymer stage, and the pores are individually distinguishable when the whole structure is planarized. Due to the porosity being induced by the coupling angle of precursor molecules, the pores are highly periodic and equal

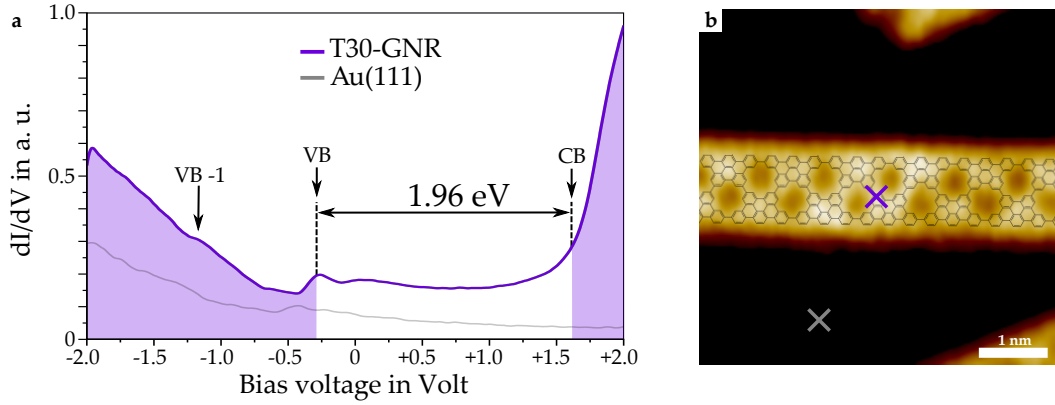


Figure 5.12: **a)**  $dI/dV$  point spectra of a T30-GNR (purple) and the Au(111) substrate (gray). VB and CB edges of the T30-GNR are colored in purple. ( $I_T = 0.1$  nA,  $V_{\text{mod}} = 20$  mV,  $f_{\text{mod}} = 859$  Hertz) **b)** STM image of a T30-GNR segment. The measurement locations of  $dI/dV$  spectra are marked accordingly. ( $V_B = +1.0$  V,  $I_T = 1.0$  nA)

in size, with a pore diameter of 0.32 nm. To investigate the electronic structure of T30-GNR, scanning tunneling spectroscopy was used to measure the  $dI/dV$  point spectra shown in figure 5.12 **a**. The purple curve represents the  $dI/dV$  signal, again averaged over several measurements. The prominent peak at  $E = -(0.27 \pm 0.05)$  eV is identified as the VB edge position and the CB edge is located at  $E = +(1.67 \pm 0.10)$  eV, visible as a small shoulder on the fast rising edge. The VB-1 position is also marked in the plot for clarification. The  $dI/dV$  point spectrum of the clean Au(111) surface is also shown in gray to verify the tip condition.

Figure 5.12 **b** shows a detailed STM image of a T30-GNR segment together with a structural model. The superimposed model shows the ribbons structure is in perfect agreement with the theoretical model and free of defects. The measurement locations of the  $dI/dV$  spectra are marked with crosses accordingly.

Similar to T90-GNRs one can compare the VB and CB edge locations of T30-GNRs to pristine 12-AGNRs to investigate the electronic modifications due to the pore structure directly. For a direct comparison, the results of Merino-Díez et al, who spectroscopically analyzed 12-AGNRs on Au(111), were used. The results are displayed in table 5.2.

	VB-1 in eV	VB in eV	CB edge in eV	Bandgap width in eV
T30-GNR	-1.27	-0.29	+1.67	1.96
12-AGNR*	-0.84	-0.18	+0.9	1.13

Table 5.2: Direct comparison between the energetic location of VB-1, VB, CB and bandgap of T30-GNRs and 12-AGNRs. The \* marks results from Ref. [119]

Looking at these results, it is immediately obvious that the electronic structure of T30-GNRs is different from that of pristine 12-AGNRs. The large shift in the position of the conduction band edge results in a much larger bandgap of  $E_{\text{Gap}} = (1.96 \pm 0.15) \text{ eV}$ . Since the periodic vacancies are the only structural difference of both systems, it is suggested to address this energetic shift of the CB edge to the presence of the nanopores in the ribbon's backbone. To further investigate the electronic structure  $dI/dV$  mapping was used to probe localized electronic states on the T30-GNRs. The results are shown in figure 5.13.

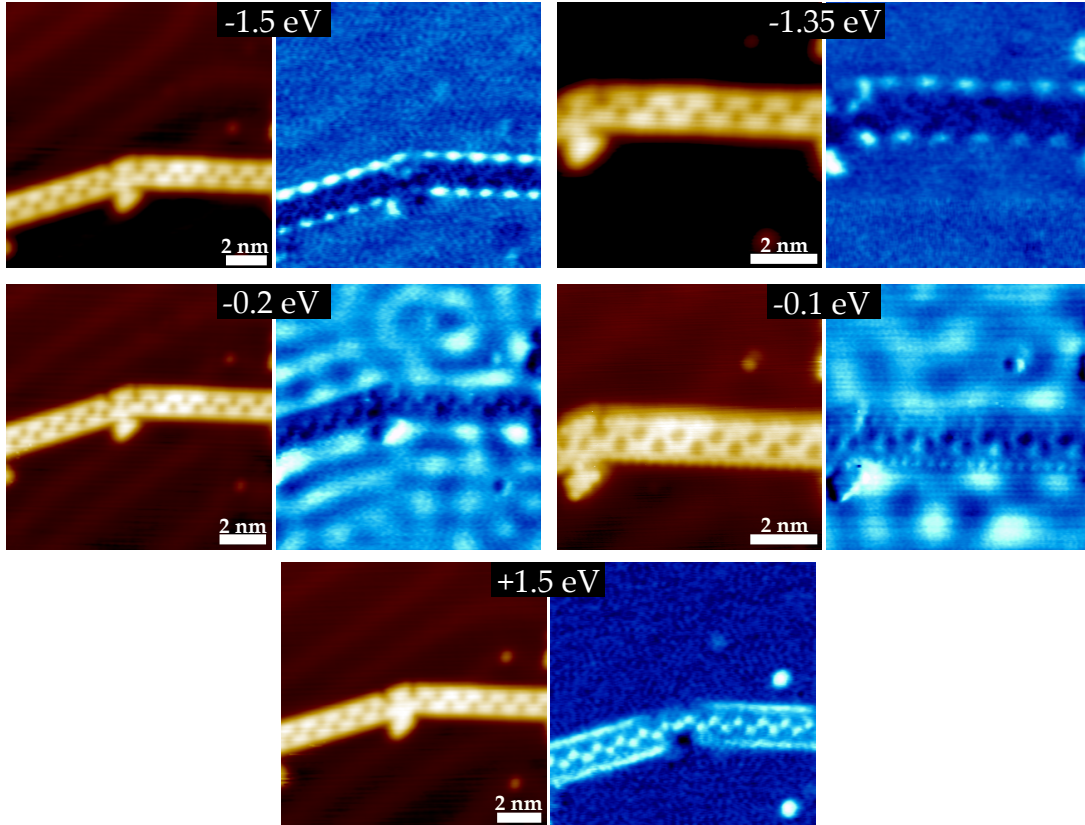


Figure 5.13:  $dI/dV$  maps of T30-GNRs at different energies showing the spacial distribution of electronic states. All maps were taken with a setpoint of  $I_T = 1 \text{ nA}$  and with a modulation voltage of  $V_{\text{mod}} = 30 \text{ mV}$  at  $f_{\text{mod}} = 4.371 \text{ kHz}$ .

At  $E = -1.5 \text{ eV}$  and  $E = -1.35 \text{ eV}$  the armchair edge of the T30-GNR appears bright, while the backbone and the pores show little to no intensity. It is suspected that the visible periodic pattern inside the armchair state is due to a modification based on the nanopores in the backbone. It is obvious that the periodicity of the pores and the induced modulation in the armchair state share the same characteristic length. At  $E = +1.5 \text{ eV}$  close to the CB edge, the well known armchair edge state can be observed as bright straight features on both edges of the GNR. Additionally,

a new state located right above the pores can be seen. These high intensity regions show that additional electronic states are induced in the ribbon due to the porosity, determining the new CB edge position. The energetic location of these states matches the location of the CB edge in the  $dI/dV$  point spectrum shown in figure 5.12 perfectly.

The maps at  $E = -0.2$  eV and  $E = -0.1$  eV are not so straight forward to discuss, because they show a strong background signal coming from the substrate. The wavelike pattern visible besides the T30-GNR resembles the scattered Shockley surface state which, depending on what energy is set and therefore what  $k_{||}$  is probed, appears as a surface wave of different periodicity. This signal is much stronger than the intensity of the GNRs electronic states, which can therefore just barely be resolved. At  $E = -0.1$  eV, pieces of the ribbon appear brighter again and show that there is again a periodically modulated state present at the edge.

From these results, it is concluded that the incorporation of nanopores in a already semiconducting GNR does indeed change the bandgap width and also that already present electronic states can be modified by these structural changes.

## 5.1.5 C30-GNRs

In this section, the on-surface synthesis of C30-GNRs will be presented. Similar to T30-GNRs, where the halogenation angle of the C30-precursor molecules leads to the formation of nanoporous ribbons, it was also expected for these precursors. However, due to the two additional phenyl rings on each precursor, the resulting edge structure is chevron like and not straight as in T30-GNRs. The question here was if the nanopores would affect the electronic properties of chevron like GNRs in the same way as they did for AGNRs. To investigate the growth of C30-GNRs, the molecular precursors were deposited onto a clean Au(111) substrate via DCT. The temperature was increased in steps of  $\Delta T = 20^\circ\text{C}$  until the sample temperature reached  $T \approx 450^\circ\text{C}$  and was held there for about 20 min.

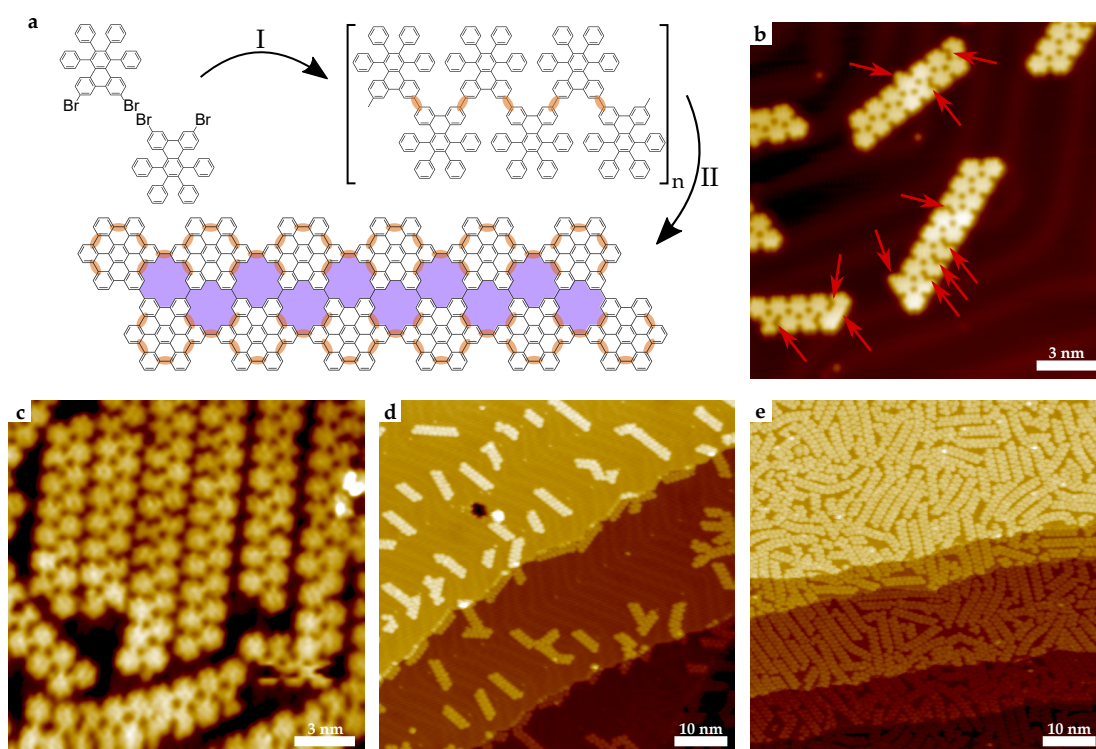


Figure 5.14: **a**) On-surface synthesis route for C30-GNRs. Newly formed covalent bonds are colored in orange. **b**) Detailed STM image of individual C30-GNRs on Au(111). Defects in the structures are marked with red arrows. ( $V_B = +0.4\text{ V}$ ,  $I_T = 1.0\text{ nA}$ ) **c**) STM image of parallelly aligned C30-GNRs. ( $V_B = +1.0\text{ V}$ ,  $I_T = 0.5\text{ nA}$ ) **d**) Large scale image of an area with low surface coverage ( $V_B = +1.0\text{ V}$ ,  $I_T = 0.5\text{ nA}$ ) **e**) Large scale image of an area with high surface coverage. ( $V_B = +1.0\text{ V}$ ,  $I_T = 0.6\text{ nA}$ )

Figure 5.14 **a** shows the on-surface synthesis route for C30-GNR formation. Unfortunately, the polymer stage of these molecules is hardly observable with STM. After the usual first synthesis

step at  $T \approx 180^\circ\text{C}$ , the precursors were expected to have formed polymer chains, however this stage of the molecules was not resolvable. It is suspected that in the polymer stage the sample is simply too unstable and that there might still be a lot of loose adsorbates left on the surface. Just after reaching the cyclodehydrogenation temperature does the sample become stable and STM can be performed reasonably.

The structure formulas show clearly that cyclodehydrogenation happens in each precursor molecule individually and these cyclized hexagons are linked to each other via four single covalent bonds. Figure 5.14 **b** shows a detailed STM image of fully cyclized C30-GNRs, where the herringbone reconstruction of the surface is also visible beneath the GNRs. The C30-GNRs do not show any signs of a template effect as they are oriented randomly on the surface. A closer look into the ribbon structure reveals many defects, which are created by the incorporation of defective precursor molecules. The resulting structures show missing or additional phenyl rings, some of which were marked with red arrows in **b**, breaking the symmetry of the ribbon. In figure 5.14 **c** it can be seen that in areas with higher surface coverage a parallel alignment of the GNRs is preferred. From this, it can be concluded that there is a similar coupling mechanism as for T90- and T30-GNRs, creating attractive interactions between adjacent chains by the  $\pi$ -system overlap of rotated phenyl groups. The two images in **d** and **e** show 100x100 nm surface areas with different coverages. In both images it is obvious that the average chain length of C30-GNRs is rather low and that the chain length seems to be mostly independent of the surface coverage. This is in contrast to previously discussed systems, where lower coverages and/or parallel alignment stabilized the growth of GNRs. If one compares this case with the edge terminations of T30-GNRs, one sees that a similar mechanism is possible for C30-GNRs. 'Wrongly' attached precursor molecules would break the linear chain growth and likely terminate the GNR. Now however, the cyclized structure of these molecules is not distinguishable from the rest because of their rotational symmetry. It is therefore concluded that this mechanism in addition to the high number of defects present in the precursor molecules is responsible for the overall shorter chains.

Because of the larger defect density in the GNRs it was difficult to find defect free segments of C30-GNR, longer than six molecular units, for spectroscopy. Thus, spectra were taken on rather short pristine segments. As for the other GNRs, the spectra presented in figure 5.15 **a** shows an average over several individual spectra measured at different locations across the sample.

Looking at the background Au spectrum shown in gray it can be seen again that it is mainly featureless and shows the characteristic step-like feature at  $E \approx -0.5$  eV. The additional peak at  $E = -1.3$  eV is usually not present in clean gold spectra and therefore has to be a tip artifact. This is also verified by the feature reappearing in the  $dI/dV$  spectra of C30-GNRs. Where the same peak appears as a distinct shoulder in the fast rising valence band. Nonetheless, the shown C60-GNR spectrum shows distinct features that can be identified as GNR typical electronic states.

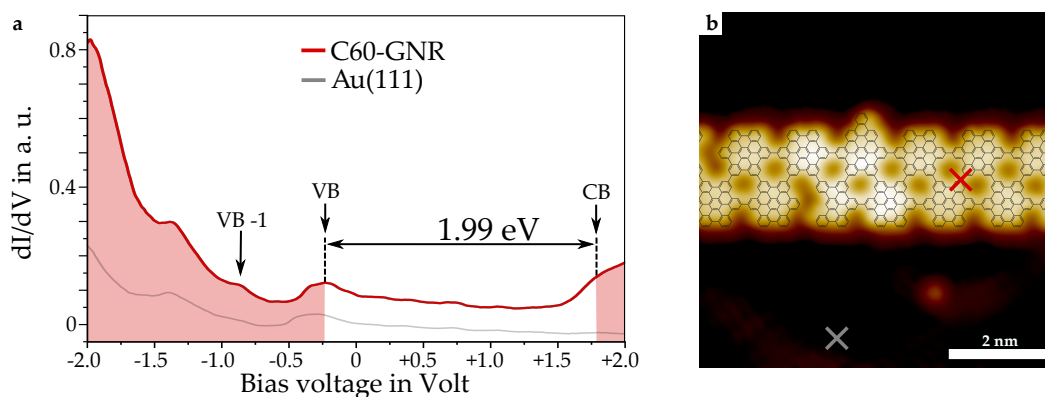


Figure 5.15: **a)**  $dI/dV$  point spectra of a C30-GNR (red) and the Au(111) substrate (gray). VB and CB edges of the C30-GNR are colored accordingly and the VB-1 location is marked. ( $I_T = 0.1$  nA,  $V_{\text{mod}} = 20$  mV,  $f_{\text{mod}} = 859$  Hertz) **b)** Detailed STM image of a C30-GNR segment. The measurement locations of  $dI/dV$  spectra are marked accordingly. ( $V_B = +0.2$  V,  $I_T = 1.0$  nA)

The VB-1 edge visible as a peak in the spectrum at  $E = -(0.71 \pm 0.10)$  eV and the VB edge at  $E = -(0.22 \pm 0.05)$  eV appear as expected at negative bias voltages. Compared to the other GNRs presented here, the VB-1 peak appears slightly shifted towards higher energies with the peaks in all other spectra located below  $E = -1.0$  eV. The characteristic rising edge visible at  $E = +(1.77 \pm 0.12)$  eV is identified as the onset conduction band edge. Although not being as prominent as in other GNR spectra, the increased signal leaves no doubt about the onset of the conduction band.

Knowing these energies, it was possible to determine the bandgap of the C30-GNRs as  $E_{\text{Gap}} = (1.99 \pm 0.17)$  eV. It is slightly larger than that of T90- or T30-GNRs, however the bandgap of chevron like GNRs has been shown to be a bit larger in general compared to other ribbons.<sup>[125,136,189]</sup> Unfortunately, there are no comparable pristine GNRs of similar edge structure from which these results could be set into perspective. However, looking at the experimental bandgap of AGNRs with similar widths like 17-, 18- or 21-AGNRs, ranging from 0.19 eV to 0.9 eV, it becomes clear that the bandgap of C30-GNR is considerably larger.<sup>[112,137,195]</sup> With a width of almost 2 nm, it is definitely one of the wider GNRs and one would therefore expect the bandgap of a nonporous GNR of similar width to be smaller. To further investigate the spatial distribution of electronic states on C30-GNRs,  $dI/dV$  mapping was used, and the results are shown in figure 5.16.

In the cases of T90- and T30-GNRs, it was already found that bright edge states dominate the  $dI/dV$  maps below the onset of the valence band and above the conduction band edge. This is also the case here, with the exception that now there are also bright features appearing inside the GNR at  $E = -1.0$  eV and  $E = -0.8$  eV. It is suspected that these features arise due to the

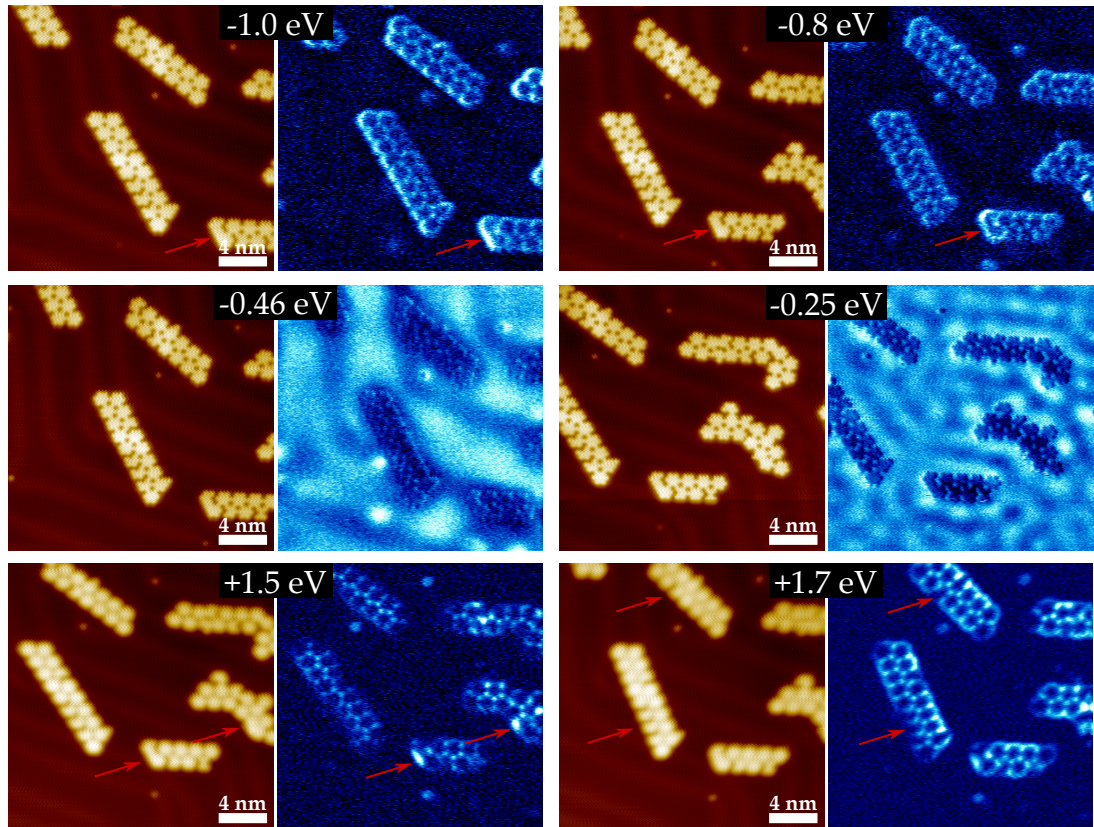


Figure 5.16:  $dI/dV$  maps of C30-GNRs at different energies showing the spatial distribution of electronic states. Defects resulting in modified  $dI/dV$  signals are marked with red arrows. All maps were taken with a setpoint of  $I_T = 1.0$  nA and with a modulation voltage of  $V_{\text{mod}} = 30$  mV at  $f_{\text{mod}} = 4.371$  kHz.

highly symmetric and cyclized structure of the individual hexagonally shaped precursor molecules, leading to a bright edge states being wrapped around each of these structures. It is also evident that these states become quenched when a structural defect due to a missing phenyl ring is incorporated. If additional phenyls are connected to the GNR and create a small piece of fully graphenic lattice, the signal is increased as marked by the red arrows in the maps at  $E = -0.8$  eV and  $E = +1.5$  eV.

The maps at  $E = -0.46$  eV and  $E = -0.25$  eV show the ribbons electronic states near the Fermi energy, again being superimposed by a strong surface state signal. What is especially interesting here is that at  $E = -0.46$  eV the surface state seems to be unaltered by the GNR adsorbates while at  $E = -0.25$  eV it appears scattered by the GNR structures, leading to interference patterns in between the ribbons. The map at  $E = +1.5$  eV clearly shows the quenched edge state at the sites of defective precursors and also hints towards the onset of a pore state, being located above each nanopore in the GNR. At  $E = +1.7$  eV both of these states show further increased intensity. The edge state surrounding each precursor molecules allows it to even see the covalent bonds between

them, appearing as dark lines in the otherwise bright edge of the individual hexagons. The pore state also gained significant intensity, now appearing as bright dots above each pore. Marked with red arrows in this map are locations of defective precursor molecules. One can see that the edge state in these precursor molecules is quenched completely, resulting not just in a low intensity at the location of the defect, but rather a complete eradication of the outer edge state on the respective hexagonal building block.

From these results it is concluded, that even though the C30-GNR is a rather wide nanoribbon, the bandgap is still comparable to the one of pristine C90-GNRs and porous T30-GNRs. In addition, it is larger than theoretically expected for a GNR of the similar width. It is also observable that the quality of the precursor molecules strongly affects the electronic properties of the final nanostructures, meaning that atomic precision of the resulting GNRs is absolutely necessary.

### 5.1.6 Conclusion and outlook

In conclusion, this section presents the synthesis of five different graphene nanoribbons by on-surface molecular self-assembly. For this thesis, three novel GNR precursor molecules were designed, which are structurally similar to the well known C90-precursor. These molecules were meant to result in completely new GNR structures, showing different induced electronic properties based on structural modifications. It was found that all three precursors were suitable for the on-surface bottom-up synthesis. Used with the newly developed DCT method described in section 4.4.3 reliable and reproducible results could be obtained.

At the beginning of this chapter, two well known GNR precursors, namely C90- and 9-A-precursor molecules, were used to figure out the synthesis parameters. With the goal of synthesizing heterojunctions out of these molecules, it was inevitable to have precise knowledge about characteristic times and synthesis temperatures. These measurements showed great results, which were in perfect agreement with previously published data on Au(111) supported C90-GNRs and 9-AGNRs. It also helped to figure out the necessary parameters for spectroscopic measurements.

Regarding the growth of the individual nanoribbons it was found that, while T30- and C30-GNRs show average chain lengths of 10 nm-20 nm, T90-GNRs grow extraordinarily well on a Au(111) surface. With maximum chain lengths of over 100 nm, which is only rarely seen for on-surface synthesized GNRs, they appear to be promising candidates for the future integration into electronic devices. It was also found that the individual GNRs align parallelly in densely covered surface areas. This parallel alignment stems from  $\pi$ - $\pi$  interaction of neighboring rotated phenyl rings during the polymer stage, resulting in attractive forces between the polymers. As it will play a crucial role in the synthesis of porous nanographenes, presented in section 5.4, it shows that this alignment is a highly beneficial feature. Even when thinking about the use of individual GNRs, such large arrays of parallelly aligned chains are perfect for the construction of graphene nanoribbon based FETs.

While the T90-GNR can be described as a 9-AGNR with a notched edge configuration, the structures of the T30- and C30-GNRs are a little more complicated. Due to the change in halogenation angle, the precursor molecules form a zig-zag shaped backbone. Upon cyclization of the molecule, this results in a periodic arrangement of equally sized nanopores inside the GNR. Such induced porosity in GNRs by the design of the precursor molecule had only been published in a small number of research works until this point. Therefore, the information about such GNRs was very limited, which is why an extensive study of the electronic properties of these ribbons followed. The influence of the nanopores on the GNRs bandstructure still remained to be uncovered.

With  $dI/dV$  point spectra and  $dI/dV$  maps, it was possible to determine a bandgap of all these GNRs and explore the spatial distribution of individual electronic states. As it was found, the

notched edges of T90-GNRs as well as the periodic vacancies in T30- and C30-GNRs result in additional electronic features in the  $dI/dV$  maps. These induced electronic states are a direct result of structural modifications of the GNR structure, as they are not present in their pristine counterparts. It is therefore not surprising that the bandgap of these ribbons is substantially different. The measurements revealed a shift of the conduction band edge to higher energies in the case of T30-GNRs, thereby enlarging the bandgap by about 86 %. With these results, it was possible to gain a first insight into the influence of porosity onto the electronic structures of GNRs.

In a further step, more precursor molecules with a halogenation angle of  $30^\circ$  are meant to be synthesized. With more porous graphene nanoribbons available, the investigation of the electronic modifications due to the pores will be easier. Since these results are currently under publication, the hope is to get additional information out of theoretical calculations soon.

## 5.2 Triangle molecules

Looking closely at the T30- and C30-precursor molecules, one could think of another way to piece these molecules together. Instead of forming quasi one-dimensional GNRs, they could also form triangular molecules, based on their rotational symmetry. Such triangular structures were easily obtained in solution, however on the surface during the experiments in section 5.1.4 and section 5.1.5, such structures were only rarely observed. This is therefore an example that on-surface synthesis can produce different results than solution-based synthesis.

In this section, such triangular molecules were synthesized in solution and then placed on a Au(111) surface via DCT. The so prepared samples were then postannealed to compare the results to the synthesis of T30- and C30-GNRs from the molecular precursors shown in figure 5.1. The following sections will present the results obtained from both T30-triangle and C30-triangle molecules.

### 5.2.1 C30-triangle

The C30-triangle molecules, are built out of three C30-precursors connected in a circular fashion. The individual C30-precursors were connected via a Yamamoto coupling reaction<sup>[196]</sup> in solution. Afterwards, the triangular molecules were deposited onto the surface using the usual DCT approach. The sample was afterwards annealed to  $T \approx 200\text{ }^{\circ}\text{C}$  to guarantee desorption of all atmospheric residue. The goal here was to get images of non-cyclized C30-triangles in the polymer stage with the STM. Figure 5.17 **a** presents the synthesis route for C30-triangles in solution. The STM images show the sample after the abovementioned annealing step. In **b** an area with low surface coverage reveals the intact herringbone reconstruction of the surface underneath the molecules. The first thing one has to notice is that the molecules are already fully planarized, meaning that cyclodehydrogenation already happened. To avoid any errors it was tried several times to prepare the sample at even lower temperatures but always ended up finding the molecules fully cyclized. This means that the triangular precursor structure drastically reduces the cyclodehydrogenation temperature compared to the other GNR precursors, which usually take temperatures of more than  $T \approx 440\text{ }^{\circ}\text{C}$  to fully cyclodehydrogenate. With the cyclodehydrogenation temperature being more than 50% lower, the question is raised what actually determines this temperature.

It is also observable that even at such low coverages, the molecules tend to adsorb on the fcc locations of the Au surface. The kinks of the herringbone reconstruction are especially likely to trap molecules diffusing over the surface. Looking at the image in **c** this idea of a strong template effect becomes even more evident. In this image, the coverage is higher and the molecules closely follow the herringbone pattern, resulting in a wavelike pattern of C30-triangles. However, even

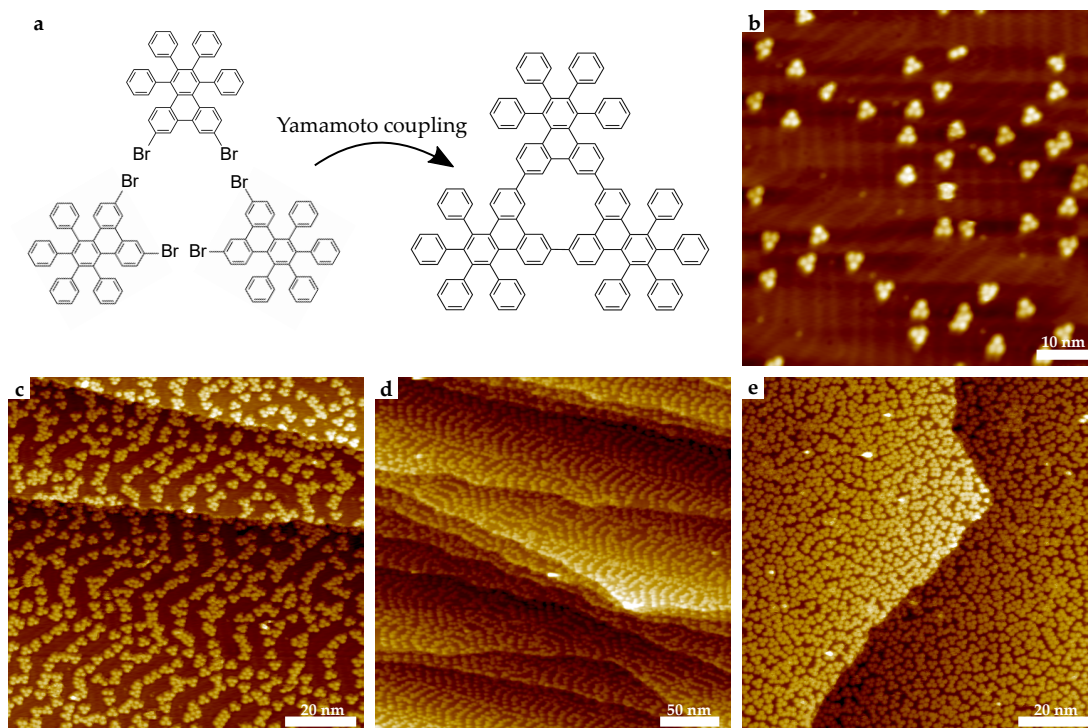


Figure 5.17: **a)** Solution synthesis step to form C30-triangle molecules out of C30-precursors. **b)** STM image of single precursor molecules on Au(111) with low surface coverage. **c)** Image of an area with medium surface coverage. The precursors align in the herringbone reconstruction. **d)** Large STM image showing the template effect extending over several step edges. **e)** Areas with high coverages show no template effect anymore but densely packed precursor molecules. (All images:  $V_B = +1.0$  V,  $I_T = 0.1$  nA)

though the template effect is particularly large here, the molecule-substrate interaction is still low enough for the herringbone pattern to exist in an unaltered fashion. In Figure 5.17 **d** a large scale image of the sample surface is presented, showing the homogeneously covered surface with the herringbone template extending over several step edges. Only when increasing the surface coverage even further is this template effect overcome by the intermolecular interactions. Looking at the STM image in **e**, it can be seen that at coverages around one ML the surface is covered by closely packed randomly oriented molecules.

One also has to notice from the STM images that the molecules do not form dimers, trimers or larger islands, instead they always keep a distance to their nearest neighbor. Obviously, there must be some kind of repulsive interaction between the molecules. Such repulsive interactions on surfaces have already been described in section 2.3.2, where the charge pillow model seems to apply to C30-triangles. In fact, this case is very similar to the one reported by Rojas et al., who observed a similar effect with tetraphenyl porphyrins on a Cu(111) surface.<sup>[197]</sup> Taking a closer look into the self-assembly and template effect of the molecules, several STM images of areas with

similar surface coverage of approximately 0.7 ML were analyzed in detail. Figure 5.18 **a** shows a typical image of a sample, where all precursor positions were marked with crosses. Red crosses indicate molecules sitting in the fcc areas of the surface reconstruction and blue crosses mark precursors that are located on the hcp sites. The intermolecular distances  $r_1$  and  $r_2$  were extracted from a total of 400 distances measured, which are presented in the histogram in **b**.

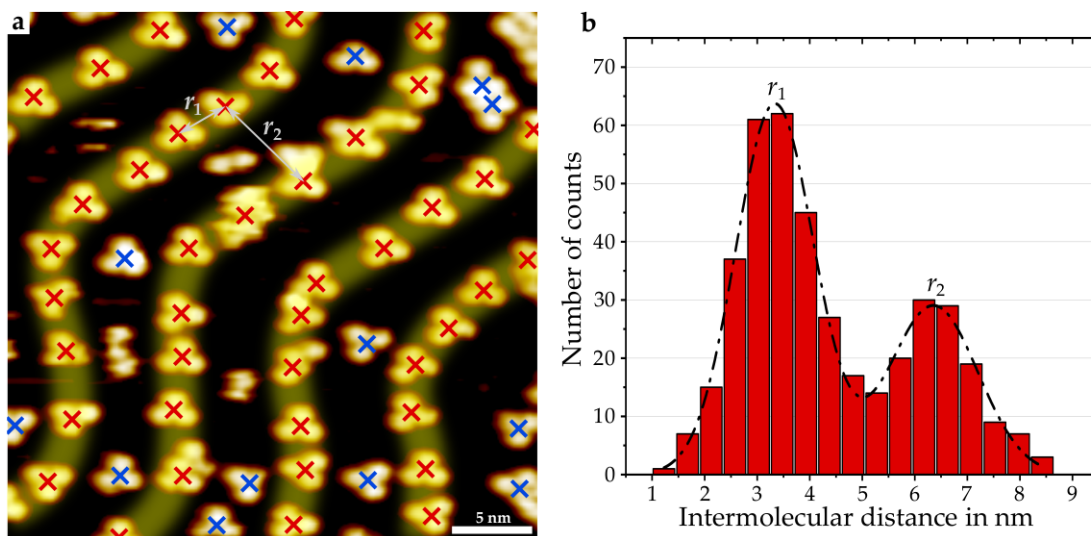


Figure 5.18: **a**) STM image of ordered precursor molecules on a reconstructed Au(111) surface. Red crosses mark molecules adsorbed on the herringbone pattern indicated in yellow, blue crosses mark precursors that do not align with the pattern. Distances  $r_1$  and  $r_2$  mark intermolecular distances alongside the reconstruction pattern and across of it. ( $V_B = +1.0$  V,  $I_T = 0.1$  nA) **b**) Histogramm of interatomic distances taken from several individual STM images with similar surface coverage. The dashed line resembles a fitted double normal distribution.

It is clear to see that the values of intermolecular distances are distributed around two mean values, corresponding to the distances in line with the surface template ( $r_1$ ) and across that pattern ( $r_2$ ). Fitting a double normal distribution to these datapoints gives the dashed line, from which the respective values of

$$r_1 = (3.34 \pm 0.23) \text{ nm} \qquad r_2 = (6.36 \pm 0.05) \text{ nm},$$

can be extracted. Since the C30-triangles are adsorbed in the fcc trenches of the surface reconstruction, it is not surprising that the value of  $r_2$  is close to the experimental value of about 6.0 nm which can be deduced from the measurements of clean Au(111) or other research works.<sup>[198,199]</sup> The in line distances  $r_1$  can be directly interpreted as a measure of the strength of the repulsive interaction between individual molecules.

Looking at this sample configuration, the next logical step was to initiate diffusion and thereby self organization of the molecules through thermal annealing. As it was shown earlier, it is also possible to promote a second dehydrogenation process of already cyclized molecules to link them together. The goal here was to create large two-dimensional islands of covalently bound C30-triangles. The sample was therefore annealed at  $T = 450\text{ }^{\circ}\text{C}$  for  $t = 30\text{ min}$  which resulted in an interesting reorientation of the molecules, shown in figure 5.19.

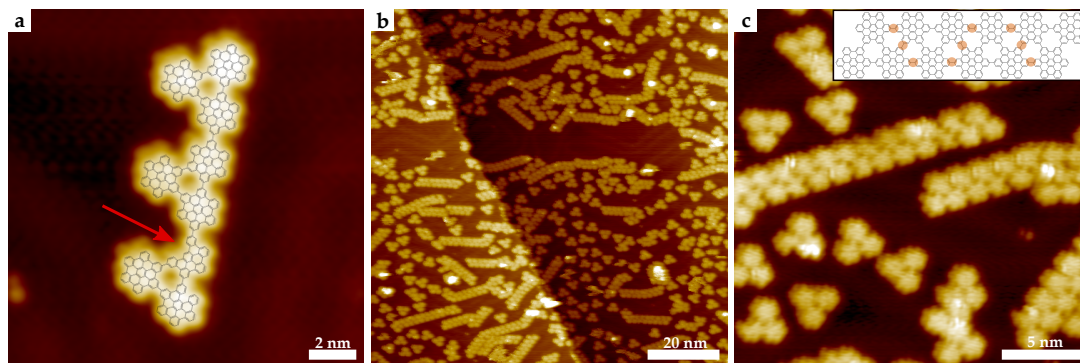


Figure 5.19: **a)** STM image of a trimer formed out of three individual precursor molecules superimposed with a structural model. The red arrow indicates a missing phenyl ring at one of the precursors. ( $V_B = +1.0\text{ V}$ ,  $I_T = 0.5\text{ nA}$ ) **b)** Large scale image showing ribbon formation in areas with higher surface coverage. ( $V_B = +1.0\text{ V}$ ,  $I_T = 0.1\text{ nA}$ ) **c)** Detailed image of the formed porous graphene nanoribbons next to some individual precursor molecules with the inset showing the chemical structure of the GNRs with the newly developed covalent bonds highlighted. ( $V_B = +1.0\text{ V}$ ,  $I_T = 0.1\text{ nA}$ )

It is clear to see that the dehydrogenation in combination with enough thermal energy to overcome the repulsive interaction led to the formation of covalent bonds between individual C30-triangle molecules. In **a**, an STM image with particularly good spatial resolution of a newly formed trimeric structure is shown. This linear configuration of three interconnected C30-triangles is superimposed with a structural model to show that the theoretical structure fits perfectly. Due to the good spatial resolution it is even possible to recognize the exact location of a defect, marked with a red arrow.

Since this structure was found in an area with low surface coverage, the individual molecules have no preferred orientation relative to each other. The location of the covalent bonds between them are therefore in arbitrary locations. However if looking at figure 5.19 **b** reveals that in areas with higher surface coverage, the molecules start to assemble into one dimensional ribbons. This is rather surprising, since the molecules themselves show a threefold symmetry, which would hint towards a possible arrangement into two-dimensional islands. To find ribbon structures here was therefore really unexpected and it meant that a symmetry breaking mechanism for the intermolecular interaction had to exist.

Between the ribbons, depletion zones are created as a direct result of the decreased intermolecu-

lar distances. The length of the chains varies between 10 nm and 20 nm and the orientation along the herringbone reconstruction is still recognizable. In **c** a zoomed in STM image of the these ribbons is shown, showing that they are structurally equal to C30-GNRs. The structure formula in the upper right corner reveals that each triangle molecule is covalently bound to its neighbors in six different locations, forming the same porous backbone structure as in C30-GNRs.

As a mechanism for the formation of these GNRs it is proposed that the precursors start to diffuse in the directions given by the herringbone channels when the temperature is increased. If two molecules by chance overcome their repulsive interaction and form a dimer, the charge pillow changes shape, resulting in a reduced repulsive force along the growth direction. It is therefore easier for the next molecules to connect to the end of the already existing chain. This chain growth then stops as soon as the depletion zone around the ribbon becomes too large, or if a molecule is attached in the wrong orientation, prohibiting the next one from connecting to the chain.

This shows that it is possible to create C30-GNRs by using a different approach of combined solution and on-surface synthesis. However, it has to be stated that this route also leads to a lot of residue present on the sample like individual C30-triangles and structures of randomly connected molecules.

### 5.2.2 T30-triangle

The second triangular molecule is the truncated version of the C30-triangles. In analogy to figure 5.17 **a** these molecules are formed out of three individual T30-GNR monomers via Yamamoto coupling in solution. The sample preparation procedure is analog to C30-triangles. Looking at STM images in figure 5.20 it becomes clear that these molecules, although being structurally similar to the C30-triangles, behave very differently when deposited onto a Au(111) surface.

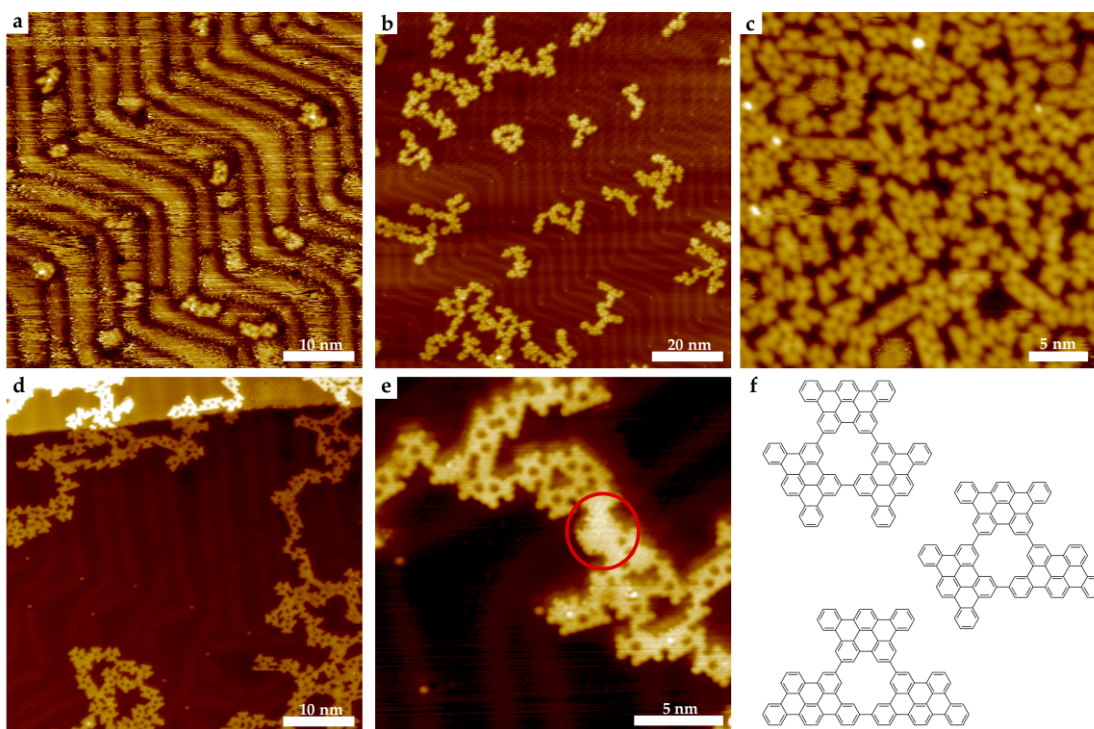


Figure 5.20: **a**) STM image showing single adsorbed molecules on top of the herringbone reconstructed surface with mobile molecules present. ( $V_B = -2.0$  V,  $I_T = 0.1$  nA) **b**) Low coverage area after the second annealing step. ( $V_B = +1.0$  V,  $I_T = 0.1$  nA) **c**) Higher coverage area showing densely packed precursor molecules and short GNR segments. ( $V_B = -0.8$  V,  $I_T = 0.1$  nA) **d**) STM image of randomly fused precursor molecules. ( $V_B = +1.0$  V,  $I_T = 0.5$  nA) **e**) High resolution image showing individual precursor geometries. Marked in red is a small graphene flake. ( $V_B = +1.0$  V,  $I_T = 0.1$  nA) **f**) Chemical structures of the different isomeric configurations of the T30-triangle.

Figure 5.20 **a** shows an image of the surface after the first annealing step at  $T \approx 250$  °C. Some cyclized precursor molecules are visible, being adsorbed at the fcc areas of the herringbone reconstruction, similar to C30-triangles. The image quality is greatly reduced by mobile molecules being present at the surface, which results in a streaky appearance of the substrate. Moving over the sample, this unsteady tunneling junction did not allow for any reasonable imaging of the molecules, which is why the sample was annealed again at  $T \approx 450$  °C. This turned out to resolve

the issue and the sample was now full of covalently connected T30-triangles.

In figure 5.20 **b** and **c** two STM images of differently covered sample regions are shown. In **b** the precursor molecules start to form randomly connected structures with no preferred orientation. Similar to the case of C30-triangles, at such elevated annealing temperatures the surface template effect is overcome and once the molecules form larger connected structures, they do not diffuse around on the surface anymore. In more densely covered regions, like it is shown in **c**, the molecules formed some linear chains, which are structurally similar to T30-GNRs. However, in this STM image it can already be seen that the shape of the T30-triangles is not equal and that there in fact exist three distinct configurations of the molecule.

These isomeric molecular configurations are shown in **f** and make it immediately clear why there are just a few linear chains present. Depending on the connection angle between individual T30-precursor molecules during the solution synthesis only one of the three species exists with a parallel edge configuration from which T30-GNRs can be formed. Since the three structures are isomeric, they can not be distinguished during the usual purification methods, which are based on the molecular mass of individual reaction components.

This is also visible in the high resolution images **d** and **e**, where the individual shape of each molecule can be recognized. However, no significant tendency towards the formation T30-GNRs is observed but rather a variety of randomly connected molecules are present on the surface. In some locations, individual phenyl rings might have closed the pores integrated in the T30-triangles, forming small pieces of graphene. Such a piece is marked with a red circle in **e**. Due to the molecular powder including three different molecules, this sample only shows randomly connected nanostructures. If it would be possible to separate these three species from another, the use of only the one with parallel edges would most certainly lead to a similar behavior as it was observed for C30-triangles.

### 5.2.3 Conclusion and outlook

The experiments shown here revealed major differences between the coupling reactions of T30- and C30-precursor molecules on-surface and in solution. It could be shown that the different reaction paths lead to the formation of different reaction products. The third degree of freedom available during the solution synthesis allows the precursors to form trimeric structures instead of quasi one dimensional polymer chains. Furthermore, the solution based synthesis can lead to the formation of isomeric molecules that are structurally different. In the case of T30-triangles, this could be revealed by STM images, showing that there are indeed three different molecular structures present in the solution synthesized powder.

Placing T30- and C30-triangles on a clean Au(111) surface showed that the surface reconstruction has a strong template effect, with both molecules being adsorbed predominantly in the fcc regions of the herringbone pattern. For C30-triangles, a repulsive interaction between individual molecules was observed, which is based on a charge pillow effect.

During the on-surface experiments, it also became apparent that the dehydrogenation temperatures of both T30- and C30-triangles seem to be greatly reduced in comparison to the T30- and C30-precursor molecules. All molecules appeared fully cyclized in the STM images already at temperatures below  $T = 250$  °C.

When trying to promote further coupling reactions, it was surprisingly found that C30-triangle molecules form quasi one-dimensional C30-GNRs. This coupling reaction has to be based on a symmetry breaking mechanism that happens to the repulsive charge pillow upon dimer formation. For T30-triangles, no such effect could be observed. However, based on the fact that for these molecules not just one but three different molecular structures were present on the sample this effect might also just be not as significant as for C30-triangles. One of the present species, showing a parallel edge configuration, however did result in short T30-GNR segments.

These findings are currently under publication, with the focus on the differences between halogene coordinated coupling on surfaces and in solution. A possible next step with molecules of this kind would be to use different halogene atoms at varied sites on the molecules to hierarchically control the formation of porous graphene on the surface. Also, a explicit theoretical model is still needed to support the symmetry breaking argument for the coupling of C30-triangles.

## 5.3 GNR Heterojunctions

It has already been mentioned in section 3.3.3 that linear combinations of more than one GNR species, called GNR heterojunctions, are fascinating research objects. The possibility to combine semiconductor materials with different bandgap widths allows for the direct construction of p-n-junctions on the surface. Thereby it is not only possible to construct FET devices with atomic precision, but also other interesting phenomena like the emergence of topological states inside those junctions can occur. GNR heterojunctions are formed on the surface by self-assembly of the precursor molecules into polymer chains and subsequent postannealing for cyclodehydrogenation. Providing two kinds of precursor molecules will thereby result in a more or less random sequence of both in the synthesized hetero-GNRs. Usually, the individual molecules are deposited onto the surface via thermal evaporation. However, since a new technique of diffusion controlled sample preparation has been developed, which is described in section 4.7.2, this method is going to be used here. With such a versatile approach it is possible to test a variety precursor combinations to create different heterojunction systems.

Using the DCT application with a 1:1 molar mixture of precursor molecules instead of just one single species proved to be a promising tool to create GNR heterojunctions with varying composition. The different diffusion constants of the molecules on the surface result in a varying ratio of species 1 and 2 depending on the distance from the contact site. The GNRs synthesized within the scope of this work, provide a variety of possibilities to form novel GNR heterojunctions, two of which will be discussed in this section. Since the sample preparation is similar for all the following experiments, it will be discussed once in detail here.

The 1:1 molar mixture was prepared using a precision balance (Mettler, AE160), and was afterwards deposited onto a clean Au(111) surface via the DCT method described in section 4.4.3. Thermal activation at  $T = 120\text{ }^{\circ}\text{C}$  then promotes diffusion of the individual molecules over the surface. This temperature was usually kept constant for about 30 min and then the temperature was rapidly increased to  $T = 250\text{ }^{\circ}\text{C}$  and afterwards to  $T = 450\text{ }^{\circ}\text{C}$  for polymerization and cyclodehydrogenation. Each sample was investigated by acquiring STM images in different distances from the contact area to figure out if the coverage is too high or too low. After finding the sweet spot where desirable heterojunctions are located, the characterization of these with the help of  $dI/dV$  point spectroscopy and  $dI/dV$  mapping followed.

### 5.3.1 C90-GNR/9-AGNR Heterojunctions

In this section, the results of C90-GNR/9-AGNR heterojunctions will be presented. Based on the theoretical predictions of Taqieddin and Aluru,<sup>[200]</sup> the plan was to verify their results on a real system. When they studied heterostructures of C90-GNRs and 9-AGNRs using first principle calculations, not only did they find that the length of each GNR segment is of utmost importance for the resulting bandgap of the combined structure, but also that a topological interface state emerges at the junction. Especially this theoretically predicted interface state remained to be tested experimentally, which is why C90-GNR/9-AGNR heterojunctions were chosen. Since the two individual precursor molecules were frequently used in the past and the experimental synthesis parameters were very well known due to the experiments presented in section 5.1.1 and section 5.1.2, they were excellently suited as a test system.

For the synthesis of the heterostructures, the diffusion based sample preparation technique, described in section 4.7.2 was used with a 1:1 molar mixture of C90- and 9-A-precursor molecules. As expected, it was found that the surface coverage did turn out differently than for the deposition of just one molecular species. The different diffusion constants of the precursor molecules led not only to a decreasing surface coverage over the crystal surface, but also to a varying precursor ratio in the formed heterojunctions. Depending on the distance from the stamping site, this precursor composition could be mapped out by simply moving the tip over the sample surface with the coarse motion drive. For the investigation the LT-STM was used to take images in varying distances across the sample, which were then analyzed for their surface coverage.

The inhomogeneous coverage over the whole sample surface was mapped out too, and the findings have already been shown in figure 4.11. The images there clearly show that in areas closer to the contact site, solely C90-GNRs were found with large adsorbates, most likely unreacted 9-A-precursor molecules, lying on top of them. On the opposite side of the surface, the surface showed very little coverage, with mostly clean substrate areas and just a few single 9-AGNRs present. No C90-GNRs were found on that side of the crystal, clearly showing that the diffusion constant of 9-A-precursors is larger than that of C90-precursors. Having a closer look into the region of interest on the sample surface, where heterojunctions of different compositions were located, resulted in the STM images shown in figure 5.21. These junctions were found in a distance of 2.5 mm to 3.5 mm from the DCT contact area with the distance increasing from **a** to **d**. The exact sequence of precursor molecules could be determined from the STM images, since the spatial resolution is good enough to even distinguish individual phenyl rings.

The number of C90- and 9-A-precursors for each junction was determined by comparing the STM image with structural models of the molecules. The structural formula of the corresponding polymer of each junction is given below each image, with the individual precursor molecules colored respectively. It is clear to see that the number of C90-precursor molecules decreases

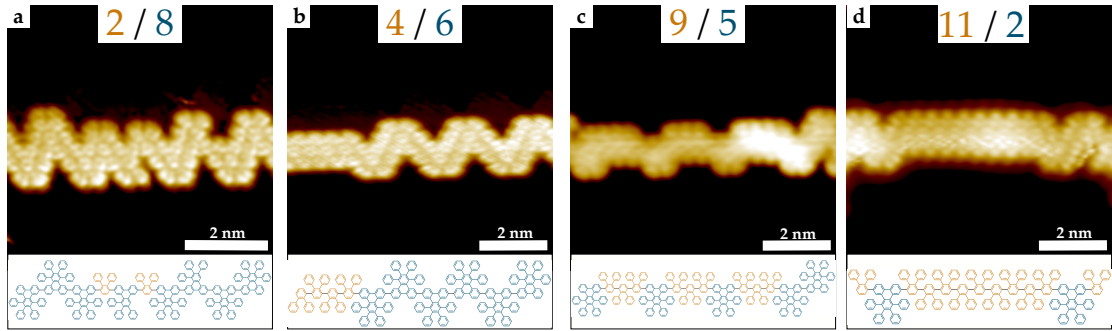


Figure 5.21: STM images of differently composed C90-GNR/9-AGNR heterojunctions. The structural formula under each images shows the polymer of each junction respectively. **a)**  $I_T = 0.5$  nA and  $V_B = -2.0$  V. **b)**  $I_T = 0.5$  nA and  $V_B = -2.0$  V. **c)**  $I_T = 1$  nA and  $V_B = -2.0$  V. **d)**  $I_T = 1$  nA and  $V_B = -1.8$  V

while the number of 9-A-precursors increases from **a** to **d**, meaning from close to the contact site to the opposite side of the crystal surface. This is in good agreement with the discovery that C90-precursor molecules most likely have a smaller diffusion coefficient on Au(111) and are therefore only not found on the opposing side of the surface. Taking a closer look at each junction, the only pristine C90-GNR/9-AGNR heterojunction is shown in **b**. All the other junctions are sequences of the different precursors, instead of a pristine 9-AGNR connected to a C90-GNR. Such junctions are the desired, since they allow us to test the hypothesis of a potential interfacial state. The other junctions show that an alternating sequence of C90- and 9-A-precursor molecules results in a new structure which can be described as a reduced chevron GNR. In comparison to a C90-GNR it is only 12 instead of 15 carbon atoms wide but also shows the distinct chevron like shape. This hybrid structure was regularly formed during experiments.

To investigate the electronic properties of a pristine C90-GNR/9-AGNR heterojunction  $dI/dV$  mapping was used to determine the exact energetic and spatial location of the postulated interfacial state. As it turned out, performing spectroscopic measurements on these samples is challenging because a lot of mobile adsorbates prohibit stable measurement conditions over longer time periods. Several annealing steps could unfortunately not resolve this issue, but instead led to the disintegration of the structures if the temperature was chosen slightly too high.

In figure 5.22 **a - d**,  $dI/dV$  maps of select C90-GNR/9-AGNR heterojunctions are shown. The junction shown in **a - c** consists of a short 9-AGNR segment which is connected to a C90-GNR segment. Even though these segments are rather short, it can be seen in the  $dI/dV$  maps that they show characteristic localized electronic states nonetheless. The energies of these states are in good agreement with previously published results,<sup>[136,143]</sup> proving a sufficient and comparable tip configuration during these measurements. At  $E = +0.65$  eV, where neither C90-GNRs nor 9-AGNRs have significant electronic states visible in the  $dI/dV$  signal, a highly local feature of

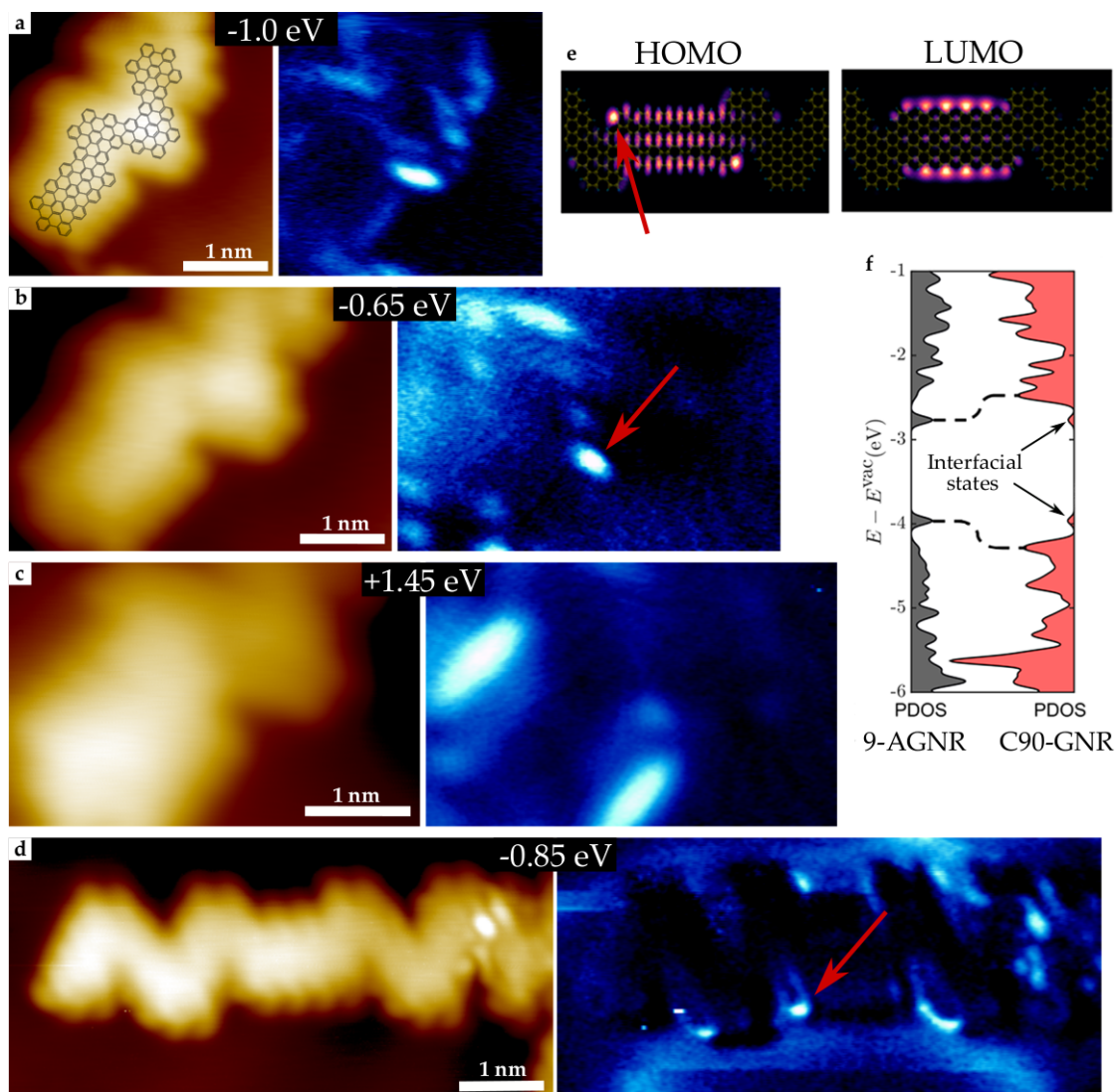


Figure 5.22: **a) - c)**  $dI/dV$  maps of a C90-GNR/9-AGNR heterojunction at different energies. A structural model was superimposed and the interfacial state is marked with a red arrow in **b**. ( $I_T = 0.1$  nA,  $V_{\text{mod}} = 50$  mV,  $f_{\text{mod}} = 865$  Hz) **d)**  $dI/dV$  map of a C90-GNR/9-AGNR/C90-GNR junction where interfacial state is again marked in red. ( $I_T = 0.1$  nA,  $V_{\text{mod}} = 60$  mV,  $f_{\text{mod}} = 925$  Hz) **e)** Density functional theory calculation of the spatial distribution of HOMO and LUMO on C90-GNR/9-AGNR/C90-GNR heterojunction. From Ref. [200]. **f)** Projected density of states for a C90-GNR/9-AGNR/C90-GNR heterojunction. From Ref. [200].

high intensity appears right at the junction. This feature repeatedly appeared in the measurements and was also observed on other junctions, such as the one shown in **d**. Here the energetic location is slightly shifted towards lower energies at  $E = +0.85$  eV, which could be addressed to the structural difference compared to the heterojunction shown in **a**. However, this electronic state is

always located right at the concave edge of the junction, directly at the location of the outermost carbon atom of the 9-AGNR segment. This is in perfect agreement with the postulated position of the interfacial state of Taqieddin and Aluru.

Their DFT calculations are shown in figure 5.22 **e** and **f**. The spatial distribution of the frontier energy levels (i.e., the highest occupied molecular orbital (HOMO) and the lowest unoccupied molecular orbital (LUMO)) are shown in **e** where it becomes apparent, that the postulated location of the state precisely matches the results presented here. In addition, **f** shows the projected density of states for a 9-AGNR/C90-GNR heterojunction, in which the interfacial state is located inside the bandgap, effectively modifying the bandgap width of the junction. This is hard to verify with the existing experimental data from the experiments and remains to be tested in the future using  $dI/dV$  point spectroscopy.

These experiments prove the existence of the theoretically predicted topological interfacial state in C90-GNR/9-AGNR heterojunctions. By applying a newly developed sample preparation technique to a previously unknown molecular system, it was possible to verify the theoretical postulations. This case shows, that theoretical investigations of such nanostructures are absolutely necessary and can help to identify suitable systems without the need to conduct time-consuming surface science experiments.

### 5.3.2 C90-/T90-GNR Heterojunctions

As a second example for GNR heterojunction synthesis, C90-/T90-GNR heterojunctions will be used. The motivation behind these experiments was the exceptional growth characteristics of T90-GNRs in combination with the different bandgap widths of both individual GNRs. The hope was to create a stabilizing effect due to the use of T90-precursor molecules and thereby create long hetero-GNRs usable for the incorporation in future electronic devices.

Due to the structural similarity of both precursor molecules, the resulting structures should show a straight backbone with truncated and non-truncated chevron like edge structures. Such heterojunctions out of structurally related molecules have proved to result in interesting electronic properties in the past. [133,135,136]

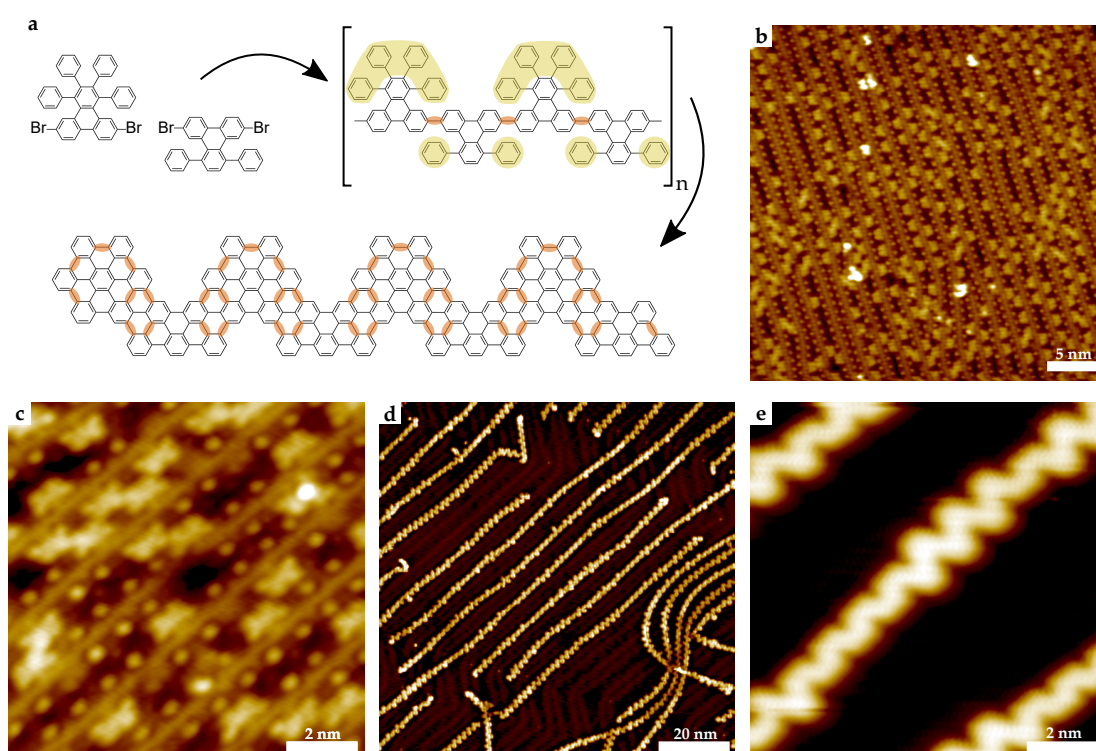


Figure 5.23: **a)** On-surface synthesis route for C90-/T90-GNR heterojunctions. Newly formed covalent bonds are colored in orange and yellow molecule parts resemble the bright features in **b** and **c**. **b)** STM image of aligned C90-/T90-polymer chains. ( $V_B = +1.0$  V,  $I_T = 0.2$  nA) **c)** Detailed view of aligned C90-/T90-polymer chains. The bright features resemble non-planar phenyl rings of each precursor molecule. ( $V_B = +1.0$  V,  $I_T = 0.3$  nA) **d)** STM image of extraordinarily long C90-/T90-GNRs. ( $V_B = +1.0$  V,  $I_T = 1.0$  nA) **e)** Image of a perfect Heterojunction consisting of pristine C90-GNR and T90-GNR segments. ( $V_B = +1.5$  V,  $I_T = 1.0$  nA)

Figure 5.23 shows the resulting structures after stamping a 1:1 molar precursor mix of C90-

and T90-precursor molecules onto the surface. In **a** the individual reaction steps are shown for an exemplary alternating configuration of precursors. The newly formed covalent bonds after polymerization and cyclodehydrogenation are colored in orange and in the polymer stage, non-planar phenyl rings are highlighted in yellow.

As can be seen in figure 5.23 **b** and **c** the formed polymer chains are clearly recognizable because of their distinct visual appearance. The backbone of each chain appears as a straight line, which is decorated by bright features. These parts resemble the out of plane rotated phenyl rings. Depending on the number of those rings present on each precursor molecule, differently shaped features are visible. Each T90-precursor creates two bright lobes, as it has already been observed in figure 5.2, and each C90-precursor molecule resulting in a trapezoidal feature, consisting of four individual tilted phenyl rings. This distinct appearance makes it possible to uniquely identify every single precursor molecule incorporated in the chain.

Another phenomenon visible in figure 5.23 **b** is that the chains show perfect parallel alignment in areas with high coverage. This is rather surprising, since the edge structure of the heteroribbons is not uniform. In the upper left corner of **c** two neighboring chains are shown consisting of mostly C90-GNR precursors. From this part one can see that the distance between adjacent chains is determined by the C90-GNR parts. The phenyl rings of the T90-precursor molecules have a larger distance to neighboring chains than in the case of pristine T90-polymers and can therefore only contribute little to the attractive interaction. This is a surprising result, since such a tendency towards parallel alignment was not observed for C90-GNRs.

A less densely covered area of the surface is shown in Figure 5.23 **d**. The present hetero-GNRs are already fully cyclized after the second annealing step and are nicely aligned with the herringbone reconstruction. At a first glance, the GNRs seem to consist of randomly arranged C90- and T90-precursors but on closer inspection several larger segments of pristine C90-/T90-GNR heterojunctions, like the one shown in **e**, can be found. The length of the GNRs is exceptional, with the longest chains exceeding 150 nm. An example can be seen in **d**, reaching from the bottom left to the top right corner of the image. On the left side of that STM image, some of the GNRs seem to be bent around 90° and overlapping each other. During the on-surface synthesis, the GNRs experience not external forces that could result in such a deformation. Since it is well known that GNRs can be manipulated with the STM tip,<sup>[201–203]</sup> it is likely that such a manipulation happened here on accident. Due to a high setpoint while scanning, the GNRs must have gotten attached to the tip at some point and then dragged in the scan direction. This also explains why the ends of the GNRs are displaced horizontally, in line with the scanning motion of the STM tip.

The pristine heterojunction in **e** again shows the truncated nature of T90-GNRs with respect to C90-GNRs, where two phenyl rings are missing on each precursor, making the T90-GNR 3 carbon atom rows more narrow. Since such junctions are frequently found on this sample,

enough structures were present to investigate the electronic properties using STS.  $dI/dV$  point spectroscopy measurements along the heterojunction were therefore performed to see how the band structure develops from one side of the junction to the other.

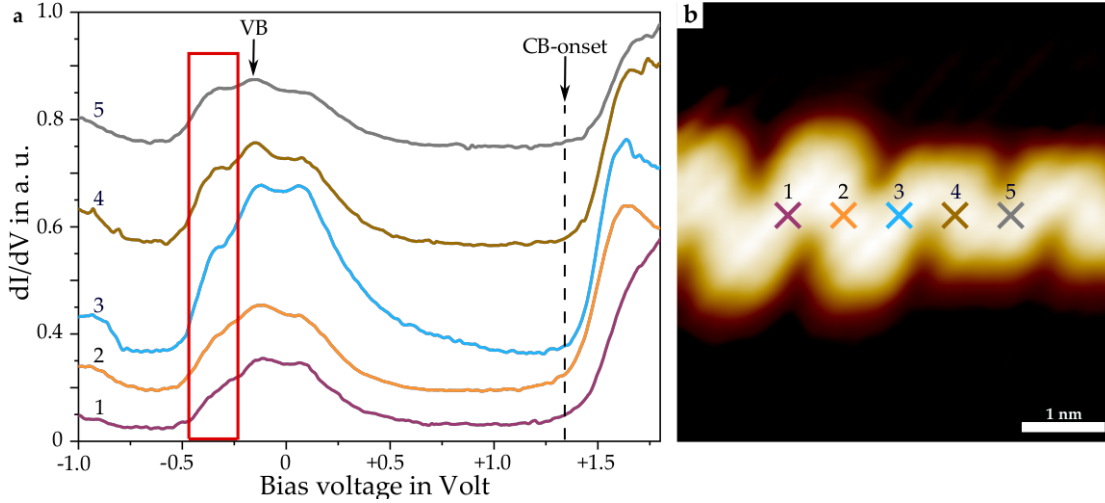


Figure 5.24: **a)**  $dI/dV$  point spectra taken across a C90-/T90-GNR heterojunction. The measurement locations are marked with colored crosses in **b)**. Marked in red is a peak that evolves along the junction and the dashed line identifies the CB-onset. All spectra measured with a setpoint of  $I_T = 0.1$  nA, with a modulation voltage of  $V_{\text{mod}} = 30$  mV at  $f_{\text{mod}} = 859$  Hertz. **b)** STM image of a pristine heterojunction. ( $V_B = +1.5$  V,  $I_T = 1.0$  nA)

Figure 5.24 **a)** shows the  $dI/dV$  point spectra measured at the marked locations in **b)**. Starting from the pristine C90-GNR segment on the left five equidistant points were chosen across the heterojunction. All spectra show a clear bandgap spanning from  $E \approx -0.2$  eV to  $E \approx 1.3$  eV. It can be seen, that the location of the CB-onset, marked by the black dashed line, does not significantly change across the heterojunction. In the area marked by the red square however, a peak is emerging going from the C90- to the T90-GNR side. While it is not present in the first spectrum, it increases in intensity and is observable as a clear peak in spectrum 5, being located at the T90-GNR segment. Comparing the spectra to the ones for pristine C90- and T90-GNRs shown in figure 5.3 and figure 5.8 it can be seen that this peak is indeed an electronic feature of T90-GNRs, also appearing in the measurements shown in figure 5.8. However, the positions of the peaks around the Fermi energy and the energetic location of the CB-edge are similar to the values determined for pristine C90-GNRs.

It is therefore concluded that the bandgap width across the junction is predominantly defined by the C90-GNR segment with the VB and CB edge peaks being present in all spectrum across the junction, while the shifted location of the CB-edge for T90-GNRs could not be observed. The fact that no pristine T90-GNR spectrum was observed is due to the fact that the length of

that segment was simply not large enough. These spectra also hint that there are no topological interfacial states present, since no novel electronic states that could not be assigned to either of the GNRs were observed. Usually, such electronic states emerge at the junction between two different GNR segments, where topological effects can lead to the formation of interfacial electronic states.<sup>[143,204]</sup> To further verify that there are indeed not localized states present at any part of the junction,  $dI/dV$  mapping to reveal the spacial distribution of electronic states.

In figure 5.25 the different  $dI/dV$  maps of the C90-/T90-GNR heterojunctions are shown with the respective energy of each map given above each pair of images. Inside the valence band, the characteristic GNR states dominate the images with the maps at  $E = -1.7$  eV,  $E = -1.5$  eV and  $E = -1.1$  eV showing localized edge states in both parts of the junction. At  $-1.3$  eV there is solely the armchair state of the T90-GNR present. Moving closer to the VB edge position, at  $E = -0.9$  eV and  $E = -0.7$  eV the chevron edge state of the C90-GNR is predominant. Unsurprisingly, the maps at  $E = -0.2$  eV and  $E = +0.4$  eV do again show strong signal of the substrate surface state. The superposition of both signals makes it challenging to separate the GNR states from the surface state.

At  $E = +1.3$  eV the overall signal amplitude of the  $dI/dV$  map is very low, reducing the signal-to-noise ratio in the map. The electronic states present here are very weak, but still represent the onset of the CB edge in the C90-GNR segment. At  $E = +1.5$  eV it is clear that the C90-GNR segment determines the conduction band edge. The strong signal amplitude coming from that part of the junction leaves no doubt that this energy is already located inside the CB. For a complete analysis of the heterojunction more  $dI/dV$  maps were recorded at other energies inside the bandgap. These maps are given in section 7.3.

None of these maps did show any signs of topological states in proximity of the junction or any extraordinary electronic effects. This leaves us with the conclusion that C90-/T90-GNR heterojunctions do indeed not possess any topological interfacial states. However, what these measurements show is that the overall bandgap of the hetero-GNR is predominantly defined by the C90-GNR segments. It is therefore no wonder that the  $dI/dV$  point spectroscopy measurements showed a bandgap close to the one of pristine C90-GNRs.

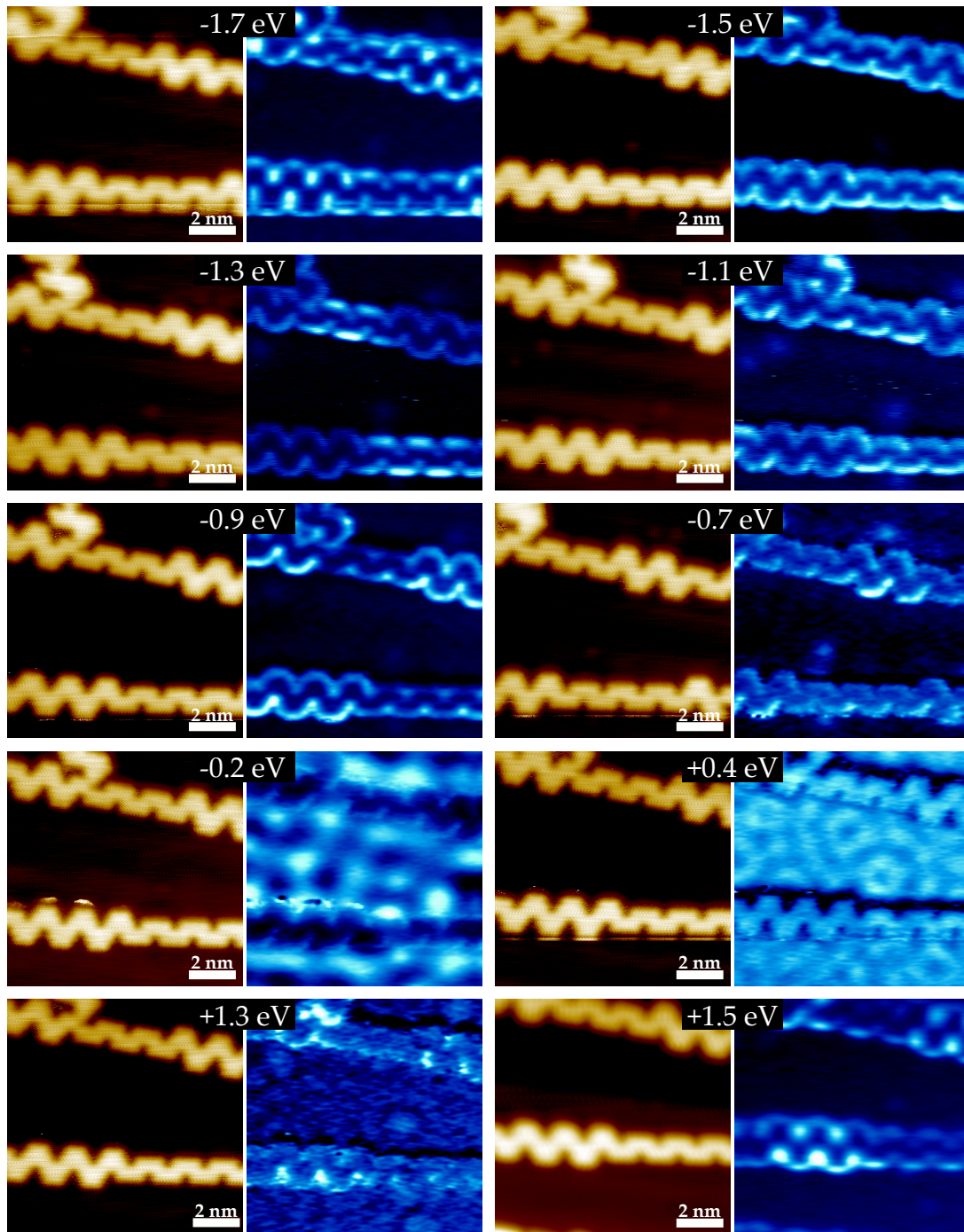


Figure 5.25:  $dI/dV$  maps of a C90-/T90-GNR heterojunction. The respective energies are given above each image. All maps were taken with a setpoint of  $I_T = 1.0$  nA and with a modulation voltage of  $V_{\text{mod}} = 20$  mV at  $f_{\text{mod}} = 4.371$  kHz.

### 5.3.3 Conclusion and outlook

From the previous sections, it can be concluded that the newly developed sample preparation method presents a versatile approach for the synthesis of GNR heterojunctions. The presented samples were all prepared using this approach, resulting in atomically precise GNR heterojunctions of varying precursor composition. It is therefore superior to the traditional approach of sample preparation through thermal evaporation of the molecular precursors. The sample quality also has to be highlighted here, since no major contaminations were found on the prepared samples.

The GNR heterojunctions presented here both show unique properties and have been synthesized experimentally for the first time. The first system, C90-GNR/9-AGNR heterojunctions, was chosen to verify theoretical predictions about localized electronic states in these junctions experimentally. Such localized states in GNR heterojunctions often emerge from topological effects at the interface. In this case, the existence of such an interfacial state could be verified. The  $dI/dV$  measurements presented clearly show a locally increased signal intensity at the expected location at the junction. With these maps, it was also possible to confirm the predicted straddling type band alignment of the hetero-GNR.

The second combination of precursor molecules resulted in the formation of T90-/C90-GNR heterojunctions. As it was expected, the T90-precursor molecules had a stabilizing effect on the chain growth, resulting in extraordinarily long hetero-GNRs. Attractive interactions between the chains due to the rotated phenyl rings of C90-precursor molecules furthermore led to a parallel alignment of those chains, resting preferably in the fcc channels of the herringbone reconstruction. With regard to the subsequent use of these in electronic devices, such an alignment is extremely beneficial. In hindsight to the electronic properties of these junctions, it could be shown that the bandgap of the combined system is determined by the C90-GNR segment. This was further underlined by the measured  $dI/dV$  maps, that showed greatly increased signal on these parts of the junction inside the valence and conduction band.

Future experiments are planned utilizing the simplicity of the diffusion based sample preparation technique for the synthesis of other hetero-GNR systems. Especially the incorporation of porous GNR segments into heterojunctions is interesting since no such junctions with porous GNRs exist to date. The evolution of the pore state throughout the junction is thereby of particular interest. Experiments regarding the manufacturing of FET devices out of T90-/C90 hetero GNRs are already planned in close collaboration with the group of Prof. Sinitskii.

## 5.4 Porous nanographenes (PNG)

The following section will revolve around the synthesis of porous nanographenes out of individual GNRs. The idea for this project emerged based on the observations presented in section 5.1 that at sufficiently high coverages, some GNRs tend to form parallelly aligned islands. As it has been previously shown, GNRs that are in close proximity of each other can be fused together via a second dehydrogenation process.<sup>[137,205,206]</sup> Combining these two pieces of information the plan was to laterally fuse parallelly aligned GNRs together, to create two-dimensional sheets of nanographene.

Such nanographene sheets have already been synthesized in the past, however, the lack of a significant bandgap prohibits the use in any electronic applications. In the case of the GNRs presented here however, a lateral combination will result in the formation of nanopores either by creating the pores at the seam of two adjacent ribbons or by simply using porous GNRs right away. Few studies are known for such porous nanographenes, however, since the pores do alter the electronic properties of individual GNRs, they are suspected to open up a bandgap in otherwise semimetallic graphene sheets. In this study, a complete spectroscopic characterization of different PNGs will reveal the nanopores do indeed determine the electronic properties. With the use of  $dI/dV$  point spectroscopy and  $dI/dV$  mapping, the bandgap of structures of different widths will be determined, exposing a surprising connection.

For these experiments, samples were prepared with T90-, T30- and C30-GNRs with the focus on maximizing the alignment between individual chains. The synthesis parameters were therefore tuned carefully, resulting in samples with large areas of aligned GNRs. As it is usually the case, long annealing times in combination with slow increases in temperature during synthesis steps seemed to do the trick, since the molecules have enough time to relax into the most favorable positions. Being left with a suitable sample, a last annealing step was used to promote interribbon coupling and the formation of PNGs.

### 5.4.1 C30-PNGs

This section will start off with the presentation of the results for the synthesis of porous nanographenes from C30-GNRs. As shown in section 5.1.5 the C30-precursor molecules form rather short, porous graphene nanoribbons with a chevron like edge structure. It has already been observed that these shorter chains also result in much smaller areas of parallelly aligned C30-GNRs. However, this system can be used as an example to underline the importance of experimental parameters during the synthesis. In figure 5.26 six STM images of samples covered in C30-PNGs are shown, synthesized with different annealing strategies.

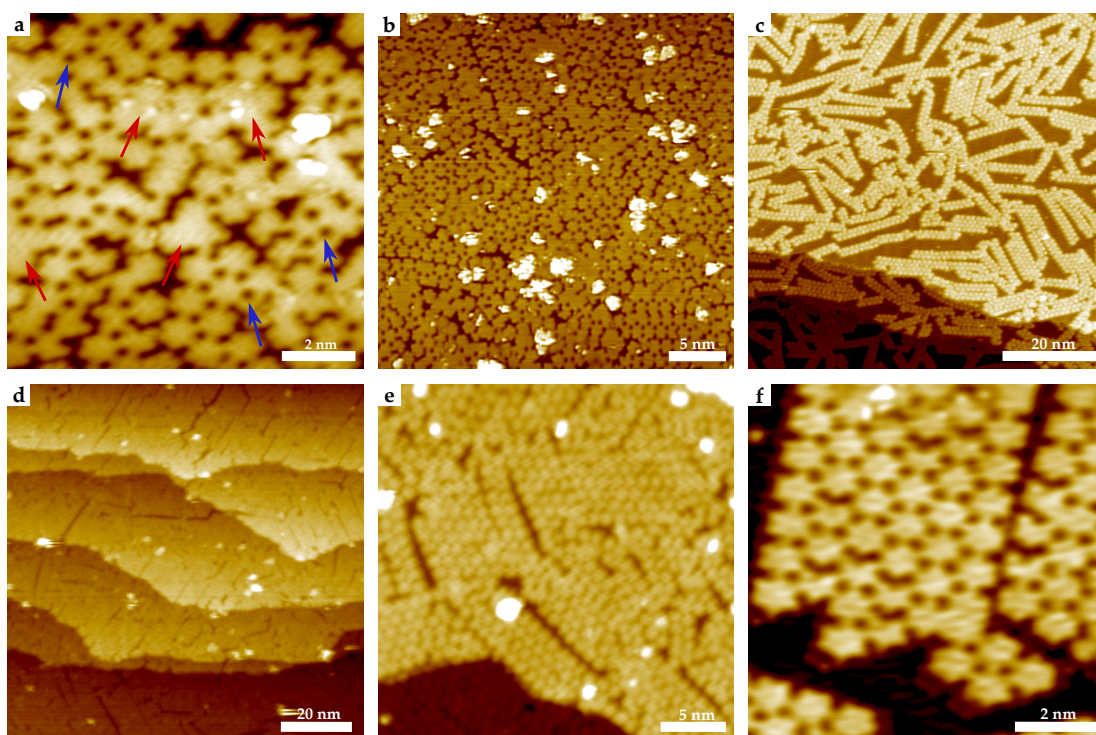


Figure 5.26: **a - c**) STM images of C30-PNGs synthesized with a fast annealing process. (**a**:  $V_B = +1.0$  V,  $I_T = 1.0$  nA, **b**:  $V_B = +0.8$  V,  $I_T = 0.5$  nA, **c**:  $V_B = +0.8$  V,  $I_T = 0.5$  nA) **d - f**) STM images of C30-PNGs synthesized under optimized growth conditions. (**d**:  $V_B = +1.0$  V,  $I_T = 1.0$  nA, **e**:  $V_B = +1.0$  V,  $I_T = 1.0$  nA, **f**:  $V_B = +1.0$  V,  $I_T = 1.0$  nA)

In **a** and **b** the sample was rapidly heated up to  $T = 500$  °C directly after deposition of the molecular powder. The first observation that has to be pointed out here is that, due to the drastic increase in temperature, the diffusive motion and thereby the spread of molecules on the crystal surface is greatly diminished. Compared to other samples prepared with this technique but longer annealing times, reacted precursor molecules were only found in close proximity to the direct contact site, meaning that the tip had to be located very close to that area to observe the molecules.

This is also the reason why there are visible bright adsorbates present on top of the monolayer coverage in the images.

In both images, no GNR-like chains are visible, but individual C30-precursor molecules can be distinguished by their distinct hexagonal shape. It is concluded that due to the rapid temperature increase, only some of the precursor molecules formed polymer chains and subsequent GNRs, while most molecules remained separate. Upon dehydrogenation, covalent bonds are formed between all present structures, leaving us with a sample of randomly connected hexagonal precursors. This behavior is similar to the results of Teeter et al., who reported that the non-brominated analogue of the C30-precursor molecule, hexaphenylbenzene, forms random connections between adjacent molecules when deposited on Cu(111) and postannealed to  $T = 450$  K.<sup>[207]</sup> The C30-precursor molecules used here behave similarly, since C-Br- as well as C-H-bonds break up at the same time, leaving fully radicalized molecules on the surface that form covalent bonds at random sites.

One major difference in the resulting structures has to be pointed out, since it is important if the precursor molecules are connected at the edge locations or on their sides. In the study of Teeter et al., the molecules connected on the edges due to a closely packed configuration prior to the annealing step. In the case shown here, the molecules are oriented randomly, thereby also creating covalent bonds at random sites. When two precursors connect side to side, not one but three covalent bonds are formed and the resulting structure is fully graphenic. Such locations are marked in **c** with red arrows, where two or more precursor molecules are connected. The missing nanopores, marked in blue, make it obvious, that the molecules are not connected on the edge positions.

A surface area with a coverage of about 0.8 ML, where the C30-PNGs are oriented randomly, is shown in Figure 5.26 **c**. Besides the fact that there are a variety of random connections between individual C30-GNRs and already fused structures, it is also visible, that only a few C30-GNRs seem to be parallelly aligned. Since such irregular structures are undesirable, areas closer to the DCT site with higher surface coverages were investigated. Shown in **d** and **e** are images of such surface areas, where the molecular coverage is close to one monolayer.

Here, the individual C30-GNRs are originally aligned. Further annealing now results in the formation of covalent bonds between the neighboring chains, creating porous nanographenes. The large scale image in **d** shows that the PNG structures extend over several step edges and cover large areas of the surface. The formation of such PNGs however requires at least some lateral movement of the individual GNRs. As the covalent bonds are formed, the distance between adjacent chains is decreased. Calculating the distances between adjacent C30-GNRs from figure 5.14 **c**, results in a average gap value of 0.25 nm, which is reduced to quasi zero as PNGs are formed. This leads to the formation of small gaps between the PNGs, that can be observed in figure 5.26 **d** and **e**. As neither GNRs nor PNGs can close these gaps due to the hindered diffusive motion, the width of

PNG structures is limited. Using this method, no PNGs containing more than six individual were observed, since then the distances to the nearest neighbors simply become too large.

In **e** and **f** two zoomed in STM images are shown which reveal the actual structure of the C30-PNGs. In **e** it can be seen that the individual hexagonal building blocks are ordered in a perfect hexagonal lattice, of course due to the connection angles between the molecules. Side to side connections as observed in **c** are not visible here. As postulated, the gaps between the C30-PNGs seem to reach a certain size until the distances can not be overcome anymore, stopping lateral growth of the PNGs. In Figure 5.26 **f** a molecularly resolved PNG strip synthesized out of three individual C30-GNRs is shown. The periodically aligned pores are clearly visible as dark spots between individual hexagonal precursor structures. However, it is also visible that the structure contains a lot of defects, similar to the observations from C30-GNRs.

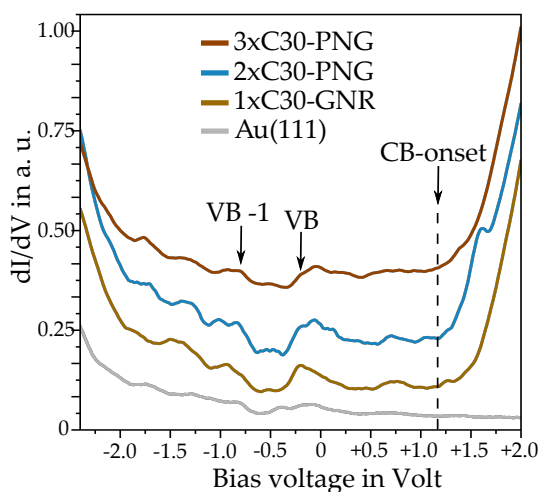


Figure 5.27:  $dI/dV$  point spectra taken on different C30-PNGs of different width and on the clean Au substrate. The VB-1 and VB edge positions and the CB onset are marked accordingly. All spectra measured with a setpoint of  $I_T = 0.1$  nA, with a modulation voltage of  $V_{\text{mod}} = 30$  mV at  $f_{\text{mod}} = 859$  Hertz.

the opening of a bandgap in porous graphenic flakes. To test this hypothesis,  $dI/dV$  point spectroscopy was used to determine the bandgap width of C30-PNGs.

In figure 5.27, four  $dI/dV$  spectra are shown. The first one marks the reference spectrum measured on clean Au(111) substrate to verify the tip configuration. The other three are again averages over several individual spectra, measured on C30-PNG structures of different widths. The nomenclature here is such that  $N \times \text{C30-PNG}$  refers to a PNG of  $N$  laterally fused C30-GNRs. It is obvious, that the C30-PNG spectra look very similar, with the VB-1 and VB edge as well

The shown structure has a width of 7.7 nm, or 54 rows of carbon atoms, which is one of the widest bottom-up synthesized graphenic structures to date. Due to the  $\pi$ - $\pi$  interactions in the polymer stage, the alignment of the chains is highly periodic, resulting in a perfectly periodic pattern of nanopores inside the structure after cyclization. As seen during the spectroscopic investigation of C30-GNRs, such pores alter the electronic properties of individual ribbons. It was therefore the logical next step to continue with a spectroscopic characterization of these structures. It is known, that pristine two-dimensional graphene sheets do not possess a significant bandgap.<sup>[208]</sup> However as described in section 3.3.5, several studies postulated

as the CB onset being clearly identifiable. One can see that the location of the VB-1 and VB edge appears to be constant throughout the spectra. Surprisingly, the location of the CB-onset also does not seem to change significantly with increasing width of the structures. With the VB edge located at  $E = -(0.22 \pm 0.03)$  eV and the CB-onset at  $E = +(1.18 \pm 0.10)$  eV,  $E_{\text{Gap}}$  was measured to be at least  $(1.40 \pm 0.13)$  eV. Which, especially for a 3xC30-PNG, is considerably bigger than expected for a pristine graphene sheet of similar width. This adds evidence to the theory that the nanopores play an important role regarding the bandgap width of the structure. The independence on the structural width also suggests that even for wider structures with the same pore configuration, the bandgap width would not change significantly.

In the Au(111) spectrum, a small additional peak is present close to the Fermi energy, which also appears in the C30-PNG spectra. It is therefore identified as a tip artefact and not attributed to the electronic structure of the C30-PNGs. Comparing the spectra here to the spectra shown in figure 5.15, one can see that they look qualitatively the same. Some notable differences in the shape of the CB edge are attributed to tip effects. Because of these differences, the CB-onset is marked here, while for the spectra of C30-GNRs, the CB edge location was marked. Even though the difference in shape of these features might seem surprising at first, the location of them is unaltered by the tip configuration.

### 5.4.2 T30-PNGs

In the next section, experiments regarding the synthesis of T30-PNGs will be presented. In comparison to C30-PNGs, the edge structure is different here, showing a purely armchair edge configuration. As it has been shown in section 5.1.4, the islands formed of parallelly aligned T30-polymers are considerably larger than for C30-polymers. With slight optimization measures of the on-surface synthesis process, this effect can be increased even more. The resulting arrays of T30-GNRs provide the perfect starting point to synthesize large nanographene sheets. Since the T30-GNRs already provide a nanoporous structure, the resulting nanographenes must have pores as well. However, contrary to the observations for C30-PNGs, in this case two configurations, in which the adjacent chains can be coupled, are possible. These different configuration types result in different pore patterns of the T30-PNGs. To provide a better understanding of the exact coupling sites, a schematic view is given in figure 5.28.

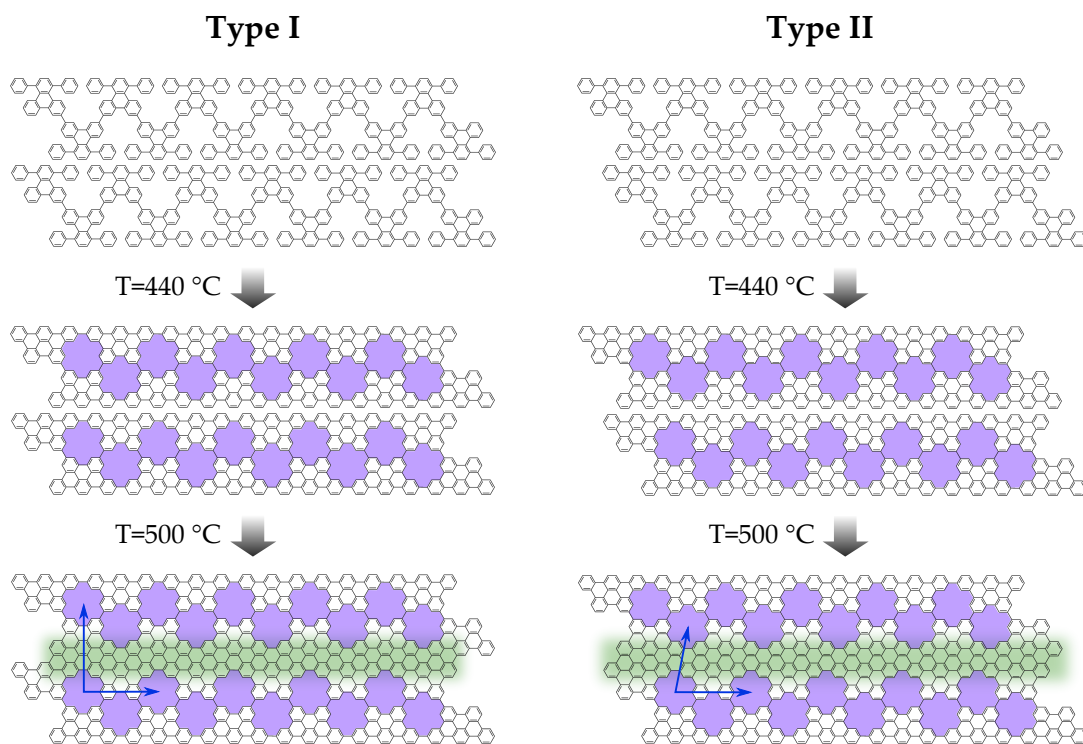


Figure 5.28: Reaction schemes for the on-surface synthesis of T30-PNGs with two alignment types. Type I aligning the pores of the neighboring chains and Type II, with a slightly shifted pore configuration. The pores of the fused structures are colored in purple, and green marks the resulting AGNR segment. Shown in blue are the unit cell vectors for the respective structures.

Figure 5.28 shows the two possible configurations in which neighboring chains can be connected. These two types of alignment are possible by shifting adjacent GNRs by the diameter of one

phenyl ring in the direction along the ribbon's axis. Due to the covalent bonding angle of the carbon lattice, only discrete shifting distances are allowed. Shifting the GNR by two times that distance again results in the Type I configuration.

The Type I configuration, shown on the left side of figure 5.28, results from an alternating placement of the rotated phenyl ring pairs of each polymer chain at the seam. This leads to the pores in the fused structure being aligned in the direction perpendicular to the ribbon's axis. The angle between the unit cell vectors, shown in at the bottom, in this case is 90 deg, resulting in a rectangular unit cell. In the Type II configuration, where an additional translation along the ribbon axis occurs. The formation of covalent C-C-bonds with a distinct angle of 120° creates a shift in the pore locations of about 0.4 nm. In this configuration, one of the unit cell vectors is tilted, creating an oblique unit cell.

The area marked in green represents a section of the PNG where no pores are incorporated. The covalent bonds formed at the seam thereby create a five carbon atom wide strip of pristine graphenic lattice, which can be regarded as a 5-AGNR. In the theoretical work of Baskin and Král, the bandgap width of porous nanographenes was calculated. What they found was that the bandgap is solely defined by the segments of armchair or zig-zag GNRs in between the pores.<sup>[162]</sup> By calculating the bandstructures of different porous nanocarbons, they showed that the electronic structure of the complete two-dimensional system can be determined by the graphenic strips, or parallel GNRs formed between the pores. In the case here, this would mean that the bandgap width of the T30-PNGs should be similar to the one of pristine 5-AGNRs. A hypothesis that will be tested through a spectroscopic characterization of T30-PNGs.

Before coming to the electronic characterization however, the synthesis of T30-PNGs will be discussed. In figure 5.29, STM images of the resulting T30-PNG structures are shown in areas of different surface coverage.

Figure 5.11 **a** shows an area with a coverage of about 0.8 ML after the second dehydrogenation step. It can be seen that the T30-GNRs are still separated on the surface and do not show a preferred orientation. Even at the step edge in the lower left corner of the image, no alignment is visible, even though there are several T30-GNRs parallelly attached to the edge of the upper terrace. Due to the lower coverage, the distances between individual chains in the polymer phase was simply too large for them to interact, leaving the cyclized T30-GNRs randomly oriented and isolated since no change in position happens once they are completely planarized. Moving closer to areas of higher coverage, the degree of alignment between the structures increases. In **b**, an exemplary STM image is shown in which individual T30-GNRs as well as already fused T30-PNGs are present. The red line divides the image into two domains with different ribbon orientations. The one on the left being vertical, while the one on the right side is rotated 60° hinting to an epitaxial alignment of T30-GNRs in densely covered surface areas.

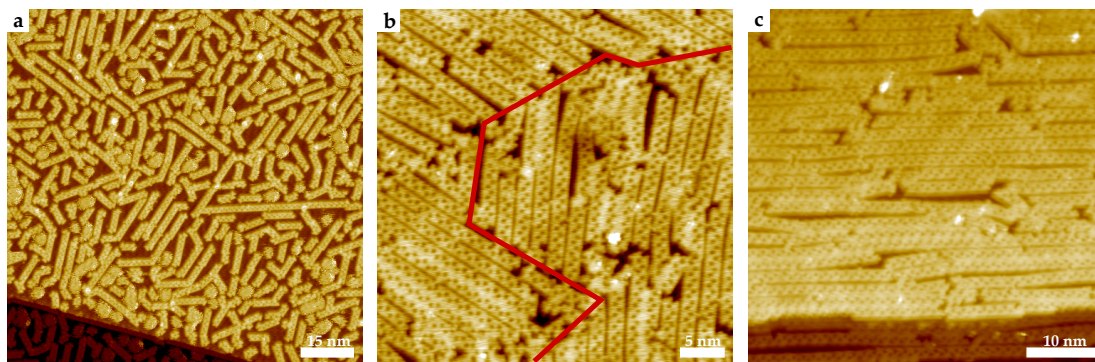


Figure 5.29: **a**) STM image of a T30-GNR sample after the second dehydrogenation step in an area with low surface coverage. Interribbon distances hinder the formation of T30-PNGs. ( $V_B = +1.0$  V,  $I_T = 0.6$  nA) **b**) STM image of a surface area with almost full coverage. Chains are not perfectly aligned but a considerable amount of PNGs is formed. ( $V_B = +1.0$  V,  $I_T = 1.0$  nA) **c**) Parallely aligned T30-PNGs near a step edge in an area with full surface coverage. ( $V_B = +1.0$  V,  $I_T = 1.0$  nA)

Another point that immediately catches the eye is that the fused T30-PNGs appear brighter at the seams than individual T30-GNRs. Does that mean that the formed 5-AGNR segment provides a locally increased conductivity and therefore appears brighter in the STM image than the rest of the ribbon? The  $dI/dV$  maps presented in figure 5.31 do not confirm this. It is therefore concluded that the epitaxial alignment of individual GNRs prior to the lateral fusing results in a mismatch of the atomic lattice T30-PNGs and the Au(111) surface. Such a mismatch might be leading to a slight buckling of the T30-PNGs at the seams, increasing their distance to the substrate locally.

Figure 5.28 c shows a fully covered region of the surface. It is clear to see that the GNRs and PNGs are all aligned parallelly to the edge and that due to this improved alignment longer PNGs are formed. Such stabilizing effects have already been discussed for the case of T90-GNRs and are desirable considering the fact that the resulting T30-PNGs are on average both longer and wider than on flat areas of the substrate. Upon closer inspection, it can be also seen that there is no preferred type of lateral alignment between the chains. The amount of T30-PNGs that are formed in a Type I fashion is equal to the amount of Type II T30-PNGs present.

Figure 5.30 a shows the result of the point spectroscopy experiments on T30-PNGs of different widths. Similarly to the case of C30-PNGs the interest here lied in the evolution of the bandgap depending on the structural width. Therefore, T30-PNGs consisting of a different number of T30-GNRs were investigated using  $dI/dV$  point spectra. The spectra were always taken right in the middle of each PNG structure, which of course leads to the tip being located above different parts of the T30-PNGs for every measurement. However, the spectra are still expected to show if the bandgap width shows any correspondence to the structural width. The measurement locations are marked exemplarily in the STM image shown in b with the respective colors. T30-PNGs in

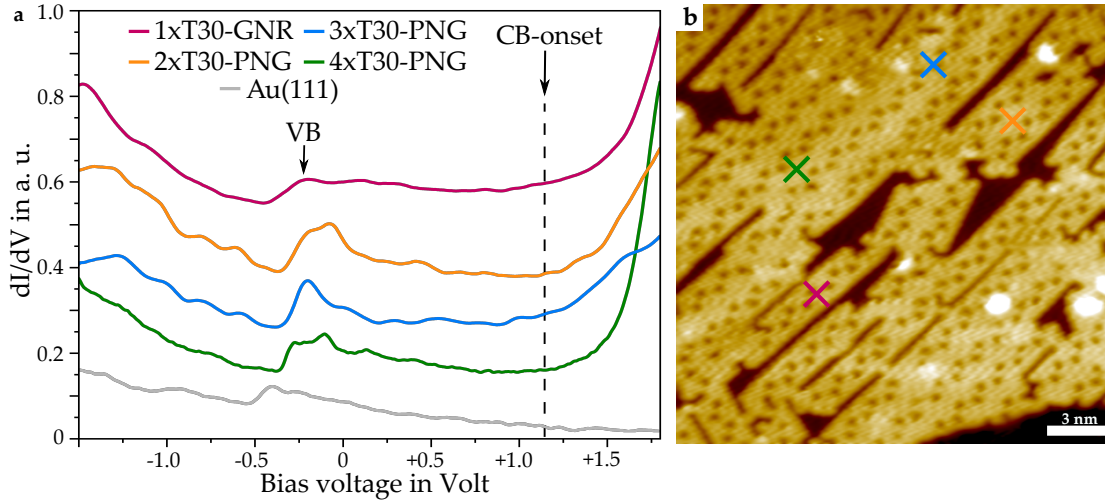


Figure 5.30: **a)**  $dI/dV$  point spectra of T30-PNGs of different width. The VB edge and CB-onset are marked accordingly. All spectra measured with a setpoint of  $I_T = 0.1$  nA, with a modulation voltage of  $V_{\text{mod}} = 30$  mV at  $f_{\text{mod}} = 859$  Hertz. **b)** STM images of T30-PNGs where measurement locations of the spectra are marked exemplarily. ( $V_B = +1.0$  V,  $I_T = 0.1$  nA)

this image consist of up to five individual T30-GNRs and, even though the parallel alignment is not ideal here, show considerable lengths of up to 20 nm.

Shown in gray in figure 5.30 **a)** is a spectrum of clean Au(111), also averaged over several individual point spectra. It shows that the tip configuration during measurements was stable, and no major artifacts in the spectra are created by the tip. Considering the overall shape of the T30-PNG spectra it can be seen that every spectrum shows a distinct peak, or peaks in the case of 2x- and 4x-T30-PNGs, at the usual VB edge location and a clear onset of the CB edge. The CB-onset was marked with a dashed line as a guide to the eye to show that its location does indeed not change significantly.

Looking specifically at the spectra of 2x and 4xT30-PNGs, it becomes clear that the peak structure at the VB edge near the Fermi energy is different from the other spectra. Here, more than one peak is visible, which might be surprising at first. However, comparing these spectra to published ones of other AGNRs, it shows that such multipeak structures at the VB edge position are frequently found.<sup>[137,195]</sup> Looking at the measurement positions for the spectra of 2x and 4xT30-PNGs, they are located right above pristine AGNR segments of the structures. Those additional peaks are therefore addressed as a result of the measurement location. Due to the uncertainty in determining the exact position of the CB-onset for every spectrum, calculating precise values for the bandgap width from these spectra would result in large errors. However, it is nevertheless possible to determine a lower limit for the bandgap, which in this case is  $E_{\text{Gap}} \geq 1.40$  eV for all T30-PNG spectra shown in figure 5.30.

Since the T30-PNGs provide pristine armchair edges, it is possible to compare the results of this work with other experimental bandgap values for wide pristine armchair GNRs. The only difference in structure between AGNRs and the here shown T30-PNGs, are the existing pores. Therefore, differences in electronic properties can be addressed directly to these structural variations. In the case of 4xT40-PNGs, the width of the structure is 48 carbon atom rows or 5.96 nm, and therefore larger than previously synthesized 21- or 42-AGNRs.<sup>[137]</sup> The experimentally determined bandgaps for these pristine AGNRs are 0.30 eV and 0.14 eV respectively, which matches the theoretical predicted decreasing bandgap with increasing GNR width quite well.<sup>[23]</sup> This is however almost one order of magnitude smaller than for the results shown here. This again leaves the conclusion that the integrated nanopores lead to an increased bandgap width. Moreover, that the size of the bandgap appears to be mostly independent on the structural width.

Testing the hypothesis of Baskin and Král, bandgap values of the here presented structures have to be compared with the values of pristine 5-AGNRs. Such narrow armchair GNRs were synthesized by Zhang et al, who determined the bandgap to be  $E_{\text{Gap}} = (2.10 \pm 0.10)$  eV.<sup>[118]</sup> As the result here only describes a lower limit for the bandgap, the possibility that the real bandgap of T30-PNGs is indeed close to the one of 5-AGNRs can not be ruled out.

To further investigate the individual electronic structure of the T30-PNGs,  $dI/dV$  mapping was used to spatially resolve the distribution of electronic states. In figure 5.31 the individual differential conductivity maps are shown with the respective energies given above each pair of images. The focus here lied especially on the evolution of characteristic armchair edge states and pore states in the T30-PNGs. It has to be noted that there, due to the close proximity to the stamping site, in some of the maps large adsorbates can be seen. These structures, visible as bright spots in the STM images, also result in a increased signal in the  $dI/dV$  maps. Due to the fact that these adsorbates are not structural parts of the PNG structures however, these locations will be neglected in the following discussion of the  $dI/dV$  maps.

Inside the valence band, at  $E = -1.6$  eV,  $E = -1.0$  eV and  $E = -0.8$  eV there are different individual electronic states present. Besides the typical armchair edge state, a distinct pore state appears right over each nanopore on the T30-PNGs. This state however is only present when two or more T30-GNRs are fused together and is not present in individual T30-GNR segments. Looking back at the results in figure 5.13, this is in good agreement with the observations made here, where no such state was observed in the valence band.

The maps at  $E = -0.6$  eV and  $E = +1.0$  eV show no localized states as expected from the point spectra in figure 5.30. The resulting  $dI/dV$  maps only include signal coming from adsorbates and the substrate. At  $E = -0.2$  eV, the signal from the Au surface state is superimposed on the VB edge state of the ribbon, which is therefore hardly visible. However, due to the fact that the VB edge is clearly visible in all the point spectra, it is concluded that this state could be visualized

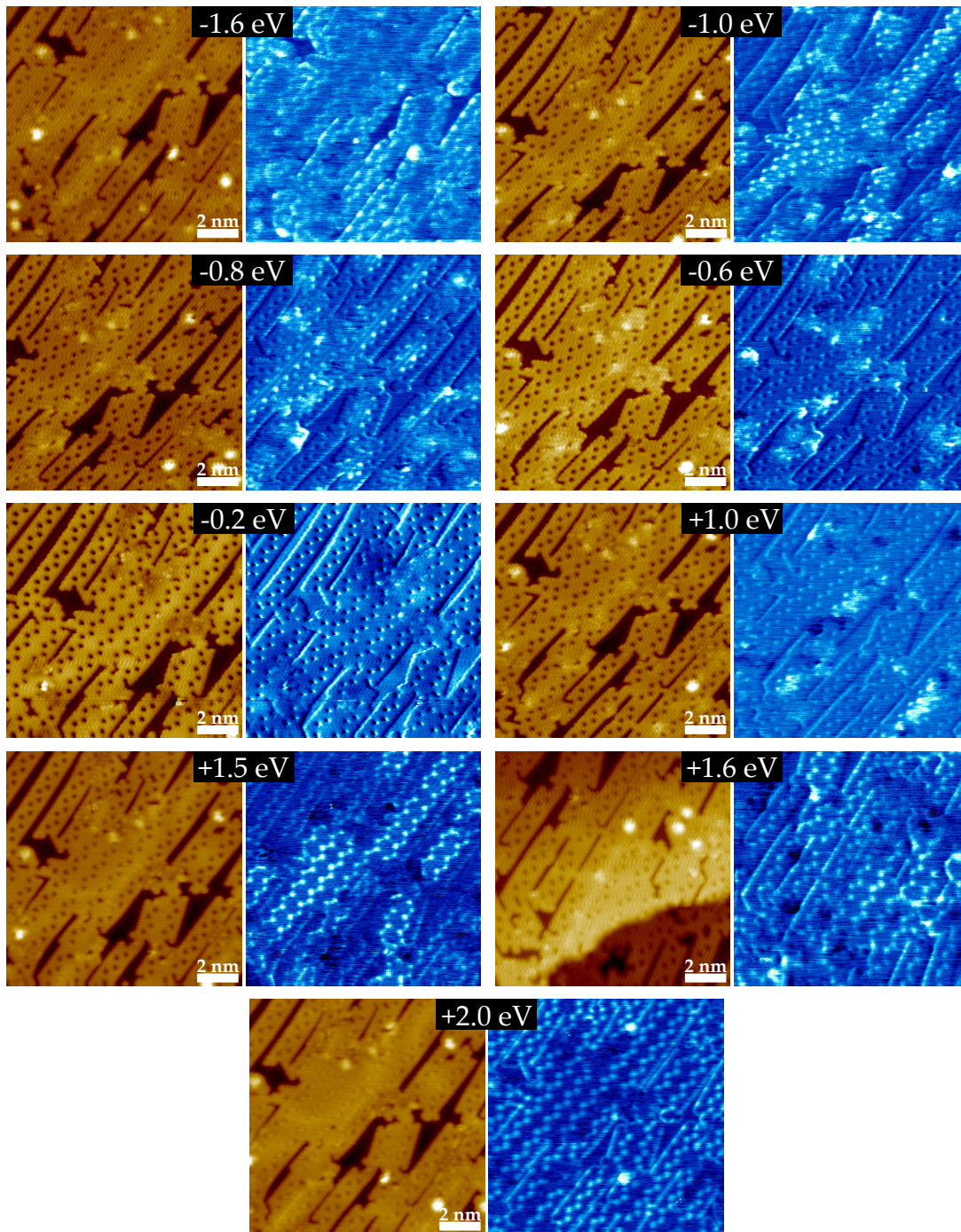


Figure 5.31:  $dI/dV$  maps of T30-PNGs. The respective energies are given above each image. All maps were taken with a setpoint of  $I_T = 1.0$  nA and with a modulation voltage of  $V_{\text{mod}} = 20$  mV at  $f_{\text{mod}} = 4.371$  kHz.

by suppressing the background signal coming from the Au substrate.

Inside the conduction band, at energies above  $E = +1.5$  eV, the armchair edge state as well as the pore state reappear. An interesting observation here is that the armchair edge state is quenched where the edges are fused together. This can be directly seen in the map at  $E = +2.0$  eV, where no such state is present inside the PNG structures but on the outer edges. From the measurements on individual T30-GNRs it is known that the pore state appears inside the conduction band. This is verified with the observations here, where it is visible in the maps at  $E = +1.5$  eV,  $E = +1.6$  eV and  $E = +2.0$  eV. In contrast to the valence band, here this state is also present on individual T30-GNR segments. However, it seems to appear with increased intensity when two or more T30-GNRs are fused.

The absence of an armchair edge state along the edges that are now inside the PNG and the increased intensity of the pore state, leaves no doubt that additional electronic states are induced when the T30-PNGs are created. The energetic location of these states in combination with the  $dI/dV$  point spectra further supports the assumption that these states mainly determine the bandgap width of the structure. It could be shown that the bandgap width is largely independent of the structural width. Additionally, the predictions of Baskin and Král can not be supported by the results presented here.

### 5.4.3 T90-PNGs

After the successful synthesis of porous nanographenes out of T30- and C30-GNRs, the question was if structures could also be built out of nonporous GNRs. While synthesizing C90-GNRs, small segments of such porous structures have already been observed, as it has been shown in figure 5.2. The problem there was the low degree of alignment between the GNRs, which limited the formation of larger PNG structures. Looking at the T90-GNRs, they seem to be the ideal system to resolve this issue. They grow exceptionally well and form large arrays of parallel aligned chains in densely covered surface areas. Due to their notched edge structure, nanopores can be formed between adjacent chains similarly as it has been observed for C90-GNRs.

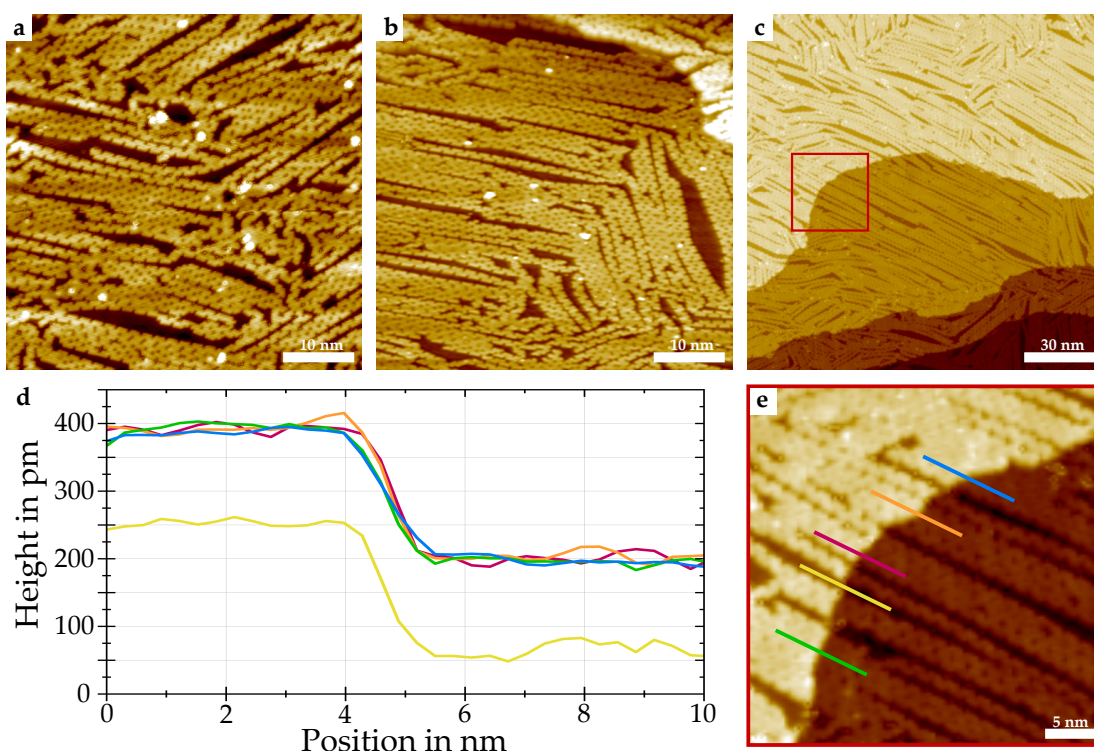


Figure 5.32: **a)** STM image of randomly oriented T90-PNGs. ( $V_B = +1.5$  V,  $I_T = 1.0$  nA) **b)** STM image of T90-PNGs, showing improved alignment and therefore wider and longer structures. ( $V_B = +1.5$  V,  $I_T = 0.6$  nA) **c)** Ultra long T90-PNGs extending over several surface step edges. ( $V_B = +1.5$  V,  $I_T = 1.0$  nA) **d)** Different linescans across the Au step edge covered with T90-PNGs. The exact location of the lines is marked in **e)** respectively. **e)** Enhanced view on the area marked in red in **c)**. The T90-GNRs clearly grow across the step edge.

To test this hypothesis, samples were prepared with the usual DCT approach and annealing times were used to promote ideal parallel alignment of the formed GNRs. Similarly to C30- and T30-GNRs, annealing the sample to  $T = 500$  °C leads to dehydrogenation of the head site carbon

atoms and allows the formation of covalent bonds between the T90-GNRs.

In figure 5.32, STM images of the resulting samples are presented. They clearly show that the exceptional growth characteristics of T90-GNRs are highly beneficial for the preparation of T90-PNGs. The large chain lengths in combination with the optimized synthesis parameters lead to an increased degree of alignment. The resulting strips of nanographenes are therefore extremely long and show very little defects.

The STM images in **a** and **b** show two surface areas, where the structures formed domains with different orientations on the surface. These orientations originate from the initial epitaxial growth of T90-GNRs prior to T90-PNG formation. One can also see that the gaps between neighboring PNG strips just rarely show parallel edges, hinting towards a zipper-like coupling mechanism. The formation of covalent bonds between adjacent chains starts at a random point where the distance to the nearest carbon atom of the neighboring chain is small. From there on the individual GNR is pulled towards the existing PNG leading to a zipper effect.

The largest T90-PNGs present in **b** consist of five T90-GNRs and are 6.1 nm wide, with their length varying between 10 nm and 30 nm. More narrow T90-PNGs are often longer, as can be seen in figure 5.32 **c**. This STM image is 150x150 nm and shows T90-PNGs up to 95 nm in length. Even for individual GNRs, such lengths are only rarely found and usually require the use of additional stabilizing mechanisms during the synthesis. The ability to produce extraordinary wide and long structures on a simple Au(111) substrate could largely facilitate the manufacturing process of FET devices.

The Au surface in figure 5.32 **c** shows three distinct step edges, along which individual GNRs are usually aligned. This is not the case here. Instead of orienting along the direction of the edge, they appear to grow over it. This is clearly visible, looking at the enhanced view on the area marked in red, shown in figure 5.7 **e**. Here the continuous structure of the T90-PNGs can be observed and it becomes apparent that the structures closely follow the topology of the substrate. To further investigate the height difference between the upper and the lower terrace and the exact shape in which the PNGs span over the edge, several lines scans were measured across the step and the height profiles are shown in **d** in the according colors.

Taking a look at the yellow profile, which shows the topology of a uncovered step edge, it can be seen that the height difference is about 200 nm, matching the results shown in figure 4.4 for monoatomic steps of the Au(111) surface. This height difference is also observable in the other line scans, taken at different locations along the step edge, which is covered by T90-PNGs. This shows that the PNG-surface distance stays constant and that the PNGs closely follow the surface topology of the substrate. The fact that the slope of all line scans is similar also shows that the PNGs bend around the edge, indicating a high flexibility of the structures in the out-of-plane direction.

Despite the large dimensions of these images, the spatial resolution allows distinguishing two different pore types. Similar to the case of C30- and T30-PNGs, different types of alignment between the individual GNRs can lead to structurally different PNGs. The major difference between these two and T90-PNGs is that due to the notched edge configuration, the size of the formed nanopores changes depending on the alignment type. In figure 5.33, both alignment types

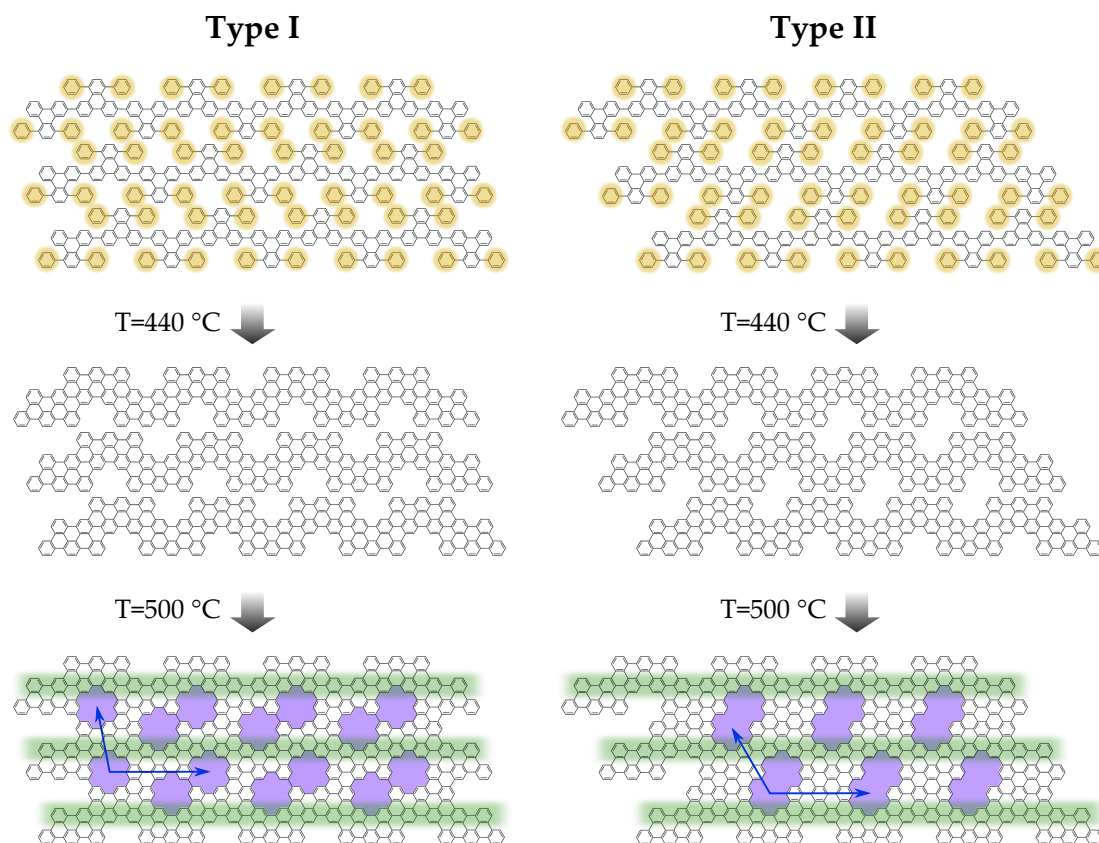


Figure 5.33: Reaction schemes for the on-surface synthesis of T90-PNGs with two pore types. Depending on the alignment, a pair of two neighboring circular vacancies (Type I), or a larger oval shaped pore (Type II) is formed. The pores are colored in purple and the 3-AGNR in green. Shown in blue are the unit cell vectors of both configuration types.

are shown side by side. The rotated phenyl rings in the polymer stage are colored in yellow. They appear as bright lobes in the STM images shown in figure 5.6 c. They are responsible for the coupling between adjacent chains. In the Type I configuration, the two phenyl rings of each precursor molecule of one chain interact with two phenyl rings of two precursor molecules of the opposing chain. Therefore, each notch is closed up by the armchair segment of the neighboring T90-GNR and circular pores with a diameter of 0.32 nm are formed when the GNRs are fused together. The size of the pores matches the ones in C30- and T30-GNRs as one six-membered

carbon-atom-ring is missing. However, here they always appear in pairs of two, separated by a single covalent bond.

The Type II configuration is formed when the precursor molecules of neighboring chains are directly opposite of each other. Here, the notches are connected, creating ovally shaped vacancies which are 0.32 nm wide and 0.84 nm long. Due to the slight misalignment of the notches, these pores are tilted with respect to the ribbon's axis at an angle of  $60^\circ$ . The unit cells of the lattice is of oblique shape in both configuration types, shown by the blue arrows, with the unit cell of the Type II configuration being slightly larger.

Counting the number of pairs of Type I pores and single Type II pores in the STM images, it was found that they appear with a ratio of 1.8:1, meaning that the circular pore pattern is more almost twice as likely to be formed than the ovally shaped pores.

To clarify the exact pore structures, they were colored in purple in the T90-PNG structure formulas at the bottom of figure 5.33, where also the 3-AGNRs, formed by the backbone of each individual T90-GNR, are highlighted in green. In this case, mirror symmetric variants of both types of pore configurations exist but will not be discussed here since they are not expected to have different electronic properties. However, as it is clear to see, the shape and size of the pores is very different and is expected to influence the electronic structure of T90-PNGs differently.

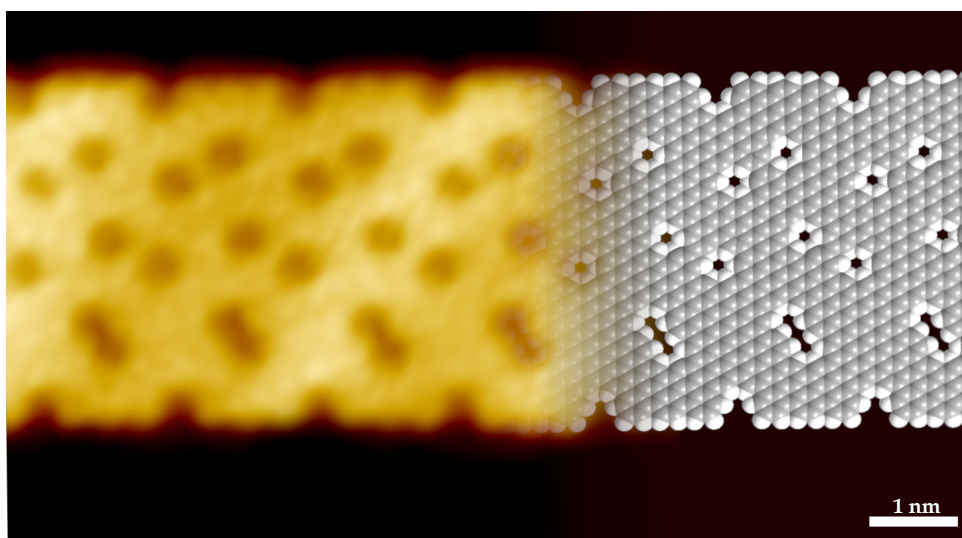


Figure 5.34: Detailed STM image of a T90-PNG with mixed pore structures. The image is superimposed with a space filling structural model on the right side to show the precise atomic structure. ( $V_B = +1.5$  V,  $I_T = 1.0$  nA)

A detailed STM image is presented in figure 5.34 that includes both configurations. Here, a T90-PNG is shown, consisting of four fused T90-GNRs with a nonuniform pore structure. The first three T90-GNRs, counting from top to bottom, are arranged in a Type I configuration, forming

pairs of circular pores with a mirrored symmetry, whereas the third and fourth T90-GNRs form a Type II pore configuration. The size of both the circular and oval shaped pores can precisely be determined from this image. A superimposed structural model is shown to clarify the exact atomic structure of this T90-PNG, where every carbon atom is represented by a gray and every hydrogen atom by a white sphere. This also underlines the fact that every carbon atom sitting at an inner or outer edge of the structure is hydrogen passivated.

However, the question remains if the bandgap width of the structures is similar to C30- and T30-PNGs and if the bandgap is also independent of the width of the PNG. Unfortunately, at the time this thesis was written, there was not yet enough data to answer these questions conclusively. Looking at the predictions of Baskin and Král,<sup>[162]</sup> one would expect the bandgap to be similar for both configurations, as the resulting 3-AGNRs should determine the bandgap width. As the results of Merino-Díez et al. predict, the bandgap of individual 3-AGNRs<sup>†</sup> on Au(111) should be  $E_{\text{Gap}} = 3.23 \text{ eV}$ ,<sup>[119]</sup> which is rather large but fits the theoretically predicted values quite well.<sup>[23,209]</sup>

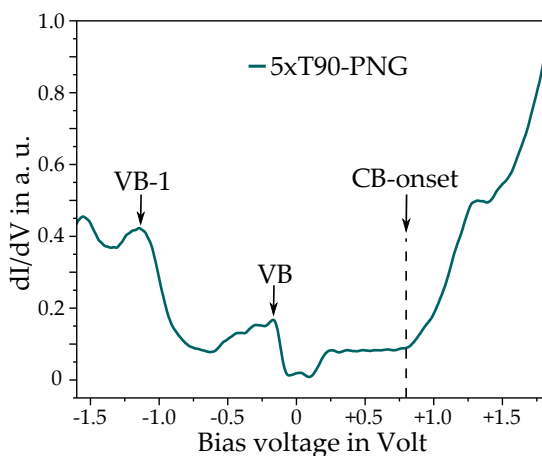


Figure 5.35:  $dI/dV$  point spectra measured at a single T90-PNG consisting of 5 fused T90-GNRs with a mixed pore configuration. VB-1 and VB edge as well as the CB-onset are marked accordingly. Measurement parameters:  $I_T = 1.0 \text{ nA}$ ,  $V_{\text{mod}} = 30 \text{ mV}$ ,  $f_{\text{mod}} = 859 \text{ Hertz}$ .

The  $dI/dV$  point spectrum shown in figure 5.35 is the result of a single measurement taken on a T90-PNG with a mixed pore configuration, consisting of five fused T30-GNRs. In this particular spectrum, the VB-1 and VB edge can be directly observed at  $-1.15 \text{ eV}$  and  $-0.2 \text{ eV}$ . The determination of the CB onset is not that simple. Besides the usual increase in signal around  $+0.78 \text{ eV}$ , there is also a distinct step like feature visible around  $+0.25 \text{ eV}$ . Depending on which of these is interpreted as the CB edge, the bandgap of the structure could either be calculated to be  $E_{\text{Gap}} \approx 0.45 \text{ eV}$  or  $E_{\text{Gap}} \approx 0.98 \text{ eV}$ . A definite determination of the bandgap is therefore not possible with this data.

However, comparing these results with the hypothesis of Baskin and Král, the expected and experimentally observed bandgap widths are largely different. A exact determination of the electronic structure of T90-PNGs remains to be conducted in future experiments and should additionally be supported by theoretical calculations.

<sup>†</sup>In their work they referred to these GNRs as poly(para-phenylenes) or PPP-wires.

#### 5.4.4 Conclusion and outlook

The results shown here present the first documentation of the synthesis of porous nanographenes out of individual GNRs. It could be shown that attractive forces between individual polymer chains can be utilized to produce arrays of parallelly aligned GNRs. A additional dehydrogenation process can then be used to initiate the formation of covalent bonds between adjacent GNRs. This fusing process happens in a zipper-like fashion and results in the formation of wide strips of nanographenes.

Using this approach with the novel GNRs presented in this thesis revealed that it is possible to create porous nanographenes with two distinct strategies. One, by using already porous GNRs for the synthesis and thereby integrating the periodic vacancies in the structure. Or two, by using nonporous GNRs with a notched, or chevron-like edge structure, where nanopores are formed during the lateral fusing process. The initial alignment of the individual GNRs plays an important role in both cases, as different pore structures can exist depending on the alignment type.

Comparing the PNG structures presented in this work, it could be shown that the initial growth conditions of the individual GNRs strongly affect the quality and size of the synthesized PNGs. In the case of T90-PNGs, the extraordinary length and the perfect alignment of the individual GNRs led to the formation of defect free and extremely long porous nanographenes. Whereas for both C30- and T30-PNGs, the structures were rather short and incorporated a variety of defects.

The electronic characterization of all C30- and T30-PNGs with STS proved that they are semi-conducting. This supports the hypothesis that it is possible to induce semiconducting properties in large nanographene sheets by introducing periodic nanopores into the lattice. However, it is even more surprising that for both structures it was found that the bandgap width does not change significantly with the width of the structure. This indicates that the bandgap of these PNG structures is solely determined by the periodicity and size of the pores. Even larger porous nanographene structures are therefore expected to also show a similar bandgap.

These findings pose as the first spectroscopic characterization of porous nanographene structures and will hopefully be confirmed by future experiments. As a next step, further STS measurements on T90-PNGs are planned to further support the theory of a structurally independent bandgap width. With regard to the fabrication of devices out of PNGs, ideas are currently under discussion in close collaboration with the group of Prof. Sinitskii.

## 6 Summary

The experimental work presented in this thesis poses as a significant contribution to the state of the art in graphene nanoribbon research. Graphene nanoribbons have become an important class of nanomaterials due to their amenability to tailoring of their semiconducting properties by structural design. As a result, they are now able to compete with traditional inorganic semiconductor materials such as silicon, gallium arsenide and germanium. By building on recently established principles to manipulate the electronic band structure parameters with relevance for device applications, it was possible to experimentally confirm for the first time the correlation between periodic structural vacancies in graphene nanoribbons and their band structure.

The research goal was to expand existing strategies for the on-surface synthesis of graphene nanoribbons and nanographenes and to experimentally explore the parameters that define their electronic properties. In order to achieve this goal, a new class of molecular precursors was used, which were rationally designed for this study in collaboration with the group of Prof. Sinitskii at the University of Nebraska – Lincoln. With these molecules, novel graphene nanoribbons were synthesized that showed unique structural features like periodic structural vacancies along the GNR's backbone. Also, a new surface scientific approach was developed, which is the diffusion controlled on-surface self-assembly, to construct graphene nanoribbon heterostructures and heterojunctions. It was further demonstrated for the first time, that a topochemistry approach to form nanographenes from graphene nanoribbons, poses as an easy strategy to synthesize porous nanographenes.

A major part of the experimental work involved the setup of an ultrahigh vacuum low temperature scanning tunneling microscope at the University of Bayreuth. While this was an already existing apparatus which had to be transferred to UBT from the University of Nebraska – Lincoln, this task involved substantial refurbishment of the equipment. Additionally, numerous additions and improvements to the apparatus, had to be developed and constructed, involving the design of a new sample load lock, building an in-situ tip annealing tool, tools for in-situ molecular deposition, and establishing procedures and parameters for scanning tunneling spectroscopy.

---

Key outcomes of the studies included in this thesis are:

- the first demonstration that the halogen-atom-guided self-assembly of precursor molecules with 30 degree bond angles with respect to the molecular symmetry axis is a design principle to build porous GNRs
- the first demonstration that differences in the surface diffusivity of precursor molecules can be exploited to synthesize GNR heterostructures of controlled stoichiometry
- the first demonstration that the specific topology of GNR's edges upon dense packing is key to the formation of nanographenes from individual GNRs
- experimental evidence that the electronic band gap of porous nanographenes is mainly determined by their periodically arranged structural vacancies
- experimental evidence that new localized electronic states arise when structural vacancies are introduced into GNR or PNG structures.

Furthermore, other interesting experimental results were obtained. For example, it could be shown that the products of on-surface synthesis routes and synthesis in solution can be different, even if the initial precursor molecules are the same. It was also found that it is possible to synthesize porous GNRs without the use of brominated precursor molecules out of C30-triangles. Of special interest was also the experimental verification of a theoretically postulated localized interface state in C90-GNR/9-AGNR heterojunctions.

The intellectual merit of this study is in pushing the limits of the rational design of nanographenes and in the discovery of a new and critical parameter that determines their electronic band structure. More specifically, this work could show that designing the incorporation of structural vacancies is a viable way to build semiconducting graphene. Through further development of this strategy, the currently existing major hindrance to make use of the unique properties of graphene in 2D electronics and device applications, the lack of an electronic band gap, could be overcome. The results of this study might also be of fundamental importance in guiding the discovery of other porous 2D materials.

# 7 Appendix

## 7.1 STS parameters

Presented here is a list of typical values for the parameters set during  $dI/dV$  measurements.

Parameters set in the Matrix software:

- $V$ -start =  $-2.500\text{ V}$
- $V$ -end =  $+2.500\text{ V}$
- Points = 500
- $T$ -Raster =  $20.00\text{ ms}$
- Slew Rate =  $500\text{ mV s}^{-1}$

Delay Times:

- $T1 = 30.00\text{ ms}$
- $T2 = 30.00\text{ ms}$
- $T3 = 30.00\text{ ms}$
- $T4 = 30.00\text{ ms}$

- Gap Preset unticked

Parameters set on the function generator:

Waveform = Sine

Amplitude =  $30\text{ mV}$

Frequency =  $\left\{ \begin{array}{ll} 859\text{ Hz} & \text{for } dI/dV \text{ point spectroscopy} \\ 4.371\text{ kHz} & \text{for } dI/dV \text{ mapping} \end{array} \right.$

Parameters set on the Lock-in-amplifier:

$$\begin{aligned} \text{Slope/Octave} &= 24 \text{ dB/oct} \\ \text{Time constant} &= \begin{cases} 30 \text{ ms} & \text{for } dI/dV \text{ point spectroscopy} \\ 3 \text{ ms} & \text{for } dI/dV \text{ mapping} \end{cases} \end{aligned}$$

Sensitivity value has to be adjusted to make use of the whole measurement range.

## 7.2 IUPAC names of precursor molecules

Notation	IUPAC name
9-A	3',6'-dibromo-1,1':2',1''-terphenyl
T90	6,11-dibromo-1,4-diphenyltriphenylene
T30	7,10-dibromo-1,4-diphenyltriphenylene
C30	7,10-dibromo-1,2,3,4-tetraphenyltriphenylene
C90	6,11-dibromo-1,2,3,4-tetraphenyltriphenylene

Table 7.1: Table of exact IUPAC names of the precursor molecules shown in figure 5.1 with the corresponding abbreviations in this work.

## 7.3 C90-/T90-GNR Heterojunctions

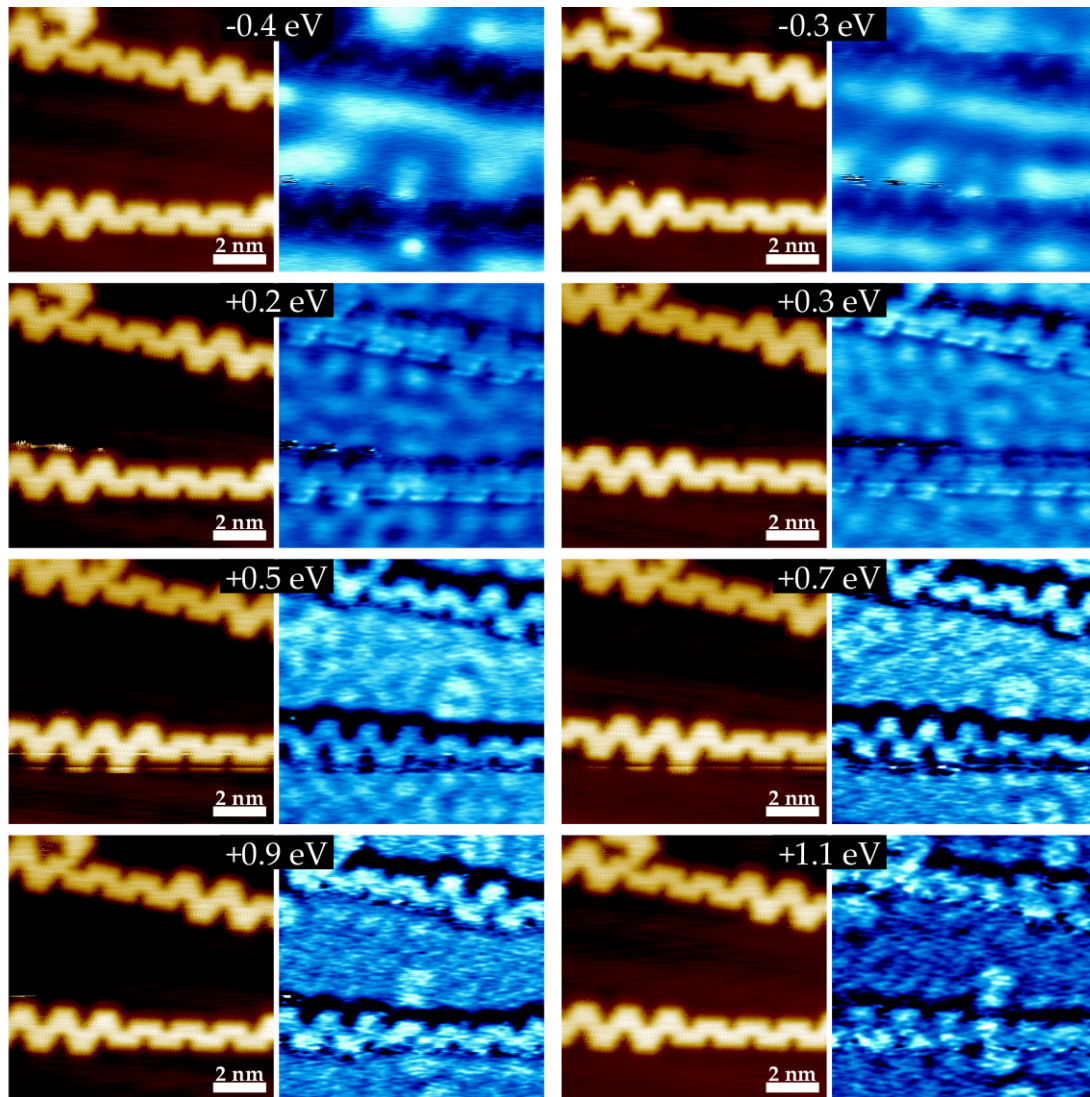


Figure 7.1:  $dI/dV$  maps of a C90-/T90-GNR heterojunction. The respective energies are given above each image. All maps were taken with a setpoint of  $I_T = 1.0$  nA and with a modulation voltage of  $V_{\text{mod}} = 20$  mV at  $f_{\text{mod}} = 4.371$  kHz.



# Bibliography

- [1] O. Burkacky, J. Dragon and N. Lehman, *The semiconductor decade: A trillion-dollar industry*, 2022, <https://www.mckinsey.com/industries/semiconductors/our-insights/the-semiconductor-decade-a-trillion-dollar-industry>.
- [2] J. Green, *Detailed Introduction to Three Generations of Semiconductor Materials*, 2022, <https://www.sputtertargets.net/blog/introduction-to-the-generations-of-semiconductors.html>.
- [3] E. Montalbano, *Semiconductor Materials Offer Alternatives to Silicon*, 2018.
- [4] L. James, *When Moore's Law Ends: 3 Alternatives to Silicon Chips*, 2018, <https://www.makeuseof.com/tag/moores-law-silicon-chips/>.
- [5] *Alternatives to Silicon: Graphene, Gallium Nitride and Perovskites*, 2020, <https://www.findlight.net/blog/2020/07/19/alternatives-to-silicon/>.
- [6] K. S. Novoselov, A. K. Geim, S. V. Morozov, D. Jiang, Y. Zhang, S. V. Dubonos, I. V. Grigorieva and A. A. Firsov, *Science*, 2004, **306**, 666–669.
- [7] K. S. Novoselov, A. K. Geim, S. V. Morozov, D. Jiang, M. I. Katsnelson, I. V. Grigorieva, S. V. Dubonos and A. A. Firsov, *Nature*, 2005, **438**, 197–200.
- [8] A. K. Geim and K. S. Novoselov, *Nature Mat.*, 2007, **6**, 183–191.
- [9] A. H. C. Neto, F. Guinea, N. M. R. Peres, K. S. Novoselov and A. K. Geim, *Rev. Mod. Phys.*, 2009, **81**, 109–162.
- [10] A. A. Balandin, S. Ghosh, W. Bao, I. Calizo, D. Teweldebrhan, F. Miao and C. N. Lau, *Nano Lett.*, 2008, **8**, 902–907.
- [11] F. Schwier, *Graphene for electronic applications - Transistors and more*, In: Bipolar/BiCMOS Circuits and Technology Meeting. IEEE, 2010.
- [12] S. Y. Zhou, D. A. Siegel, A. V. Fedorov and A. Lanzara, *Phys. Rev. Lett.*, 2008, **101**, 086402.

- 
- [13] D. C. Elias, R. R. Nair, T. M. G. Mohiuddin, S. V. Morozov, P. Blake, M. P. Halsall, A. C. Ferrari, D. W. Boukhvalov, M. I. Katsnelson, A. K. Geim and K. S. Novoselov, *Science*, 2009, **323**, 610–613.
- [14] S. Y. Zhou, G.-H. Gweon, A. V. Fedorov, P. N. First, W. A. de Heer, D.-H. Lee, F. Guinea, A. H. C. Neto and A. Lanzara, *Nat. Mater.*, 2007, **6**, 770–775.
- [15] S. Y. Zhou, D. A. Siegel, A. V. Fedorov, F. E. Gabaly, A. K. Schmid, A. H. C. Neto, D.-H. Lee and A. Lanzara, *Nat. Mater.*, 2008, **7**, 259–260.
- [16] S. Kim, J. Ihm, H. J. Choi and Y.-W. Son, *Phys. Rev. Lett.*, 2008, **100**, 176802.
- [17] E. V. Castro, K. S. Novoselov, S. V. Morozov, N. M. R. Peres, J. M. B. L. dos Santos, J. Nilsson, F. Guinea, A. K. Geim and A. H. C. Neto, *Phys. Rev. Lett.*, 2007, **99**, 216802.
- [18] F. Xia, D. B. Farmer, Y. ming Lin and P. Avouris, *Nano Lett.*, 2010, **10**, 715–718.
- [19] M. Fujita, K. Wakabayashi, K. Nakada and K. Kusakabe, *J. Phys. Soc. Jpn.*, 1996, **65**, 1920–1923.
- [20] K. Nakada, M. Fujita, G. Dresselhaus and M. S. Dresselhaus, *Phys. Rev. B*, 1996, **54**, 17954–17961.
- [21] K. Wakabayashi, M. Fujita, H. Ajiki and M. Sigrist, *Phys. Rev. B*, 1999, **59**, 8271–8282.
- [22] V. Barone, O. Hod and G. E. Scuseria, *Nano Lett.*, 2006, **6**, 2748–2754.
- [23] Y.-W. Son, M. L. Cohen and S. G. Louie, *Nature*, 2006, **444**, 347–349.
- [24] M. Y. Han, B. Özyilmaz, Y. Zhang and P. Kim, *Phys. Rev. Lett.*, 2007, **98**, 206805–4.
- [25] H. Zheng, Z. F. Wang, T. Luo, Q. W. Shi and J. Chen, *Phys. Rev. B*, 2007, **75**, 165414.
- [26] J. Cai, P. Ruffieux, R. Jaafar, M. Bieri, T. Braun, S. Blankenburg, M. Muoth, A. P. Seitsonen, M. Saleh, X. Feng, K. Müllen and R. Fasel, *Nature*, 2010, **466**, 470–473.
- [27] C. J. Chen, *Introduction to Scanning Tunneling Microscopy*, Oxford: Oxford University Press, 3rd edn., 2021.
- [28] R. Wiesendanger and H.-J. Güntherodt, *Scanning Tunneling Microscopy III*, Springer Berlin, 1996.
- [29] G. Binnig, H. Rohrer, C. Gerber and E. Weibel, *Phys. Rev. Lett.*, 1982, **49**, 57–61.

- [30] G. Binnig, H. Rohrer, C. Gerber and E. Weibel, *Appl. Phys. Lett.*, 1982, **40**, 178–180.
- [31] G. Bracco, M. Smerieri and L. Savio, in *Self-assembly of Organic Molecules at Metal Surfaces*, ed. M. Rocca, T. S. Rahman and L. Vattuone, Springer International Publishing, Cham, 2020, pp. 967–1004.
- [32] P. Atkins and J. de Paula, *Physical Chemistry*, W. H. Freeman and Company, 8th edn., 2006.
- [33] S. Ross and J. P. Olivier, *On Physical Adsorption*, John Wiley and Sons, Inc., 1964.
- [34] L. E. M. Steinkasserer, B. Paulus and E. Voloshina, *Chem. Phys. Lett.*, 2014, **597**, 148–152.
- [35] P. Han, K. Akagi, F. F. Canova, H. Mutoh, S. Shiraki, K. Iwaya, P. S. Weiss, N. Asao and T. Hitosugi, *ACS Nano*, 2014, **8**, 9181–9187.
- [36] K. Sun, X. Li, L. Chen, H. Zhang and L. Chi, *J. Phys. Chem. C*, 2020, **124**, 11422–11427.
- [37] F. J. Martín-Martínez, S. Fias, G. Van Lier, F. De Proft and P. Geerlings, *Chemistry – A European Journal*, 2012, **18**, 6183–6194.
- [38] M. Shekhirev, T. H. Vo, D. A. Kunkel, A. Lipatov, A. Enders and A. Sinitiskii, *RSC Adv.*, 2017, **7**, 54491–54499.
- [39] M. Shekhirev, T. H. Vo, M. M. Pour, A. Lipatov, S. Munukutla, J. W. Lyding and A. Sinitiskii, *ACS Appl. Mater. Interfaces*, 2017, **9**, 693–700.
- [40] R. Otero, A. L. V. de Parga and J. M. Gallego, *Surf. Sci. Rep.*, 2017, **72**, 105–145.
- [41] P. S. Bagus, V. Staemmler and C. Wöll, *Phys. Rev. Lett.*, 2002, **89**, 096104.
- [42] P. S. Bagus, K. Hermann and C. Wöll, *J. Chem. Phys.*, 2005, **123**, 184109.
- [43] J. Fraxedas, S. García-Gil, S. Monturet, N. Lorente, I. Fernández-Torrente, K. J. Franke, J. I. Pascual, A. Vollmer, R.-P. Blum, N. Koch and P. Ordejón, *J. Phys. Chem. C*, 2011, **115**, 18640–18648.
- [44] O. P. Watts and C. E. Mendenhall, *Phys. Rev. (Series I)*, 1911, **33**, 65–69.
- [45] J. D. Bernal, *Proc. R. Soc. Lond. A*, 1924, **106**, 749–773.
- [46] G. W. Semenoff, *Phys. Rev. Lett.*, 1984, **53**, 2449–2452.
- [47] D. P. DiVincenzo and E. J. Mele, *Phys. Rev. B*, 1984, **29**, 1685–1694.

- [48] O. A. Shenderova, V. V. Zhirnov and D. W. Brenner, *Critical Reviews in Solid State and Materials Sciences*, 2002, **27**, 227–356.
- [49] A. Krishnan, E. Dujardin, M. M. J. Treacy, J. Hugdahl, S. Lynum and T. W. Ebbesen, *Nature*, 1997, **388**, 451–454.
- [50] S. Hembacher, F. J. Giessibl, J. Mannhart and C. F. Quate, *Proceedings of the National Academy of Sciences of the United States of America*, 2003, **100**, 12539–12542.
- [51] M. Corso, E. Carbonell-Sanromà and D. G. de Oteyza, in *Bottom-Up Fabrication of Atomically Precise Graphene Nanoribbons*, Springer Nature, 2018, pp. 113–152.
- [52] K. I. Bolotin, K. J. Sikes, Z. Jiang, M. Klima, G. Fudenberg, J. Hone, P. Kim and H. L. Stormer, *Solid State Comm.*, 2008, **146**, 351–355.
- [53] C. Lee, X. Wei, J. W. Kysar and J. Hone, *Science*, 2008, **321**, 385–388.
- [54] E. Pop, V. Varshney and A. K. Roy, *MRS Bulletin*, 2012, **37**, 1273–1281.
- [55] P. A. Denis, R. Faccio and A. W. Momburu, *Chem. Phys. Chem.*, 2009, **10**, 715–722.
- [56] D. Wei, Y. Liu, Y. Wang, H. Zhang, L. Huang and G. Yu, *Nano Lett.*, 2009, **9**, 1752–1758.
- [57] P. Rani and V. K. Jindal, *RSC Adv.*, 2013, **3**, 802–812.
- [58] E. Bekyarova, M. E. Itkis, P. Ramesh, C. Berger, M. Sprinkle, W. A. de Heer and R. C. Haddon, *J. Am. Chem. Soc.*, 2009, **131**, 1336–1337.
- [59] X. Wang, X. Li, L. Zhang, Y. Yoon, P. K. Weber, H. Wang, J. Guo and H. Dai, *Science*, 2009, **324**, 768–771.
- [60] X. Fan, Z. Shen, A. Q. Liu and J.-L. Kuo, *Nanoscale*, 2012, **4**, 2157.
- [61] E. McCann and V. I. Fal'ko, *Phys. Rev. Lett.*, 2006, **96**, 086805.
- [62] E. McCann, D. S. L. Abergel and V. I. Fal'ko, *Solid State Comm.*, 2007, **143**, 110–115.
- [63] Y. Zhang, T.-T. Tang, C. Girit, Z. Hao, M. C. Martin, A. Zettl, M. F. Crommie, Y. R. Shen and F. Wang, *Nature*, 2009, **459**, 820–823.
- [64] C. Berger, Z. Song, T. Li, X. Li, A. Y. Ogbazghi, R. Feng, Z. Dai, A. N. Marchenkov, E. H. Conrad, P. N. First and W. A. de Heer, *J. Phys. Chem. B*, 2004, **108**, 19912–19916.
- [65] O. V. Yazyev, *Acc. Chem. Res.*, 2013, **46**, 2319–2328.

- [66] O. V. Yazyev, *Reports on Progress in Physics*, 2010, **73**, 056501.
- [67] J. Kim, N. Lee, Y. H. Min, S. Noh, N.-K. Kim, S. Jung, M. Joo and Y. Yamada, *ACS Omega*, 2018, **3**, 17789–17796.
- [68] W.-X. Wang, M. Zhou, X. Li, S.-Y. Li, X. Wu, W. Duan and L. He, *Phys. Rev. B*, 2016, **93**, 241403.
- [69] P. Ruffieux, S. Wang, B. Yang, C. Sánchez-Sánchez, J. Liu, T. Dienel, L. Talirz, P. Shinde, C. A. Pignedoli, D. Passerone, T. Dumslaff, X. Feng, K. Müllen and R. Fasel, *Nature*, 2016, **531**, 489–492.
- [70] R. E. Blackwell, F. Zhao, E. Brooks, J. Zhu, I. Piskun, S. Wang, A. Delgado, Y.-L. Lee, S. G. Louie and F. R. Fischer, *Nature*, 2021, **600**, 647–652.
- [71] F. Ma, Z. Guo, K. Xu and P. K. Chu, *Solid State Comm.*, 2012, **152**, 1089–1093.
- [72] D. V. Kosynkin, A. L. Higginbotham, A. Sinitskii, J. R. Lomeda, A. Dimiev, B. K. Price and J. M. Tour, *Nature*, 2009, **458**, 872–876.
- [73] L. Jiao, X. Wang, G. Diankov, H. Wang and H. Dai, *Nature Nanotech.*, 2010, **5**, 321–325.
- [74] D. B. Shinde, M. Majumder and V. K. Pillai, *Sci. Rep.*, 2015, **4**, 4363.
- [75] L. Jiao, L. Zhang, X. Wang, G. Diankov and H. Dai, *Nature*, 2009, **458**, 877–880.
- [76] S.-C. Jeon, Y.-S. Kim and D.-K. Lee, *Transactions on Electrical and Electronic Materials*, 2010, **11**, 190–193.
- [77] Z. J. Qi, J. A. Rodríguez-Manzo, A. R. Botello-Méndez, S. J. Hong, E. A. Stach, Y. W. Park, J.-C. Charlier, M. Drndić and A. T. C. Johnson, *Nano Lett.*, 2014, **14**, 4238–4244.
- [78] Z. Chen, Y.-M. Lin, M. J. Rooks and P. Avouris, *Physica E: Low-dimensional Systems and Nanostructures*, 2007, **40**, 228–232.
- [79] X. Zhang, O. V. Yazyev, J. Feng, L. Xie, C. Tao, Y.-C. Chen, L. Jiao, Z. Pedramrazi, A. Zettl, S. G. Louie, H. Dai and M. F. Crommie, *ACS Nano*, 2013, **7**, 198–202.
- [80] L. C. Campos, V. R. Manfrinato, J. D. Sanchez-Yamagishi, J. Kong and P. Jarillo-Herrero, *Nano Lett.*, 2009, **9**, 2600–2604.
- [81] L. Ci, Z. Xu, L. Wang, W. Gao, F. Ding, K. F. Kelly, B. I. Yakobson and P. M. Ajayan, *Nano Res.*, 2008, **1**, 116–122.

- [82] S. S. Datta, D. R. Strachan, S. M. Khamis and A. T. C. Johnson, *Nano Lett.*, 2008, **8**, 1912–1915.
- [83] J. K. Stille, G. K. Noren and L. Green, *J. Polym. Sci.*, 1970, **8**, 2245–2254.
- [84] U. Scherf and K. Müllen, *The synthesis of ladder polymers*, 1995.
- [85] S. Zhang, *Materials Today*, 2003, **6**, 20 – 27.
- [86] X. Yang, X. Dou, A. Rouhanipour, L. Zhi, H. J. Räder and K. Müllen, *J. Am. Chem. Soc.*, 2008, **130**, 4216–4217.
- [87] L. Dössel, L. Gherghel, X. Feng and K. Müllen, *Angew. Chem. Int. Ed.*, 2011, **50**, 2540–2543.
- [88] A. Narita, X. Feng, Y. Hernandez, S. A. Jensen, M. Bonn, H. Yang, I. A. Verzhbitskiy, C. Casiraghi, M. R. Hansen, A. H. R. Koch, G. Fytas, O. Ivasenko, B. Li, K. S. Mali, T. Balandina, S. Mahesh, S. D. Feyter and K. Müllen, *Nature Chem.*, 2014, **6**, 126–132.
- [89] K. T. Kim, J. W. Jung and W. H. Jo, *Carbon*, 2013, **63**, 202–209.
- [90] M. G. Schwab, A. Narita, S. Osella, Y. Hu, A. Maghsoumi, A. Mavrinsky, W. Pisula, C. Castiglioni, M. Tommasini, D. Beljonne, X. Feng and K. Müllen, *Chem. -Asian J.*, 2015, **10**, 2002–2002.
- [91] S. Setayesh, A. C. Grimsdale, T. Weil, V. Enkelmann, K. Müllen, F. Meghdadi, E. J. W. List and G. Leising, *J. Am. Chem. Soc.*, 2001, **123**, 946–953.
- [92] J. Lee, H.-J. Cho, B.-J. Jung, N. S. Cho and H.-K. Shim, *Macromolecules*, 2004, **37**, 8523–8529.
- [93] M. G. Schwab, A. Narita, Y. Hernandez, T. Balandina, K. S. Mali, S. D. Feyter, X. Feng and K. Müllen, *J. Am. Chem. Soc.*, 2012, **134**, 18169–18172.
- [94] M. Saleh, M. Baumgarten, A. Mavrinskiy, T. Schäfer and K. Müllen, *Macromolecules*, 2010, **43**, 137–143.
- [95] T. H. Vo, M. Shekhirev, D. A. Kunkel, M. D. Morton, E. Berglund, L. Kong, P. M. Wilson, P. A. Dowben, A. Enders and A. Sinitskii, *Nature Comm.*, 2014, **5**, 3189.
- [96] T. H. Vo, M. Shekhirev, D. A. Kunkel, F. Orange, M. J.-F. Guinel, A. Enders and A. Sinitskii, *Chem. Comm.*, 2014, **50**, 4172–4174.

- [97] A. Narita, I. A. Verzhbitskiy, W. Frederickx, K. S. Mali, S. A. Jensen, M. R. Hansen, M. Bonn, S. D. Feyter, C. Casiraghi, X. Feng and K. Müllen, *ACS Nano*, 2014, **8**, 11622–11630.
- [98] L. Grill, M. Dyer, L. Lafferentz, M. Persson, M. V. Peters and S. Hecht, *Nature Nanotech.*, 2007, **2**, 687–691.
- [99] A. Gourdon, *Angew. Chem. Int.*, 2008, **47**, 6950–6953.
- [100] D. G. de Oteyza, A. García-Lekue, M. Vilas-Varela, N. Merino-Díez, E. Carbonell-Sanromà, M. Corso, G. Vasseur, C. Rogero, E. Guitián, J. I. Pascual, J. E. Ortega, Y. Wakayama and D. Peña, *ACS Nano*, 2016, **10**, 9000–9008.
- [101] M. Koch, M. Gille, A. Viertel, S. Hecht and L. Grill, *Surface Science*, 2014, **627**, 70–74.
- [102] J. D. Teeter, P. S. Costa, M. M. Pour, D. P. Miller, E. Zurek, A. Enders and A. Sinitskii, *Chem. Comm.*, 2017, **53**, 8463–8466.
- [103] K. A. Simonov, A. V. Generalov, A. S. Vinogradov, G. I. Svirskiy, A. A. Cafolla, C. McGuinness, T. Taketsugu, A. Lyalin, N. Mårtensson and A. B. Preobrajenski, *Sci. Rep.*, 2018, **8**, 3506.
- [104] P. H. Jacobse, K. A. Simonov, M. J. J. Mangnus, G. I. Svirskiy, A. V. Generalov, A. S. Vinogradov, A. Sandell, N. Mårtensson, A. B. Preobrajenski and I. Swart, *J. Phys. Chem. C*, 2019, **123**, 8892–8901.
- [105] H. Karakachian, T. T. N. Nguyen, J. Aprojanz, A. A. Zakharov, R. Yakimova, P. Rosenzweig, C. M. Polley, T. Balasubramanian, C. Tegenkamp, S. R. Power and U. Starke, *Nature Comm.*, 2020, **11**, 6380.
- [106] S. Linden, D. Zhong, A. Timmer, N. Aghdassi, J. H. Franke, H. Zhang, X. Feng, K. Müllen, H. Fuchs, L. Chi and H. Zacharias, *Phys. Rev. Lett.*, 2012, **108**, 216801.
- [107] F. D. Boni, G. Merlin, F. Sedona, S. Casalini, M. M. S. Fakhrabadi and M. Sambri, *Appl. Nano Mat.*, 2020, **3**, 11497–11509.
- [108] Y. Zhang, Y. Zhang, G. Li, J. Lu, X. Lin, S. Du, R. Berger, X. Feng, K. Müllen and H.-J. Gao, *Appl. Phys. Lett.*, 2014, **105**, 023101.
- [109] B. Jeong, M. Wuttke, Y. Zhou, K. Müllen, A. Narita and K. Asadi, *ACS Applied Electronic Materials*, 2022, **4**, 2667–2671.

- [110] G. B. Barin, A. Fairbrother, L. Rotach, M. Bayle, M. Paillet, L. Liang, V. Meunier, R. Hauert, T. Dumsloff, A. Narita, K. Müllen, H. Sahabudeen, R. Berger, X. Feng, R. Fasel and P. Ruffieux, *Appl. Nano Mat.*, 2019, **2**, 2184–2192.
- [111] J. P. Llinas, A. Fairbrother, G. B. Barin, W. Shi, K. Lee, S. Wu, B. Y. Choi, R. Braganza, J. Lear, N. Kau, W. Choi, C. Chen, Z. Pedramrazi, T. Dumsloff, A. Narita, X. Feng, K. Müllen, F. Fischer, A. Zettl, P. Ruffieux, E. Yablonovitch, M. Crommie, R. Fasel and J. Bokor, *Nature Comm.*, 2017, **8**, 633.
- [112] O. Deniz, C. Sánchez-Sánchez, T. Dumsloff, X. Feng, A. Narita, K. Müllen, N. Kharche, V. Meunier, R. Fasel and P. Ruffieux, *Nano Lett.*, 2017, **17**, 2197–2203.
- [113] O. Deniz, C. Sánchez-Sánchez, R. Jaafar, N. Kharche, L. Liang, V. Meunier, X. Feng, K. Müllen, R. Fasel and P. Ruffieux, *Chem. Comm.*, 2018, **54**, 1619–1622.
- [114] H. Chen, Y. Que, L. Tao, Y.-Y. Zhang, X. Lin, W. Xiao, D. Wang, S. Du, S. T. Pantelides and H.-J. Gao, *Nano Research*, 2018, **11**, 3722–3729.
- [115] S. Wang, L. Talirz, C. A. Pignedoli, X. Feng, K. Müllen, R. Fasel and P. Ruffieux, *Nature Comm.*, 2016, **7**, 11507.
- [116] Y.-C. Chen, D. G. de Oteyza, Z. Pedramrazi, C. Chen, F. R. Fischer and M. F. Crommie, *ACS Nano*, 2013, **7**, 6123–6128.
- [117] L. Talirz, P. Ruffieux and R. Fasel, *ACS Nano*, 2016, **28**, 6222–6231.
- [118] H. Zhang, H. Lin, K. Sun, L. Chen, Y. Zagranyski, N. Aghdassi, S. Duhm, Q. Li, D. Zhong, Y. Li, K. Müllen, H. Fuchs and L. Chi, *J. Am. Chem. Soc.*, 2015, **137**, 4022–4025.
- [119] N. Merino-Díez, A. Garcia-Lekue, E. Carbonell-Sanromà, J. Li, M. Corso, L. Colazzo, F. Sedona, D. Sánchez-Portal, J. I. Pascual and D. G. de Oteyza, *ACS Nano*, 2017, **11**, 11661–11668.
- [120] A. Kimouche, M. M. Ervasti, R. Drost, S. Halonen, A. Harju, P. M. Joensuu, J. Sainio and P. Liljeroth, *Nature Comm.*, 2015, **6**, 6:10177.
- [121] J. Liu, B.-W. Li, Y.-Z. Tan, A. Giannakopoulos, C. Sanchez-Sanchez, D. Beljonne, P. Ruffieux, R. Fasel, X. Feng and K. Müllen, *J. Am. Chem. Soc.*, 2015, **137**, 6097–6103.
- [122] J. D. Teeter, P. Zahl, M. M. Pour, P. S. Costa, A. Enders and A. Sinitskii, *Chem. Phys. Chem*, 2019, **20**, 2281–2285.

- [123] C. Tao, L. Jiao, O. V. Yazyev, Y.-C. Chen, J. Feng, X. Zhang, R. B. Capaz, J. M. Tour, A. Zettl, S. G. Louie, H. Dai and M. F. Crommie, *Nature Phys.*, 2011, **7**, 616–620.
- [124] S. Sun, Y. Guan, Z. Hao, Z. Ruan, H. Zhang, J. Lu, L. Gao, X. Zuo and J. Cai, *Nano Res.*, 2022, **15**, 653–658.
- [125] C. Bronner, S. Stremlau, M. Gille, F. Brauße, A. Haase, S. Hecht and P. Tegeder, *Angew. Chem. Int. Ed.*, 2013, **52**, 4422–4425.
- [126] J. Cai, C. A. Pignedoli, L. Talirz, P. Ruffieux, H. Söde, L. Liang, V. Meunier, R. Berger, R. Li, X. Feng, K. Müllen and R. Fasel, *Nature Nanotech.*, 2014, **9**, 896–900.
- [127] G. D. Nguyen, F. M. Tom, T. Cao, Z. Pedramrazi, C. Chen, D. J. Rizzo, T. Joshi, C. Bronner, Y. C. Chen, M. Favaro, S. G. Louie and a. M. F. C. F. R. Fischer, *J. Phys. Chem. C*, 2016, **120**, 2684–2687.
- [128] Y. Cao, J. Qi, Y.-F. Zhang, L. Huang, Q. Zheng, X. Lin, Z. Cheng, Y.-Y. Zhang, X. Feng, S. Du, S. T. Pantelides and H.-J. Gao, *Nano Research*, 2018, **11**, 6190–6196.
- [129] S. Kawai, S. Saito, S. Osumi, S. Yamaguchi, A. S. Foster, P. Spijker and E. Meyer, *Nature Comm.*, 2015, **6**, 8098.
- [130] R. R. Cloke, T. Marangoni, G. D. Nguyen, T. Joshi, D. J. Rizzo, C. Bronner, T. Cao, S. G. Louie, M. F. Crommie and F. R. Fischer, *J. Am. Chem. Soc.*, 2015, **137**, 8872–8875.
- [131] R. A. Durr, D. Haberer, Y.-L. Lee, R. Blackwell, A. M. Kalayjian, T. Marangoni, J. Ihm, S. G. Louie and F. R. Fischer, *J. Am. Chem. Soc.*, 2018, **140**, 807–813.
- [132] S. Kawai, S. Nakatsuka, T. Hatakeyama, R. Pawlak, T. Meier, J. Tracey, E. Meyer and A. S. Foster, *Science Adv.*, 2018, **4**, 4.
- [133] P. S. Costa, J. D. Teeter, A. Enders and A. Sinitskii, *Carbon*, 2018, **134**, 310–315.
- [134] Y.-C. Chen, T. Cao, C. Chen, Z. Pedramrazi, D. Haberer, D. G. de Oteyza, F. R. Fischer, S. G. Louie and M. F. Crommie, *Nature Nanotech.*, 2015, **10**, 156–160.
- [135] C. Bronner, R. A. Durr, D. J. Rizzo, Y.-L. Lee, T. Marangoni, A. M. Kalayjian, H. Rodriguez, W. Zhao, S. G. Louie, F. R. Fischer and M. F. Crommie, *ACS Nano*, 2018, **12**, 2193–2200.
- [136] G. D. Nguyen, H.-Z. Tsai, A. A. Omrani, T. Marangoni, M. Wu, D. J. Rizzo, G. F. Rodgers, R. R. Cloke, R. A. Durr, Y. Sakai, F. Liou, A. S. Aikawa, J. R. Chelikowsky, S. G. Louie, F. R. Fischer and M. F. Crommie, *Nature Nanotech.*, 2017, **12**, 1077–1082.

- [137] C. Ma, L. Liang, Z. Xiao, A. A. Poretzky, K. Hong, W. Lu, V. Meunier, J. Bernholc and A.-P. Li, *Nano Lett.*, 2017, **17**, 6241–6247.
- [138] S. Wang, N. Kharche, E. C. Girão, X. Feng, K. Müllen, V. Meunier, R. Fasel and P. Ruffieux, *Nano letters*, 2017, **17**, 4277–4283.
- [139] B. V. Senkovskiy, A. V. Nenashev, S. K. Alavi, Y. Falke, M. Hell, P. Bampoulis, D. V. Rybkovskiy, D. Y. Usachov, A. V. Fedorov, A. I. Chernov, F. Gebhard, K. Meerholz, D. Hertel, M. Arita, T. Okuda, K. Miyamoto, K. Shimada, F. R. Fischer, T. Michely, S. D. Baranovskii, K. Lindfors, T. Szkopek and A. Grüneis, *Nature Comm.*, 2021, **12**, 2542.
- [140] J.-P. Joost, A.-P. Jauho and M. Bonitz, *Nano Lett.*, 2019, **19**, 9045–9050.
- [141] J. Li, S. Sanz, N. Merino-Díez, M. Vilas-Varela, A. Garcia-Lekue, M. Corso, D. G. de Oteyza, T. Frederiksen, D. Peña and J. I. Pascual, *Nature Comm.*, 2021, **12**, 5538.
- [142] Y.-L. Lee, F. Zhao, T. Cao, J. Ihm and S. G. Louie, *Phys. Rev. Lett.*, 2018, **18**, 7247–7253.
- [143] D. J. Rizzo, G. Veber, T. Cao, C. Bronner, T. Chen, F. Zhao, H. Rodriguez, S. G. Louie, M. F. Crommie and F. R. Fischer, *Nature*, 2018, **560**, 204–208.
- [144] S. Lone, A. Bhardwaj, A. K. Pandit, S. Gupta and S. Mahajan, *J. Electron. Mater.*, 2021, **50**, 3169–3186.
- [145] J. Wang and Q. Wang, *Physica B Condensed Matter*, 2020, **583**, 412022.
- [146] W. S. Hwang, P. Zhao, S. G. Kim, R. Yan, G. Klimeck, A. Seabaugh, S. K. Fullerton-Shirey, H. G. Xing and D. Jena, *npj 2D Mater. Appl.*, 2019, **3**, 43.
- [147] M. E. Abbassi, M. L. Perrin, G. B. Barin, S. Sangtarash, J. Overbeck, O. Braun, C. J. Lambert, Q. Sun, T. Precht, A. Narita, K. Müllen, P. Ruffieux, H. Sadeghi, R. Fasel and M. Calame, *ACS Nano*, 2020, **14**, 5754–5762.
- [148] O. V. Yazyev and M. I. Katsnelson, *Phys. Rev. Lett.*, 2008, **100**, 047209.
- [149] M. Wimmer, İnanç Adagideli, S. Berber, D. Tománek and K. Richter, *Phys. Rev. Lett.*, 2008, **100**, 177207.
- [150] S. Ye, Y. Lv, Z. Tang, R. Hu, R. Zhu, Z. Wang, Q. Huang, H. Wang, J. He and S. Chang, *Phys. Rev. Appl.*, 2019, **12**, 044018.
- [151] H. Wang, H. S. Wang, C. Ma, L. Chen, C. Jiang, C. Chen, X. Xie, A.-P. Li and X. Wang, *Nat. Rev. Phys.*, 2021, **3**, 791–802.

- [152] M. Shekhirev, A. Lipatov, A. Torres, N. S. Vorobeva, A. Harkleroad, A. Lashkov, V. Sysoev and A. Sinitskii, *ACS Appl. Mater. Interfaces*, 2020, **12**, 7392–7402.
- [153] S. J. Kheirabadi, R. Ghayour, M. Sanaee and B. Jooj, *Physica E: Low-dimensional Systems and Nanostructures*, 2021, **129**, 114635.
- [154] M. M. Pour, A. Lashkov, A. Radocea, X. Liu, T. Sun, A. Lipatov, R. A. Korlacki, M. Shekhirev, N. R. Aluru, J. W. Lyding, V. Sysoev and A. Sinitskii, *Nature Comm.*, 2017, **8**, 820.
- [155] X. Yu, Z. Dong, J. K. W. Yang and Q. J. Wang, *Optica*, 2016, **3**, 979.
- [156] M. H. Zarei and M. J. Sharifi, *Journal of Computational Electronics*, 2018, **17**, 531–539.
- [157] M. D. Fischbein and M. Drndić, *Appl. Phys. Lett.*, 2008, **93**, 113107.
- [158] G. F. Schneider, S. W. Kowalczyk, V. E. Calado, G. Pandraud, H. W. Zandbergen, L. M. K. Vandersypen and C. Dekker, *Nano Lett.*, 2010, **10**, 3163–3167.
- [159] M. Bieri, M. Treier, J. Cai, K. Aït-Mansour, P. Ruffieux, O. Gröning, P. Gröning, M. Kastler, R. Rieger, X. Feng, K. Müllen and R. Fasel, *Chem. Comm.*, 2009, 6919.
- [160] Y. Li, Z. Zhou, P. Shen and Z. Chen, *Chem. Comm.*, 2010, **46**, 3672.
- [161] M. Hatanaka, *Chem. Phys. Lett.*, 2010, **488**, 187–192.
- [162] A. Baskin and P. Král, *Sci. Rep.*, 2011, **1**, 36.
- [163] A. Du, Z. Zhu and S. C. Smith, *J. Am. Chem. Soc.*, 2010, **132**, 2876–2877.
- [164] R. Pawlak, X. Liu, S. Ninova, P. D’Astolfo, C. Drechsel, S. Sangtarash, R. Häner, S. Decurtins, H. Sadeghi, C. J. Lambert, U. Aschauer, S.-X. Liu and E. Meyer, *J. Am. Chem. Soc.*, 2020, **142**, 12568–12573.
- [165] M. R. Ajayakumar, M. D. Giovannantonio, C. A. Pignedoli, L. Yang, P. Ruffieux, J. Ma, R. Fasel and X. Feng, *J. Polym. Sci.*, 2022, **60**, 1912–1917.
- [166] R. Zuzak, I. Pozo, M. Engelund, A. Garcia-Lekue, M. Vilas-Varela, J. M. Alonso, M. Szymonski, E. Guitián, D. Pérez, S. Godlewski and D. Peña, *J. Chem. Sci.*, 2019, **10**, 10143–10148.
- [167] K. Xu, J. I. Urgel, K. Eimre, M. D. Giovannantonio, A. Keerthi, H. Komber, S. Wang, A. Narita, R. Berger, P. Ruffieux, C. A. Pignedoli, J. Liu, K. Müllen, R. Fasel and X. Feng, *J. Am. Chem. Soc.*, 2019, **141**, 7726–7730.

- [168] P. H. Jacobse, R. D. McCurdy, J. Jiang, D. J. Rizzo, G. Veber, P. Butler, R. Zuzak, S. G. Louie, F. R. Fischer and M. F. Crommie, *J. Am. Chem. Soc.*, 2020, **142**, 13507–13514.
- [169] K. Oura, V. Lifshits, A. Saranin, A. Zotov and M. Katayama, *Surface Science, An Introduction*, Springer Verlag, 2003.
- [170] ScientaOmicron, *LT-STM III Brochure*, [https://scientaomicron.com/Downloads/Brochures/SPM/LT\\_STM\\_III\\_S0\\_Brochure.pdf](https://scientaomicron.com/Downloads/Brochures/SPM/LT_STM_III_S0_Brochure.pdf), 2021, accessed 03.2022.
- [171] F. Hanke and J. Björk, *Phys. Rev. B*, 2013, **87**, 235422.
- [172] W. Shockley, *Phys. Rev.*, 1939, **56**, 317–323.
- [173] H. Walen, D.-J. Liu, J. Oh, H. Lim, J. W. Evans, Y. Kim and P. A. Thiel, *J. Chem. Phys.*, 2015, **143**, 014704.
- [174] M. Corso, F. Schiller, L. Fernandez, J. Cordon and J. Ortega, *Journal of physics. Condensed matter: an Institute of Physics journal*, 2009, **21**, 353001.
- [175] V. Repain, J.-M. Berroir, S. Rousset and J. Lecoœur, *Europhys. Lett.*, 2007, **47**, 435.
- [176] S. Narasimhan and D. Vanderbilt, *Phys. Rev. Lett.*, 1992, **69**, 1564–1567.
- [177] S. B. Darling, A. W. Rosenbaum, Y. Wang and S. J. Sibener, *Langmuir*, 2002, **18**, 7462–7468.
- [178] J. Björk, F. Hanke and S. Stafström, *J. Am. Chem. Soc.*, 2013, **135**, 5768–5775.
- [179] J. Björk and F. Hanke, *Chemistry*, 2014, **20**, 928–934.
- [180] S. Ernst, S. Wirth, M. Rams, V. Dolocan and F. Steglich, *Science and Technology of Advanced Materials*, 2007, **8**, 347–351.
- [181] V. T. Binh., *Journal of Microscopy*, 1988, **152**, 355–361.
- [182] A. Fick, *Ann. Phys.*, 1855, **170**, 59–86.
- [183] A. Enders, R. Skomski and J. Honolka, *Journal of Physics Condensed Matter*, 2010, **22**, 433001.
- [184] M. D. Giovannantonio, O. Deniz, J. I. Urgel, R. Widmer, T. Dienel, S. Stolz, C. Sánchez-Sánchez, M. Muntwiler, T. Dumsclaff, R. Berger, A. Narita, X. Feng, K. Müllen, P. Ruffieux and R. Fasel, *ACS Nano*, 2018, **12**, 74–81.

- [185] J. D. Teeter, P. S. Costa, P. Zahl, T. H. Vo, M. Shekhirev, W. Xu, X. C. Zeng, A. Enders and A. Sinitskii, *Nanoscale*, 2017, **9**, 18835–18844.
- [186] T. H. Vo, M. Shekhirev, A. Lipatov, R. A. Korlacki and A. Sinitskii, *Faraday Discuss.*, 2014, **173**, 105.
- [187] T. Marangoni, D. Haberer, D. J. Rizzo, R. R. Cloke and F. R. Fischer, *Chem. Eur. J.*, 2016, **22**, 13037–13040.
- [188] M. Shekhirev, P. Zahl and A. Sinitskii, *ACS Nano*, 2018, **12**, 8662–8669.
- [189] X. Liu, G. Li, A. Lipatov, T. Sun, M. M. Pour, N. R. Aluru, J. W. Lyding and A. Sinitskii, *Nano Research*, 2020, **13**, 1713–1722.
- [190] A. L. Vázquez de Parga and R. Miranda, in *Scanning Tunneling Spectroscopy*, ed. B. Bhushan, Springer Netherlands, Dordrecht, 2012, pp. 2313–2321.
- [191] L. Talirz, H. Söde, T. Dumsloff, S. Wang, J. R. Sanchez-Valencia, J. Liu, P. Shinde, C. A. Pignedoli, L. Liang, V. Meunier, N. C. Plumb, M. Shi, X. Feng, A. Narita, K. Müllen, R. Fasel and P. Ruffieux, *ACS Nano*, 2017, **11**, 1380–1388.
- [192] M. Vladimirova, M. Stengel, A. D. Vita, A. Baldereschi, M. Böhringer, K. Morgenstern, R. Berndt and W.-D. Schneider, *Europhys. Lett.*, 2001, **56**, 254–260.
- [193] R. Smoluchowski, *Phys. Rev.*, 1941, **60**, 661–674.
- [194] C. Ma, Z. Xiao, W. Lu, J. Huang, K. Hong, J. Bernholc and A.-P. Li, *Chem. Comm.*, 2019, **55**, 11848–11851.
- [195] J. Yamaguchi, H. Hayashi, H. Jippo, A. Shiotari, M. Ohtomo, M. Sakakura, N. Hieda, N. Aratani, M. Ohfuchi, Y. Sugimoto, H. Yamada and S. Sato, *Comm. Mater.*, 2020, **1**, 36.
- [196] T. Yamamoto, A. Morita, Y. Miyazaki, T. Maruyama, H. Wakayama, Z. H. Zhou, Y. Nakamura, T. Kanbara, S. Sasaki and K. Kubota, *Macromolecules*, 1992, **25**, 1214–1223.
- [197] G. Rojas, S. Simpson, X. Chen, D. A. Kunkel, J. Nitz, J. Xiao, P. A. Dowben, E. Zurek and A. Enders, *Phys. Chem. Chem. Phys.*, 2012, **14**, 4971.
- [198] E. V. Iski, A. D. Jewell, H. L. Tierney, G. Kyriakou and E. C. H. Sykes, *Journal of Vacuum Science & Technology A*, 2011, **29**, 040601.
- [199] K. Schouteden, P. Lievens and C. Van Haesendonck, *Phys. Rev. B*, 2009, **79**, 195409.

- 
- [200] A. Taqieddin and N. R. Aluru, *ACS Appl. Nano Mater.*, 2021, **4**, 5816–5824.
- [201] J. van der Lit, P. H. Jacobse, D. Vanmaekelbergh and I. Swart, *New J. Phys.*, 2015, **17**, 053013.
- [202] J. Lawrence, P. Brandimarte, A. Berdonces-Layunta, M. S. G. Mohammed, A. Grewal, C. C. Leon, D. Sánchez-Portal and D. G. de Oteyza, *ACS Nano*, 2020, **14**, 4499–4508.
- [203] M. C. Chong, N. Afshar-Imani, F. Scheurer, C. Cardoso, A. Ferretti, D. Prezzi and G. Schull, *Nano Lett.*, 2018, **18**, 175–181.
- [204] T. Cao, F. Zhao and S. G. Louie, *Phys. Rev. Lett.*, 2017, **119**, 076401.
- [205] H. Huang, D. Wei, J. Sun, S. L. Wong, Y. P. Feng, A. H. C. Neto and A. T. S. Wee, *Sci. Rep.*, 2012, **2**, 983.
- [206] J. Björk, S. Stafström and F. Hanke, *J. Am. Chem. Soc.*, 2011, **133**, 14884–14887.
- [207] J. D. Teeter, P. S. Costa, C. Dobner, M. Sarker, A. Sinitskii and A. Enders, *Chem. Phys. Chem.*, 2021, **22**, 1769–1773.
- [208] X.-Y. Wang, A. Narita and K. Müllen, *Nature Reviews Chemistry*, 2017, **2**, 0100.
- [209] N. Kharche and V. Meunier, *J. Phys. Chem. Lett.*, 2016, **7**, 1526–1533.



# Eidesstattliche Versicherung

Hiermit versichere ich an Eides statt, dass ich die vorliegende Arbeit selbstständig verfasst und keine anderen als die von mir angegebenen Quellen und Hilfsmittel verwendet habe.

Weiterhin erkläre ich, dass ich die Hilfe von gewerblichen Promotionsberatern bzw. -vermittlern oder ähnlichen Dienstleistern weder bisher in Anspruch genommen habe, noch künftig in Anspruch nehmen werde.

Zusätzlich erkläre ich hiermit, dass ich keinerlei frühere Promotionsversuche unternommen habe.

Bayreuth, den

---

Christoph Dobner